NTNU – Trondheim
Norwegian University of
Science and Technology

High Efficiency Electric Propulsion Systems for Shell Eco-Marathon 2014

Eirik Heien Mo

Master of Energy and Environmental Engineering
Submission date: June 2014
Supervisor: Trond Toftevaag, ELKRAFT

Norwegian University of Science and Technology
Department of Electric Power Engineering

Task description

Background

The NTNU development team DNV GL Fuel Fighter plans to compete with two different electric cars during Shell Eco-marathon May 2014. One car in the "Prototype" class and another in the "UrbanConcept" class. The official rules of 2014 states that the motor controller must be purpose-built for the Shell Eco-marathon. Main task: Assist the DNV GL Fuel Fighter team in the planning, design and building process of the two electric drivetrains.

Scope of work

The process involves identifying competition regulations, literature studies and identifying the tasks that needs to be done. Designing the system, with emphasis on efficiency optimization, requires sub-component analysis, evaluation, model simulations and testing. The sub-components of the motor controller that should be considered are FPGA (Field-Programmable gate array) in combination with a three-phase inverter. Building involves connecting the sub-components into a system, including testing, measurements and optimization.

Preface

During the fall semester 2013 I wrote a specialisation project on the subject permanent magnet synchronous machine modelling. While gaining knowledge on this subject I could not avoid learning about vector control for this type of machine as well. During the same semester I was recruited by DNV GL Fuel Fighter, for looking into ways of improving the motor used in their UrbanConcept vehicle. While doing this I discovered that it was not only the electric motor that required attention. The most challenging task involving the preparations for Shell Eco-Marathon 2014 was that the motor controller now had to be purpose-built. Based on this I decided that my master thesis work would have to involve realising the electric propulsion system for the next competition. The required work was expanded when the team decided to bring two vehicles to the competition.

I would like to use the next sections to express my sincere gratitude to the people who made this thesis work possible.

First off I would like to thank my co-supervisor Kjell Ljøkelsøy for all of his dedication and supreme guidance involving almost every single part of the thesis work. Without him the final results presented in this thesis would not have been possible to achieve. I would also like to thank my supervisor Trond Toftevaag. Whenever I got stuck with a problem he was always able to help me find a solution by asking the right questions, or pointing me in the direction of people that could help.

In order to set up the different tests presented in this thesis a lot of help from NTNU staff was needed. Without the services provided by the Power Electronics Workshop or the Service lab these test would never have been possible to perform. Special thanks goes to Vladimir Klubicka and Erland Strendo. Vladimir provided a lot of help involving the ordering process of electronic components. Erland provided several services involving mechanical parts for both the vehicles and the motor test rig.

For advice provided for different academic disciplines of the project I would also like to thank Lars Norum, Tore M. Undeland and Atle Rygg Årdal.

The work would also not have been possible without the sponsors:
Noca, Elprint Norge and SINTEF Energi.

Last, but not least, I would like to thank the DNV GL Fuel Fighter team for a great experience and for always being able to help me with my problems, even though they had their own tasks to worry about.

Trondheim 12.06.2014

Eirik Heien Mo

Abstract

DNV GL Fuel Fighter is a team that have been participating in Shell Eco-Marathon (SEM) each year since 2008. The members vary for each year and are mainly NTNU students in their fourth or final year of their master's program. SEM is not like a regular race. In order to win you don't necessarily need to have the fastest vehicle, but the most energy efficient one. Energy used from the batteries was measured with a joulemeter. After finishing a valid competition attempt the measured joules consumption is used to calculate a km/kWh result. The vehicle with the highest km/kWh result wins the competition. SEM 2014 was arranged in Rotterdam, Netherlands. The 2014 team decided to bring two vehicles to the competition, one participating in the UrbanConcept class and another in the Prototype class. The urban concept vehicle had been reworked and reused since it was built in 2008. The prototype vehicle was built from scratch for the 2014 competition.

The work presented in this thesis is related to the electric propulsion system developed for both the urban concept and the prototype vehicle. This system is divided into four different sub systems in order to be described in detail: The electric motor, inverter, controller and encoder. All of the electric motors considered were of the type permanent magnet synchronous machine (PMSM).

Two electric motors was considered for the prototype vehicle: The EC 60 flat and the AXI motor. The EC 60 flat motor was rated for low power purposes. Early simulation model results concluded that the motor would not be able to withstand the expected loads. This conclusion was confirmed with a motor malfunction on the motor test rig. The AXI motor had higher power ratings and was used for the competition. Two motors was also available for the urban concept vehicle, but one of them broke, so the other was used. An efficiency diagram was produced for the urban concept vehicle motor by running it on a motor test rig. The tests concluded that the motor was most efficient when driving faster than 29 km/h.

The motor controller used had to be purpose-built for SEM. This was a new rule for the 2014 competition. The final motor controller solution developed for SEM 2014 was made by combining a purpose-built two-level three-phase voltage source converter and a field-programmable gate array (FPGA). These two parts are referred to as the inverter and controller respectively, in the electric propulsion system.

For the rotor position measurement optic encoder with index channel was used. There were some issues with the urban concept vehicle encoder solution during the competition.

The end result was a 3rd place in the urban concept class and a 7th place in the prototype class. The final result in the urban concept class 2014 was actually better than the final result with the same vehicle in 2013, if the solar power is taken out of the equation.

Suggested electric propulsion system improvements for SEM 2015 preparations are found at the end of this thesis.

Sammendrag

DNV GL Fuel Fighter er et lag som har deltatt på Shell Eco-Marathon hvert år siden 2008. Medlemsgruppen endres hvert år og er hovedsakelig NTNU-studenter i sitt fjerde eller siste år av sitt masterprogram. SEM er ikke lik en vanlig bilkonkurranse. Det er ikke nødvendigvis den raskeste bilen som vinner, men den mest energieffektive. Energien som blir brukt fra batteriene i bilen blir målt av et joulemeter. Etter et gyldig løp på banen blir målingen fra joulemeteret brukt til å regne ut et km/kWt resultat. Bilen med det høyeste km/kWt resultatet vinner konkurransen. Laget bestemte seg for a ta med seg to biler til konkurransen i 2014. En av bilene konkurrerte i klassen UrbanConcept og den andre i Prototype klassen. Urban concept-bilen er den samme som ble først bygd i 2008, men har blitt gjenbrukt og oppgradert siden da. Prototype-bilen var bygd fra grunnen av for SEM 2014.

Arbeidet presentert i denne avhandlingen er relatert til det elektriske fremdriftssystemet utviklet for både urban concept- og prototype-bilen. Systemet er videre delt inn i fire delsystemer for å kunne beskrive alt i detalj: Elektrisk motor, vekselretter, kontroller og enkoder. Alle elektriske motorer vurdert i denne avhandlingen er av typen permanent magnet synkron maskin (PMSM).

To elektriske motorer ble vurdert for prototype-bilen: EC 60 flat og AXI motoren. EC 60 flat motoren er egnet for lav last. En simuleringsmodell resultater konkluderte at motoren ikke ville tåle lasten som var forventet. Denne konklusjonen ble bekreftet da motoren ble ødelagt under testing på motortestbenken. AXI motoren var egnet for høyere last og var brukt for konkurransen. To motorer var også vurdert for urban concept-bilen, men en av dem ble ødelagt. Den andre ble brukt som en konsekvens av dette. Et virkningsgradsdiagram ble produsert for urban concept-bil motoren basert på resultater fra motortestbenken. Motoren kjørte best når hastigheten var over 29 km/t.

Motorkontrolleren brukt måtte være “purpose-built” for SEM. Denne regelen var ny for konkurransen i 2014. Den endelige motorkontroller løsningen for konkurransen i 2014 var en “purpose-built” trefase tonivå spenningskildeomformer kontrollert av en field-programable gate array (FPGA). Disse to delene representerer henholdsvis vekselretter og kontroller i fremdriftssystemet.

For rotor posisjonsmåling ble optisk enkoder med indeks signal brukt. Det ble noen problemer med denne delen for urban concept-bil systemet under konkurransen.

Det endelige resultatet ble en 3. plass i urban concept klassen og en 7. plass i prototype klassen. Resultatet oppnådd i urban concept-klassen i 2014 var faktisk bedre enn resultatet som ble oppnådd med samme bilen i 2013, så lenge solenergi er trukket fra utregningen.

Foreslåtte forbedringer av fremdriftssystemet for forberedelsene til SEM 2015 er funnet i slutten av denne avhandlingen.

Table of Contents

Abbreviations

SEM: Shell Eco-Marathon

PMSM: Permanent Magnet Synchronous Machine

VSC: Voltage Source Converter

PWM: Pulse Width Modulation

MOSFET: Metal-Oxide-Semiconductor Field-Effect Transistor

IGBT: Insulated Gate Bipolar Transistor

NI: National Instruments

IR: International Rectifier

FPGA: Field-Programmable Gate Array

DC: Direct Current

AC: Alternating Current

IC: Integrated Circuit

LED: Light Emitting Diode

PCB: Printed Circuit Board

List of figures

Chapter 1: Introduction

1.1 Background

The NTNU development team DNV GL Fuel Fighter would compete with two different electrical vehicles during Shell Eco-Marathon May 2014. One vehicle in the "Prototype" class and another in the "UrbanConcept" class. The official rules of 2014 now stated that the motor controller must be purpose-built for the Shell Eco-Marathon. This was a new rule for the 2014 competition. In previous years purchased motor controllers was allowed.

1.2 Objective

Assist the DNV GL Fuel Fighter 2014 team in the planning, design and building process of the electric drivetrains for both the prototype and the urban concept class vehicle.

1.3 Scope of work

The main work presented in this thesis involves the motor controller components, encoders and electric motors. Other team members was able to take care of the remaining electric drivetrain components. For more information on the project work which the other members of the team has performed, see the full project master thesis: [1].

The initial process of this thesis involved identifying competition regulations, literature studies and identifying the tasks that needed to be done.

In order to design the electric propulsion system for the vehicles, with emphasis on efficiency optimization, sub-component analysis, evaluation, testing and model simulation was required. The sub-components of the motor controller that was considered were the FPGA (Field-Programmable gate array) in combination with a two level VSC (voltage source converter).

Building involved connecting the sub-components into a system, including testing, measurements and optimization.

1.4 Limitations

The work presented in this thesis was limited to analysis and testing which, in the end, would help to improve competition results during the Shell Eco-Marathon. Thus most of the work done has had a strong focus on ensuring stabile system operation with minimum losses.

1.5 Software

List 1.5.1 sums up the software used for modelling the electrical system, software analysis and implementing control systems in the FPGA hardware.

1. MATLAB [2]
2. Simulink [3]
3. SimPowerSystems [4]
4. LabVIEW [5]
5. Cadstar [6]
6. Active DSP

List 1.5.1: Software used for system modelling, analysis and control procedures

Chapter 2: Team, competition, system and vehicle descriptions

This chapter shortly describes the different aspects of the thesis. A full project overview is important to present before jumping into the complex subcomponent descriptions and considerations. It is also important because some specific aspects cannot be described in the detailed chapters as they govern the whole system.

2.1 The team and project work

2.1.1 DNV GL Fuel Fighter, team 2014

There were approximately sixteen team members of DNV GL Fuel Fighter team 2014. See figure 2.1.1.1. For the full member descriptions see [7].

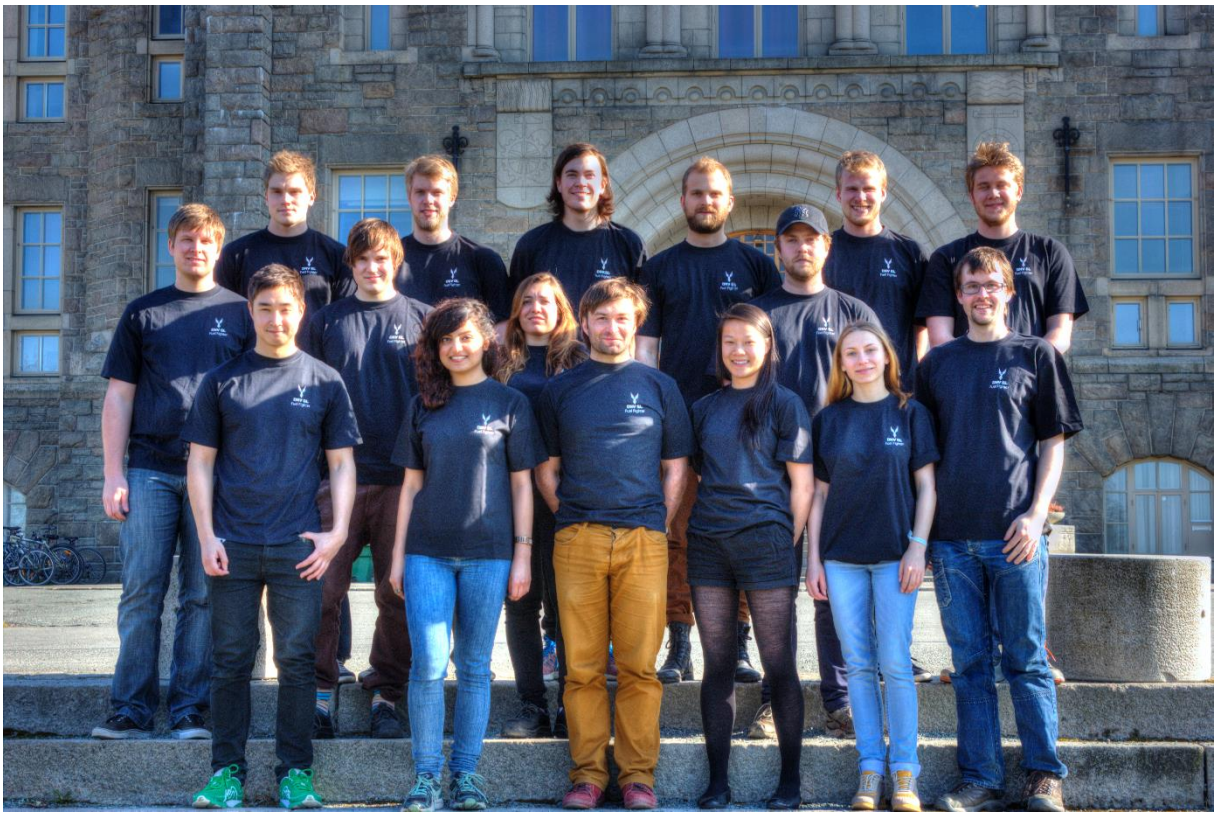

Figure 2.1.1.1: DNV GL Fuel Fighter, team 2014

Of these sixteen members there were five mechanical engineering students, three cybernetics engineering students, two physics and mathematics engineering students, two drivers and three students doing administrative and public relations work. The last member is a power electronics student and also the writer of this thesis.

2.1.2 Full vehicle system overview and relevant thesis work specification

Figure 2.1.2.1 illustrates a total system overview applicable both vehicles. It does also show what part of the system that are of main interest in this thesis.

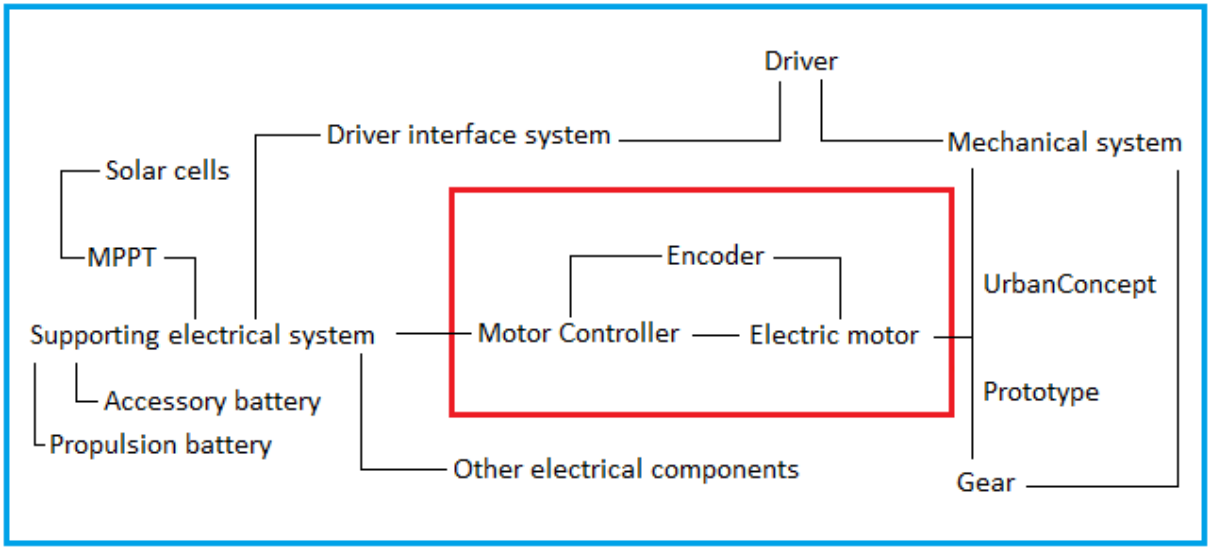

Figure 2.1.2.1: Total system (blue square) overview with main thesis work components (red square) illustrated

The components which are relevant for this thesis is placed within the red square of figure 2.1.2.1 and will be referred to as the electric propulsion system. This part became of main interest, because other team members would be able to take care of the other parts of the electric drivetrain. Thesis work involving some of the activities outside of the red square and administrative work will not be presented here. Some of these descriptions are found in the full master project report. Some of components depicted outside the red square may be mentioned briefly in this thesis, but only when it is relevant for the components within the red square.

2.2 Shell Eco-Marathon 2014 competition in Rotterdam

2.2.1 Track, driving requirements and vehicle performance measuring standard

The Shell Eco-Marathon is not like a regular race. In order to win you don't necessarily need to have the fastest vehicle, but the most energy efficient one. Energy used from the batteries was measured with a joulemeter. After finishing a valid attempt, by driving the required laps on the track correctly, the joules consumed by the electric system are calculated into kilo meters per kilo watt hour [km/kWh]. The vehicle with the highest km/kWh wins the competition.

Another joulemeter measured battery power charged by solar cells. Previously all solar energy produced would contribute to the total calculated km/kWh, but a new rule this year only allowed the solar power to cover 20% of the energy used for propulsion purposes.

"Net propulsion energy = motor propulsion energy – solar energy. The amount of solar energy used in this calculation will be limited to no more than 20% of the motor propulsion energy used during the run."

– Shell Eco-Marathon Official Rules 2014 [8]

This was done by subtracting the remaining measured solar energy provided, that was above the 20% of total propulsion power consumption, from the total km/kWh equation.

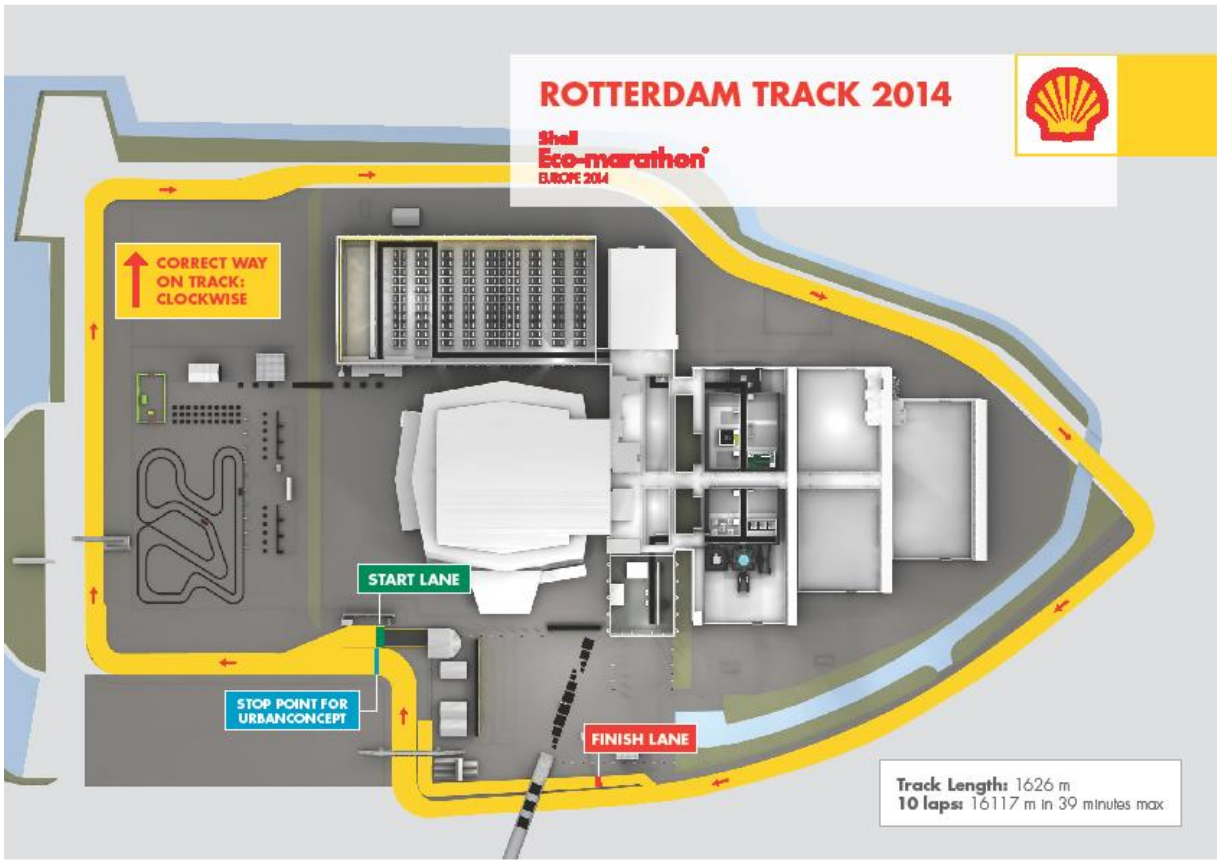

Figure 2.2.1.1: The SEM Rotterdam track 2014, Ahoy [9]

Figure 2.2.1.1 illustrates the race track. The total length of one lap is 1626 meters. In order to achieve a valid attempt the vehicle has to perform 10 consecutive laps, 16117 meters, within 39 minutes. Equation 2.2.1.1 is the calculation of the required average speed of a valid attempt, based on the track data.

$$Required\ minimum\ average\ speed = \frac{16.117\ km}{\frac{39}{60}\ h} = 24{,}8\frac{km}{h} \qquad (2.2.1.1)$$

Right next to the "START LANE" in figure 2.2.1.1 is the "STOP POINT FOR URBANCONCEPT" line. The urban concept vehicles had to perform a complete stop, before accelerating again, once for each lap at this point. If the vehicle did not stop correctly on one of these occasions then the whole attempt would not be valid. Such a stop point did not exist for the prototype vehicles. Thus the only time the prototype vehicle had to stop was at the finish line after completing all of the 10 laps.

2.2.2 The "purpose-built" motor controller requirement

The most relevant part of the SEM 2014 rules [8], when it comes to the electric propulsion system of the vehicle, is found in the next quote:

"The drive train in the 'Battery Electric' category is restricted to a maximum of one electric storage device, and up to two electric motors, with associated control units. The electric motors may be purchased, purchased-and-modified, or purpose-built. The motor controller MUST be purpose-built for the Shell Eco-Marathon. Modifications to purchased motor controllers are not acceptable. Motor controllers built from sub-components such as single-board computers, power stages, etc. are encouraged. If a unit is developed incorporating the motor controller into one or more single printed circuit boards (PCB) the text "SEM" needs to be included in the mask of the PCB etching."

– Shell Eco-Marathon Official Rules 2014 [8]

Initially the plan for the prototype vehicle electrical system design was to use an almost identical system as in the urban vehicle. The problem was that the motor controller, will also be presented in this thesis as an inverter combined with a controller, used in the urban vehicle is no longer applicable for the 2014 competition, as it is not purpose-built for SEM. The motor controller previously used is made by SmartMotor [10] for controlling a small submarine vessel. Thus a purpose-built motor controller had to be built for both vehicles for the 2014 competition. As the motors for each vehicle are both of the type permanent magnet synchronous machine (PMSM), identical motor controllers may be made for both vehicles. Except for a few parameter variations in the controller unit and encoder mounting. More on these subjects in part 5.5 and 6.3.1.

The motor controller was encouraged to be made from sub-components. This is what exactly was done for the competition. As previously mentioned the motor controller was in this case created by producing an inverter circuit board which was controlled by a FPGA circuit board

with inverter control software. See chapter 4 and 5. The last part of the SEM rules quote is important. It states that the letters “SEM” has to be printed in the mask of the PCB etching. The letters are both printed on the inverter circuit board and found in the copper formation of the board. See part 4.3.1.

The final electric propulsion system uses the SINTEF [11] FPGA with related motordrive controller software. See part 5.2.2 for a detailed description. A critical concern was that the SINTEF FPGA circuit board was not purpose-made and would therefore not be allowed for the competition. An e-mail that was sent to SEM describing the system and asking if it would be purpose-made enough for the competition. See appendix F. The answer from SEM was that the system was allowed for use as long as the team had proper insight in the control system software. Proper understanding of the SINTEF software was therefore an important focus before arriving at the technical inspection.

2.3 The “UrbanConcept” vehicle

2.3.1 Special requirements

There are several important requirements that has to be met for an urban concept vehicle to pass technical inspection. To mention some the vehicle has to have four wheels, enough space for luggage, window wipers, brake lights, turn signals, drive lights, etc. The requirements are there to force the vehicle design into something that would be useful in the city. Thus “UrbanConcept”. For more information on the design of this vehicle see the 2013 team report: [12]. The minimum weight of drivers in the urban concept class is 70 kg.

2.3.2 Initial status

The previous team barely got through technical inspection with their urban concept vehicle during SEM 2013. Figure 2.3.2.1 is a picture of the vehicle during the 2013 revealing. The total weight of the vehicle is 96 kg. With one valid attempt the 2013 team managed to achieve a 3rd place with the result 201.9 km/kWh. [13] There were several mechanical issues that had to be fixed in order to be able to compete with it in 2014, but mainly two things, the steering and the towing hook. The steering capabilities was not good enough. Mainly because design involved using a climbing rope which caused too much slack. The towing hook did not meet the dimensions requirement for the 2014 competition and had to be completely replaced. As the mechanical part of the team was very busy with the creation of a totally new vehicle, the prototype, this year there was some concern of that the urban concept vehicle would not be ready in time for SEM 2014.

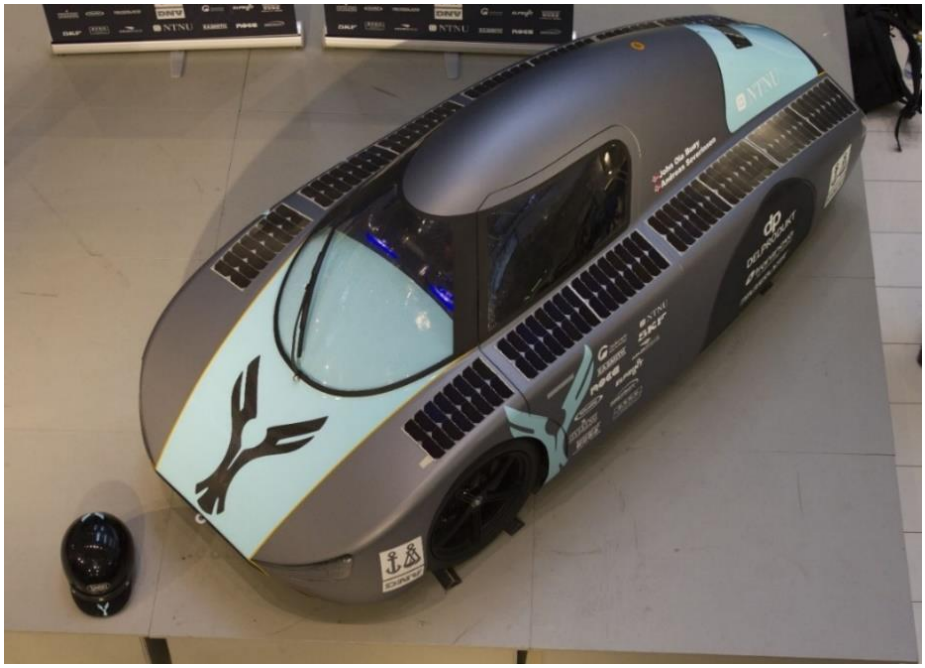

Figure 2.3.2.1: Urban concept vehicle during revealing 2013 [12]

Figure 2.3.2.2 illustrates the overall initial electrical system in the urban concept vehicle. The figure is just included here in order to illustrate the complexity of the electrical system and will therefore not be described in detail in this thesis. The complexity of this system is much greater than the average urban concept vehicle in the competition. Communication between the different modules in the system is done with a CAN bus.

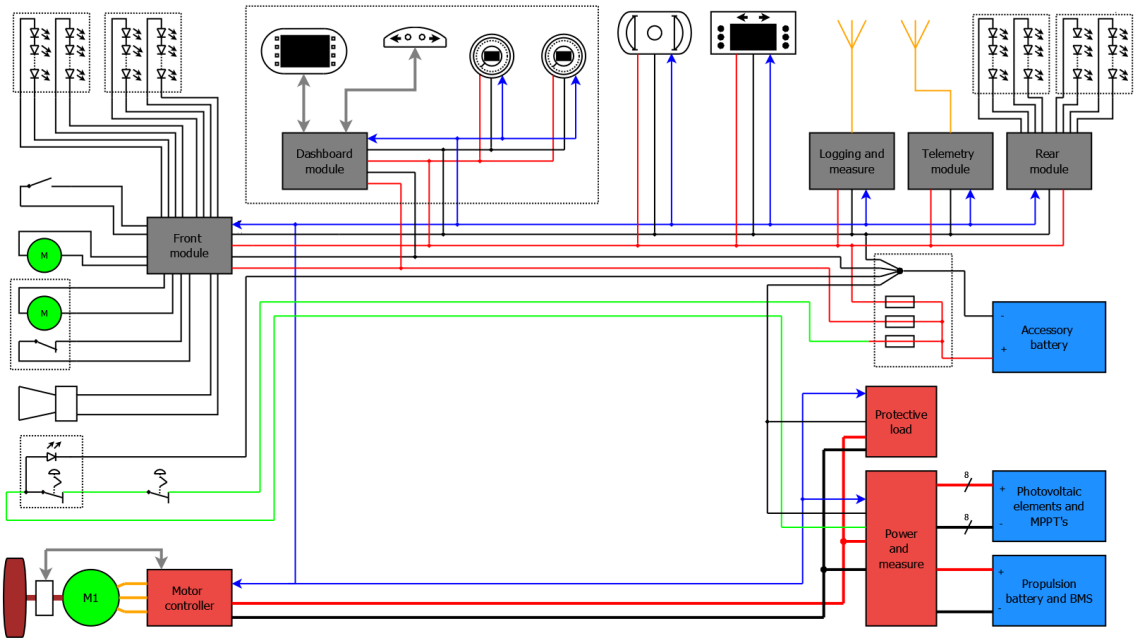

Figure 2.3.2.2: Initial urban vehicle electrical system overview diagram [12] *(edited)*

In the lower left corner of figure 2.3.2.2 the motor controller, motor and encoder is found. In part 3.3.1 more info on the 2013 motor is found and the encoder is described in part 6.2.2.

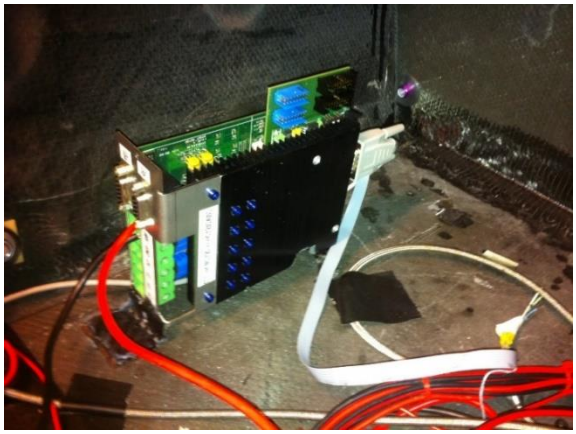

Figure 2.3.2.3: SmartMotor [10] *motor controller*

As mentioned in part 2.2.2 the motor controller for SEM 2014 had to be purpose-made for the competition. Figure 2.3.2.3 illustrates the motor controller that was in the urban concept vehicle at the start of the 2014 spring semester. The motor contoller used in 2013 is made by SmartMotor [10] for controlling the propulsion of a small unmanned submarine. As this motor contoller is not purpose made for SEM it could not be used for the 2014 competition. Thus a brand new motor contoller had to be made for this vehicle as well as the prototype vehicle.

2.4 The "Prototype" vehicle

2.4.1 Special requirements

Compared to the urban concept class the prototype class is much less restricted when it comes to the mechanical design. Four wheels, for example, is not required. This allows the vehicle to have only three wheels. Three wheels means that the vehicle can have a much smaller back than front. Allowing the droplet shape which is good shape from an aerodynamic perspective. Even back-wheel steering was allowed in during SEM 2014. Back-wheel steering would allow the vehicle to be much smaller as only one wheel would need space to turn, but it is also very dangerous as the vehicle becomes much harder to manoeuvre. Back-wheel steering will therefore not be allowed for SEM 2015. The new prototype vehicle has front wheel steering in order to be allowed for later competitions as well. For more information on the mechanical design of the new prototype vehicle see the 2014 team report: [1]. The prototype class is also less strict in the electrical design as there are no lights required. The minimum weight of drivers in the prototype class is 50 kg.

2.4.2 Initial status

The mechanical part of the team had been working on the design for the new prototype vehicle as their specialisation project as well. Thus this part of the project work was already a semester in as the spring semester and master thesis started. Figure 2.4.2.1 illustrates an early 3D rendered model of the vehicle. Initially the vehicle weight was estimated to be 30kg.

Figure 2.4.2.1: Prototype vehicle, early 3D rendered model by Magnus Skogsfjord

Not much had been planned electrically yet at the start of the spring semester. The electrical part of the team decided to make the electrical system as identical to the urban concept vehicle electrical system as possible. Just without the extra modules which was not required in the prototype class. This was decided on the basis of that a lot of spare modules from the urban concept vehicle could be used. For the motor controller this meant that the new design could be identical for both vehicles. Except for a few parameters in the software. The final electrical system design is described in part 9.1.

2.5 Energy source

As the energy source for the electrical system is not mentioned much later in the thesis it is briefly mentioned here. See [1] as well for more info.

Both of the vehicles will compete in the energy source class “Battery Electric”. Under this classification the vehicles are restricted to use Lithium-Ion batteries. The battery pack has to have a nominal voltage which is lower than 48 V and with a BMS (Battery Management System) included. [8]

More on the batteries used in the vehicles and battery pack calculation in part 7.3.1.

2.6 Main electric propulsion system components and design considerations

The main purpose of a motor controller is to control the supplied the power to the electrical machine. Electrical machines has a large variety of power input types. Some electrical machines needs alternating current, while others use direct current. The number of phases varies between different types of electrical machines as well. Three-phase is normal for AC machines, but both higher and lower number of phases are also common. The electric drivetrain design has to be adapted to the exact machine type used in the electrical system. For more information about the relevant electrical machines see chapter 3.

As the state of operation usually varies for the motor the electric drivetrain has to adapt to these factors as well. From internal and external inputs the power output of the electric drivetrain is regulated. The control part is done by one, or several, controller units in the system. Typical control inputs are currents, voltages, rotor position and manual control signals.

Figure 2.6.1 illustrates the main subcomponents of the electrical system used in the vehicles which are of main interest in this thesis: The electric motor, inverter, controller and encoder. The thesis is divided into these four parts for describing the system in chapters 3-6.

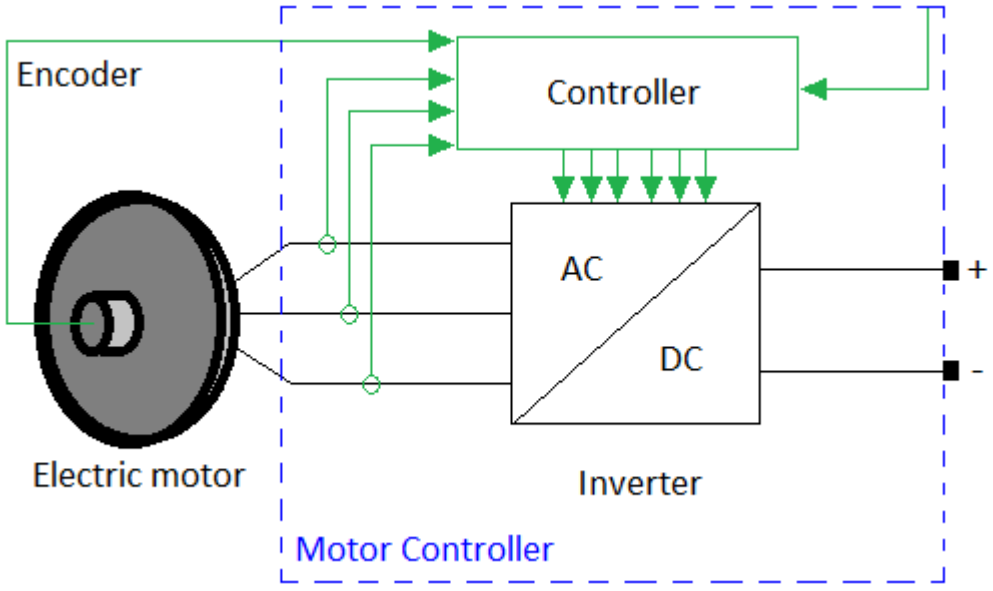

Figure 2.6.1: Main electric propulsion system subcomponents

Permanent magnet synchronous machine (PMSM) is the type of machine that is used for both vehicles in this project. As the PMSM runs on three-phase alternating current (AC) the direct current (DC) from the batteries has to be inverter. This is done with an inverter. The inverter is operated by a controller unit. The inputs needed for our controller is rotor angle and the three-phase current measurements. It does also require a torque or speed reference from the driver. The inverter type used in this thesis is the two level voltage source converter (VSC). It needs mainly six signals in order to be operated, one for each switch in

the circuit. These signals are provided by the controller. This will be described in further detail in the sub components respective chapters.

As the electric drivetrain that is to be designed in this thesis is supposed to drive a real vehicle with a real driver, several important factors has to be considered during the design process. List 2.6.1 lists some examples of critical design factors and ways to deal with them:

Factor	**Problem**	**Solution**
Voltages and currents	Voltages and currents may step out of their desired range during system operation, which could damage components.	Relevant voltages and currents should be monitored. If one steps out of range then shut-down/limiting sequence should be initiated.
Speed	High speeds may be dangerous for both the driver and the electrical system.	The system should automatically limit speed or shut down if the vehicle is moving too fast. Mechanical breaks must be present.
Temperature	All electrical components which transfers current results in some power loss. Power loss heats up the system and may lead to overheating.	Install heat sinks where overheating may occur. The system temperature should be monitored. If critical parts becomes too hot then the system should shut down.
Start-up sequence	Due to capacitors in the circuit the system may draw much current when turned on.	A soft-start circuit should be in series between the battery and the rest of the electrical system.
Shut-down sequence	As the system has energy storing components the system may not stop running after the battery is disconnected.	The rest of the electrical system should receive a shut-down signal when the battery is disconnected.
EMI (electromagnetic interference)	Disturbance may be applied to a circuit due to external or internal electromagnetism. This may lead to degradation of the circuit performance or abnormal operating conditions.	Sensitive circuits should not be too close to components with high inductive effects. Wires should be twisted to avoid induced current between them. Shielding some parts of the circuit may be an option if EMI proves to be a problem.
Vibrations	The circuit will experience vibrations while the vehicle is moving which may break the legs of some circuit components.	Use thick glue to prevent relevant circuit components from moving with the vibrations in any direction.

List 2.6.1: Electrical system critical design factors, problems and solutions

Chapter 3: Electric motor theory and motor selection

The different types of electrical motors is an important subject in this thesis. A suitable electric motor had to be chosen for both vehicles and the design of the motor controller and encoder mounts, part 6.3, strongly depended on the motor type.

In this part some theory involving the PMSM and dq-axis model will be presented. Most of it are samples from the specialisation project conducted during the fall semester of 2013 [14]*. For further details on the PMSM model theory presented please see the specialisation project.*

3.1 Electrical motor model theory

3.1.1 PMSM functional explanation and basic equations

In this part the a PMSM functional explanation will be given, including as some needed equations for understanding several different aspects of the thesis work. Many of the equations are not derived here. See [14].

The main parts of a permanent magnet synchronous machine are the rotor and stator. The armature windings are found in the stator. For a 3-phase machine, if we see the machine as a motor then connecting and placing the armature windings in a certain pattern a rotating magnetic field may be created. An example for a three-phase system (A, B and C), with mechanical synchronous rotation speed (ω_{sm}), is shown in figure 3.1.1.1.

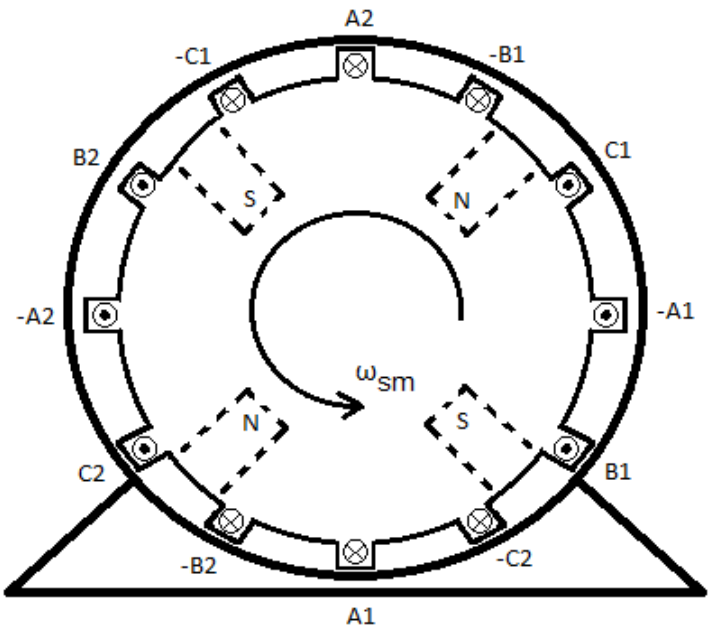

Figure 3.1.1.1: Induced rotating stator field [15]

Permanent magnets are placed on the rotor. If operated as a motor, the magnets will try to eliminate the rotating magnetic field. This process leads to a rotating motion as the magnets constantly try to follow the rotating magnetic field. From a generator viewpoint the rotating

magnets induce a voltage in the armature windings due to the changing magnetic field. This effect is documented by Faraday's law of induction.

The rotating speed of the magnetic field is depending of the number of poles in the machine and the electrical frequency of the system. The rotor speed is synchronized with the magnetic field rotation.

$$n = \frac{120\ f_e}{P}$$

n: magnetic field/rotor speed [r/min]
f_e: electrical frequency [Hz]
P: number of machine poles

(3.1.1.1) [15]

Equation 3.1.1.2 is the same function as in equation 3.1.1.1 just derived for [rad/s] instead of [r/min]:

$$\omega_{sm} = n\ \frac{2\pi}{60} = \frac{2\pi f_e}{P/2} = \frac{2}{P}\omega_{se}$$

ω_{sm}: synchronous mechanical speed [rad/s]
ω_{se}: synchronous electrical speed [rad/s]

(3.1.1.2)

For electrical and mechanical rotor position yields the same relationship:

$$\theta_m = \frac{2}{P}\theta_e$$

θ_m: mechanical rotor position [rad]
θ_e: electrical rotor position [rad]

(3.1.1.3)

In order to relate mechanical and electric power of a PMSM the following basic power equation is considered:

$$P_{sh} = \tau_{sh}\ \omega_m\ [W]$$

τ_{sh}: shaft torque [Nm]
ω_m: mechanical rotor speed [rad/s]

(3.1.1.4) [15]

The following equation is Newton's second law applied for the electromechanical system:

$$J\frac{d\omega_m}{dt} + D_d\omega_m = \tau_t - \tau_e$$

J: total moment of inertia [kg m^2]
D_d: damping-torque coefficient [Nms]
τ_t: Turbine torque [Nm]
τ_e: Electromagnetic torque [Nm]

(3.1.1.5) [16]

Equation 3.1.1.6 illustrates that the induced voltage in a machine is proportional to the rotational speed of the machine (see equation 3.1.1.2), as well as the number of turns (N) and the magnitude of the flux (φ) passing through the stator coil.

$$E_a = e_{rms} = \sqrt{2}\,\pi\, f_e\, N\, \varphi \quad [V]$$

(3.1.1.6) [15]

A connection between flux and current may be made. This is given in equation 3.1.1.7.

$$\varphi = BA = \mu \frac{NI}{l} A = \frac{1}{\left(\frac{l}{\mu A}\right)} (NI) = \frac{1}{\Re} \mathcal{F} \qquad (3.1.1.7)$$

$\Re$: reluctance [A-turns/wb]
$\mathcal{F}$: magnetomotive force [A-turn]
l: length of wire [m]
B: flux density
μ: magnetic permeability
A: area of cross section
I: current through one wire [A]

With this basic theory applied it is possible to define the connection between current and flux as a magnetic circuit diagram. In a magnetic circuit the same rules apply as for a regular electric circuit if the following replacements are made:

Electrical circuit	Magnetic circuit
Voltage, V [V]	Magnetomotive force (mmf), $\mathcal{F}$ [A-turn]
Current, I [A]	Flux, ϕ [wb]
Resistance, R [Ω]	Reluctance, $\Re$ [A-turn/wb]

List 3.1.1.1: Electrical versus Magnetic circuit [17]

An important parameter often used in the mathematical expressions for PMSMs is the inductance. Therefore the relationship between reluctance ($\Re$) and inductance (L) is derived:

Inductance is defined as the following:

$$L \overset{\text{def}}{=} \frac{\lambda}{I} = \frac{N\varphi}{I} \qquad (3.1.1.8)$$

λ: flux linkage

Combining equation 3.1.1.8 and equation 3.1.1.7 gives the following relation:

$$L = \frac{N\varphi}{I} = \frac{N\varphi}{\left(\frac{\varphi\Re}{N}\right)} = \frac{N^2}{\Re} \qquad (3.1.1.9)$$

Thus inductance is proportional to the inverse of reluctance.

Reluctance force in x direction (F_x) may be expressed as:

$$F_x = \frac{dW_c}{dx}\Big|_{I=const.} = \frac{1}{2} I^2 \frac{dL}{dx} - \frac{1}{2} {\varphi_g}^2 \frac{d\Re}{dx} + \frac{1}{2} NI \frac{d\varphi_g}{dx} \qquad (3.1.1.10)$$ [18]

x: position on the axis aligned with the force
φ_g: air gap flux

3.1.2 Park's transformation

A common way to model synchronous machines is to use a rotor reference system. Instead of referring values to the stator in a stationary three-phase system it is possible to create a new reference. As the rotor is rotating the new axes will also be rotating. The new axes are the d and q-axis. The d-axis points in the same direction as the rotor flux and the q-axis is 90° shifted as shown in figure 3.1.2.1.

Using the dq-axis system there will be especially two simplifications to the modelling which makes the analysis process easier:

1. Under steady state conditions, the currents and fluxes have constant, direct current, values.
2. As the axes are 90° apart the equivalent inductances on these axes will be orthogonal. This leads to two independent networks.

List 3.1.2.1: The two aspects that makes the dq-calculations easier to perform than other methods [19]

In order to perform this transformation one has to use the stationary two-phase system first, known as Clarke's transformation, defined here by the x- and y-axis. The xy-plane is also illustrated in figure 3.1.2.1.

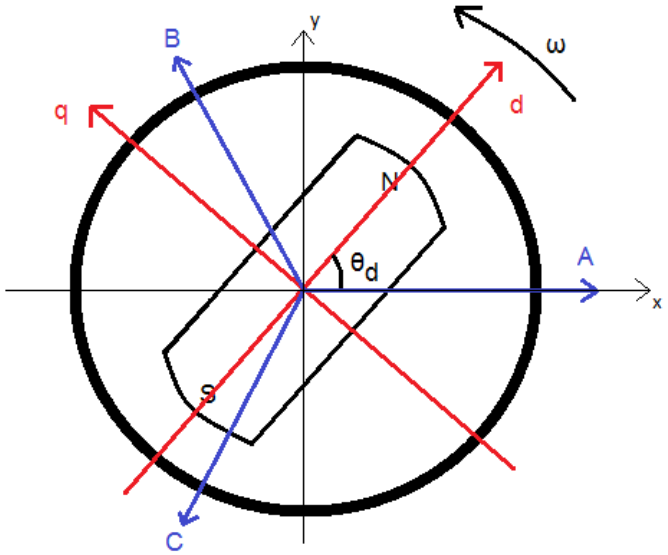

ω: flux electrical turn speed

θ_d: electrical angle between the d-axis and phase A.

A,B,C: three-phase system

Figure 3.1.2.1: ABC, xy and dq axes illustrated

Using geometry it is possible to define voltages in the xy-plane.

$$V_{xy} = V_x + jV_y = \frac{2}{3}\left((V_A - \frac{1}{2}V_B - \frac{1}{2}V_C) + j\left(\frac{\sqrt{3}}{2}V_B - \frac{\sqrt{3}}{2}V_C\right)\right) \quad (3.1.2.1)$$

[20]

Matrix form:

$$\begin{bmatrix} V_x \\ V_y \end{bmatrix} = \begin{bmatrix} \frac{2}{3} & -\frac{1}{3} & -\frac{1}{3} \\ 0 & \frac{1}{\sqrt{3}} & -\frac{1}{\sqrt{3}} \end{bmatrix} * \begin{bmatrix} V_A \\ V_B \\ V_C \end{bmatrix} \qquad (3.1.2.2)$$

The transformation from this point and into the dq-reference is just adding the angle between the xy-plane and the dq-plane part:

$$V_{dq} = V_d + jV_q = V_{xy}\, e^{-j\theta_d} = (V_x + jV_y)(\cos(\theta_d) - j\sin(\theta_d)) \qquad (3.1.2.3)$$
$$= V_x \cos(\theta_d) + V_y \sin(\theta_d) + j(-V_x \sin(\theta_e) + V_y \cos(\theta_d))$$

Matrix form:

$$\begin{bmatrix} V_d \\ V_q \end{bmatrix} = \begin{bmatrix} \cos(\theta_d) & \sin(\theta_d) \\ -\sin(\theta_d) & \cos(\theta_d) \end{bmatrix} * \begin{bmatrix} V_x \\ V_y \end{bmatrix} \qquad (3.1.2.4)$$

Using equation 3.1.2.2 in equation 3.1.2.4 gives the following matrix form:

$$\begin{bmatrix} V_d \\ V_q \end{bmatrix} = \frac{2}{3} \begin{bmatrix} \cos(\theta_d) & \cos(\theta_d - 120°) & \cos(\theta_d + 120°) \\ -\sin(\theta_d) & -\sin(\theta_d - 120°) & -\sin(\theta_d + 120°) \end{bmatrix} * \begin{bmatrix} V_A \\ V_B \\ V_C \end{bmatrix} \qquad (3.1.2.5)$$

We may also add the zero-sequence axis:

$$V_0 = \frac{1}{3} V_A + \frac{1}{3} V_B + \frac{1}{3} V_C \qquad (3.1.2.6)$$

"The zero-sequence component plays a relatively minor role in stability studies and hence is neglected in most introductory discussions of stability analysis." [19] If this axis is placed into figure 3.1.2.1 it would point out of the paper.

New matrix form:

$$\begin{bmatrix} V_d \\ V_q \\ V_0 \end{bmatrix} = \frac{2}{3} \begin{bmatrix} \cos(\theta_d) & \cos(\theta_d - 120°) & \cos(\theta_d + 120°) \\ -\sin(\theta_d) & -\sin(\theta_d - 120°) & -\sin(\theta_d + 120°) \\ \frac{1}{2} & \frac{1}{2} & \frac{1}{2} \end{bmatrix} * \begin{bmatrix} V_A \\ V_B \\ V_C \end{bmatrix} \qquad (3.1.2.7)\ [20]$$

$$= [\mathbf{T}_{dq0}(\theta_d)] * \begin{bmatrix} V_A \\ V_B \\ V_C \end{bmatrix}$$

This transform is known as Park's transform. The inverse of this transform is shown in equation 3.1.2.8.

$$[\mathbf{T}_{dq0}(\theta_d)]^{-1} = \begin{bmatrix} \cos(\theta_d) & -\sin(\theta_d) & 1 \\ \cos(\theta_d - 120°) & -\sin(\theta_d - 120°) & 1 \\ \cos(\theta_d + 120°) & -\sin(\theta_d + 120°) & 1 \end{bmatrix} \quad (3.1.2.8)$$

[20]

The dq0-plane may also be defined as a qd0-plane with the d-axis lagging the q-axis as illustrated in figure 3.1.2.2.

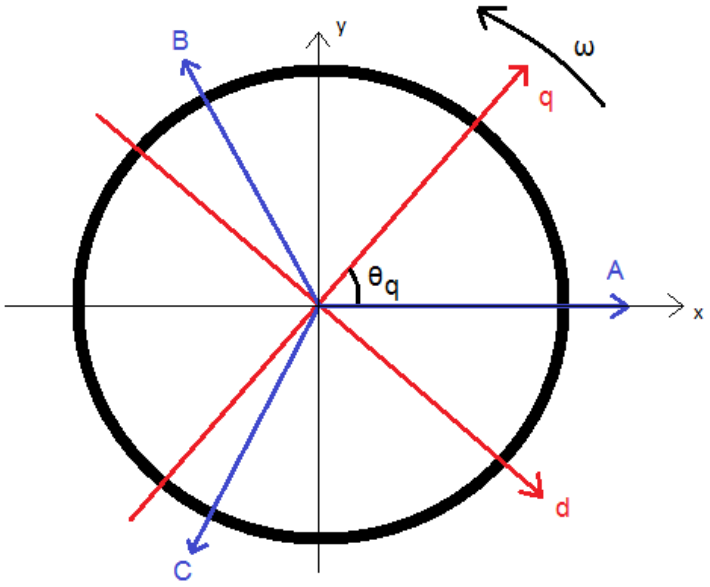

θ_q: electrical angle between the q-axis and phase A.

Figure 3.1.2.2: qd illustration

Defined as in figure 3.1.2.2, the qd0 transform, also known as modified Park's transform, looks like the following:

$$\begin{bmatrix} V_q \\ V_d \\ V_0 \end{bmatrix} = \frac{2}{3} \begin{bmatrix} \cos(\theta_q) & \cos(\theta_q - 120°) & \cos(\theta_q + 120°) \\ \sin(\theta_q) & \sin(\theta_q - 120°) & \sin(\theta_q + 120°) \\ \frac{1}{2} & \frac{1}{2} & \frac{1}{2} \end{bmatrix} * \begin{bmatrix} V_A \\ V_B \\ V_C \end{bmatrix} \quad (3.1.2.9)$$

$$= [\mathbf{T}_{qd0}(\theta_q)] * \begin{bmatrix} V_A \\ V_B \\ V_C \end{bmatrix}$$

[20]

The inverse:

$$[\mathbf{T}_{qd0}(\theta_q)]^{-1} = \begin{bmatrix} \cos(\theta_q) & \sin(\theta_q) & 1 \\ \cos(\theta_q - 120°) & \sin(\theta_q - 120°) & 1 \\ \cos(\theta_q + 120°) & \sin(\theta_q + 120°) & 1 \end{bmatrix} \quad (3.1.2.10)$$ [20]

"Modified Park's transform is more convenient for vector control than Park's transform as maximum phase induction occurs at when the angle is zero (θ_q=0)." [21] The transform is frequently used for motor controller purposes. See parts 5.1, 5.2.2 and 7.4.

3.1.3 The PMSM dq-model

Now it is possible to define a qd0 equivalent circuit model for the permanent magnet synchronous machine. The book "Dynamic Simulation of Electric Machinery using MATLAB/SIMULINK", [20], Section 7.9, defined the model as illustrated in figure 3.1.3.1 and equations 3.1.3.1-13.

Figure 3.1.3.1 represents the different equivalents for the q, d and zero-sequence axis for a permanent magnet synchronous motor with one damper winding circuit on both the d- and q-axis.

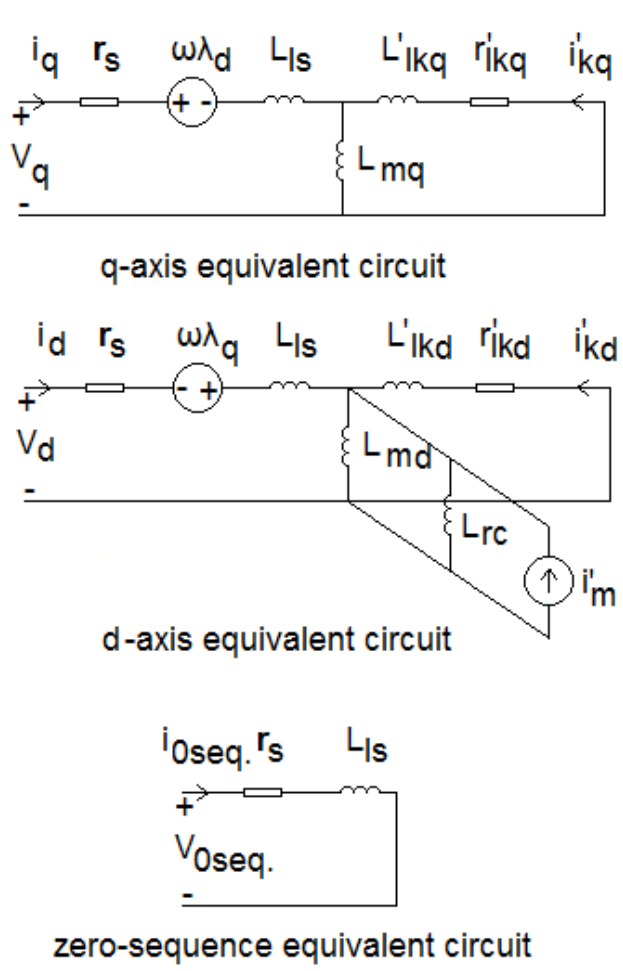

Figure 3.1.3.1: PMSM dq equivalent circuit [20]

If the parameter is marked with a ' it means that it is referred to stator.

V_q: q-axis voltage equivalent
V_d: d-axis voltage equivalent
$V_{0seq.}$: zero-sequence voltage equivalent

i_q: q-axis current equivalent
i_d: d-axis current equivalent
$i_{0seq.}$: zero-sequence current equivalent
i'_{kq}: q-axis damper winding current
i'_{kd}: d-axis damper winding current
i'_m: equivalent magnetizing current

r_s: stator winding resistance
r'_{lkq}: q-axis damper winding resistance
r'_{lkd}: d-axis damper winding resistance

λ_q: q-axis flux linkage
λ_d: d-axis flux linkage

L_{ls}: stator leakage inductance
L'_{lkq}: q-axis damper winding leakage inductance
L'_{lkd}: d-axis damper winding leakage inductance
L_{mq}: q-axis mutual inductance
L_{md}: d-axis mutual inductance
L_{rc}: permanent magnet inductance

The circuits in figure 3.1.3.1 are supplemented by the following equations:

qd0 Voltage equations [V]:

$$V_q = r_s i_q + \frac{d\lambda_q}{dt} + \lambda_d \frac{d\theta_q}{dt} \quad (3.1.3.1)$$

$$V_d = r_s i_d + \frac{d\lambda_d}{dt} - \lambda_q \frac{d\theta_q}{dt} \quad (3.1.3.2)$$

$$0 = r'_{kq} i'_{kq} + \frac{d\lambda'_{kq}}{dt} \quad (3.1.3.3)$$

$$0 = r'_{kd} i'_{kd} + \frac{d\lambda'_{kd}}{dt} \quad (3.1.3.4)$$

$$V_0 = r_s i_0 + \frac{d\lambda_0}{dt} \quad (3.1.3.5)$$

Flux linkage equations [Weber-turn]:

$$\lambda_q = L_q i_q + L_{mq} i'_{kq} \quad (3.1.3.6)$$

$$\lambda_d = L_d i_d + L_{md} i'_{kd} + \lambda'_m \quad (3.1.3.7)$$

$$\lambda_m = L_{md} i'_m \quad (3.1.3.8)$$

$$\lambda_0 = L_{ls} i_0 \quad (3.1.3.9)$$

$$\lambda'_{kq} = L_{mq} i_q + L'_{kqkq} i'_{kq} \quad (3.1.3.10)$$

$$\lambda'_{kd} = L_{md} i_d + L_{kdkd} i'_{kd} + \lambda'_m \quad (3.1.3.11)$$

[20]

Electromagnetic torque [Nm]:

$$\tau_e = \frac{3}{2}\frac{P}{2}\left(\lambda_d i_q - \lambda_q i_d\right)$$

$$\tau_e = \frac{3}{2}\frac{P}{2}\left(L_d - L_q\right) i_d i_q + \frac{3}{2}\frac{P}{2}\left(L_{md} i'_{kd} i_q - L_{mq} i'_{kq} i_d\right) + \frac{3}{2}\frac{P}{2} L_{md} i'_m i_q \quad (3.1.3.12)$$

[20]

$$\tau_e = \tau_{reluctance} + \tau_{induction} + \tau_{excitation} \quad (3.1.3.13)$$

[20]

L_q: q-axis synchronous inductance (= L_{mq} + L_{ls})
L_d: d-axis synchronous inductance (= L_{md} + L_{ls})
L'_{kqkq}: q-axis damper winding self-inductance
L'_{kdkd}: d-axis damper winding self-inductance
λ_{kq}: q-axis damper winding flux linkage
λ_{kd}: d-axis damper winding flux linkage
λ_0: zero-sequence-axis flux linkage
λ_m: flux linkage provided by permanent magnets

The PMSM dq model is very useful for analysing the different effects caused by motor design and operation. Some design factors are discussed in part 3.2. The effect of the d- and q- axis current is discussed in part 5.1. The effect of damper winding equivalents are neglected in analysis presented in this thesis. The circuit diagram change based on this assumption is shown in part 3.1.4.

3.1.4 SimPowerSystems PMSM model

How the SimPowerSystems [4] PMSM model block is built up mathematically will now be presented.

The model is made up of two parts. The mechanical part and the electrical part. The mechanical part of the model is described by equations 3.1.4.1-2.

$$\frac{d}{dt}\omega_m = \frac{1}{J}(T_e - T_f - D_d\omega_m - T_m) \qquad (3.1.4.1)$$ [21]

Equation 3.1.4.1 is Newton's second law, equation 3.1.1.5, with shaft static friction torque (T_f) included as an individual parameter.

The relation between rotor position and rotor speed is also included:

$$\frac{d\theta_m}{dt} = \omega_m \qquad (3.1.4.2)$$ [21]

The electrical part of the model varies with the assumed magnetic flux distribution and number of phases. For the three-phase sinusoidal model the following equations apply:

$$\frac{d}{dt}i_d = \frac{1}{L_d}V_d - \frac{r_s}{L_d}i_d + \frac{L_q}{L_d}\frac{P}{2}\,\omega_m\, i_q \qquad (3.1.4.3)$$ [21]

$$\frac{d}{dt}i_q = \frac{1}{L_q}V_q - \frac{r_s}{L_q}i_q - \frac{L_d}{L_q}\frac{P}{2}\,\omega_m\, i_d - \frac{\lambda_m\,\frac{P}{2}\,\omega_m}{L_q} \qquad (3.1.4.4)$$ [21]

$$T_e = 1.5\,p\,[\lambda_m i_q + (L_d - L_q) i_d i_q] \qquad (3.1.4.5)$$ [21]

The equations above are similar to the equations shown in equations 3.1.3.1-11. They are the same if the rotor damper windings are neglected, or assumed not existing, and the voltage equations are combined with the flux linkage equations. Figure 3.1.4.1 illustrates how the dq-equivalent circuit could look based on equations 3.1.4.3-5.

Note that $L_d = L_{md} + L_{ls}$ and $L_q = L_{mq} + L_{ls}$. See [14].

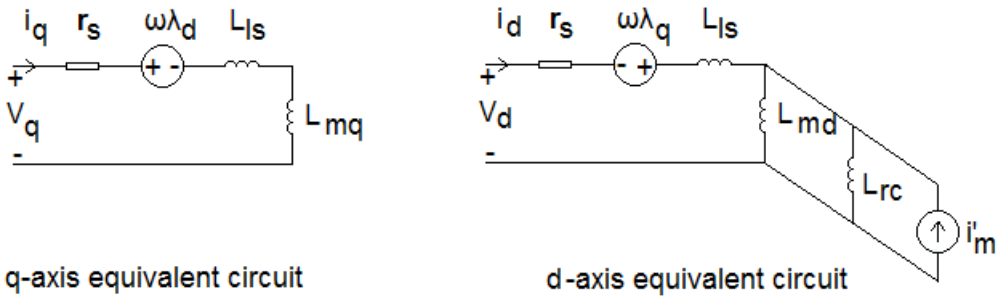

Figure 3.1.4.1: SimPowerSystems PMSM block dq-model equivalent circuit

The SimPowerSystems PMSM model block was used for the model simulations. See part 7.2.1.

3.2 PMSM design configurations

There are many design configurations which alters the shape and function of the PMSM dramatically. The standard design configuration is a stator surrounding a rotor as shown in figure 3.2.1.

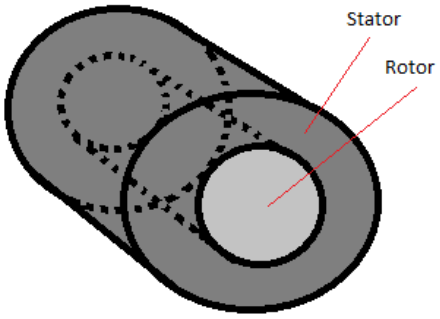

Figure 3.2.1: Rotor inside a stator design [18]

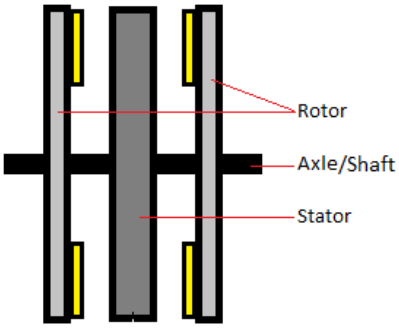

Figure 3.2.2: Axial flux design [18]

The advantage with this design is that the stator shields the moving rotor from the surroundings. [18] This is not the only possible way of constructing a PMSM. It is also possible to have an axial flux configuration as illustrated in figure 3.2.2.

The advantage with the axial flux design is, for example, using it as an in-wheel motor in a vehicle which allows a mechanical transmission free design between the wheel and machine. This kind of design is good for situations where the axial length of the machine is to be minimized. There are two rotors in order to balance the forces between stator and rotor. It is also possible to use two stators and one rotor instead.

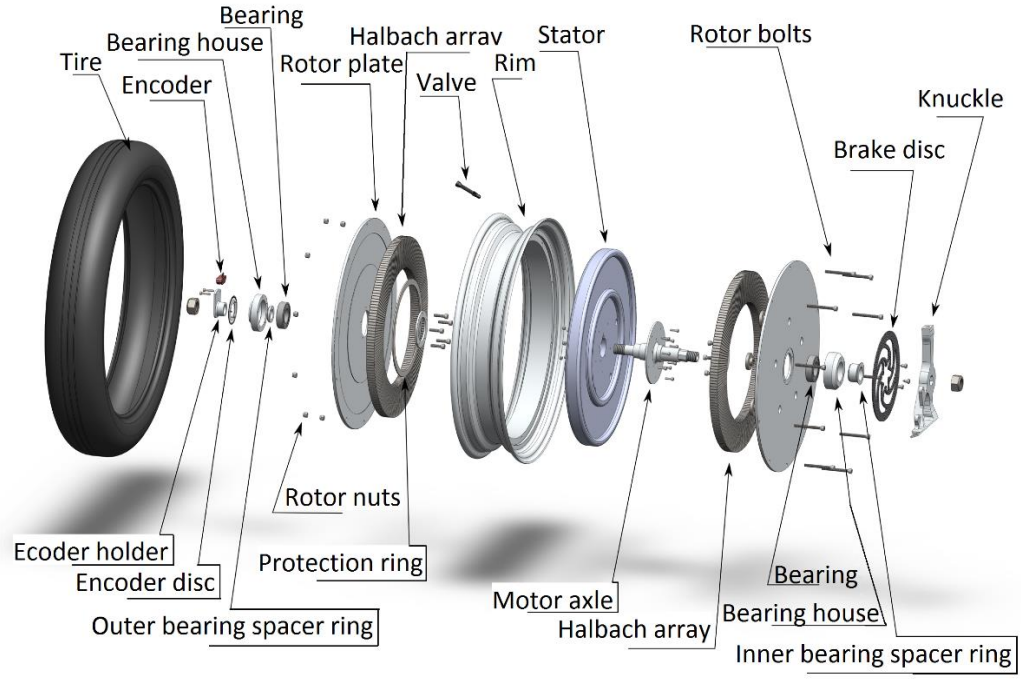

Figure 3.2.3: 2013 axial flux in-wheel motor design component illustration [12] *(edited)*

The axial flux configuration is not as simple to build as figure 3.2.2 may have you believe. Figure 3.2.3 illustrates all of the parts that the 2013 DNV GL Fuel Fighter team had to make in order to create their axial flux in-wheel motor.

Figure 3.2.3 also illustrates the encoder including the encoder mount used in 2013. More on that in part 6.3.1. The magnet rings are named “Halbach array” in figure 3.2.3. It is a way of arranging the magnet polarities for increased back induced voltage and reduced required magnetic capability of the rotor plates. This design feature is possible for both radial and axial flux machines. In the 2013 axial flux machine, part 3.3.1.2, 45 degree Halbach array was used. This array is illustrated in figure 3.2.4:

Figure 3.2.4: 45 degree Halbach array magnet arrangement as in the 2013 axial flux motor [22]

In both axial flux machines that will be studied in this thesis surface mounted magnets are used. It is assumed that both of the radial flux motors has this design feature as well as it is the most usual configuration for PMSMs. Magnets has almost the same permeability as air. This means that the reluctance in the motor air gap, seen from a stationary point in the stator, does not change with rotor position. See [14] for a more detailed description.

Due to reluctance variation, because of rotor teeth and other unsymmetrical geometries in stator, an alternating reluctance force is produced. This is called cogging. The cogging part of the forces acting between rotor and stator ($F_{x,cog.}$) is given in equation 3.2.1:

$$F_{x,cog.} = -\frac{1}{2}{\varphi_g}^2\frac{d\Re}{dx} \qquad \varphi_g\text{: air gap flux} \qquad (3.2.1)$$ [18]

Theory involving mathematical modelling of reluctance was described in part 3.1.1. Cogging is often related to vibrations and a large starting torque load in PMSMs that are designed poorly. The number of slots in the stator compared to the number of magnet poles is a crucial factor. It is possible to have a number of slots which causes the sum of cogging force on each stator tooth to be zero in total. This is not done for the AXI motor design, part 3.4.1.2, as it has a huge cogging force present.

3.3 Urban concept vehicle motor selection

3.3.1 Available motors

3.3.1.1 2011 axial flux motor

The 2011 axial flux in-wheel permanent magnet synchronous machine was kind of a mystery at first. It was first built for the 2010 Shell Eco-Marathon, but that year the team had zero valid attempts. See the competition result history at [7]. The first design had rotor plates made out of plywood. With magnets fixed to an iron ring. [23] For the 2011 competition the next team improved the motor, but mostly mechanical aspects as the team was lacking students doing electrical studies. [24] Test results from the 2010 thesis claims that the motor had an efficiency of 90% when operated at optimal conditions. [23]

Figure 3.3.1.1.1: 2011 axial flux motor [24]

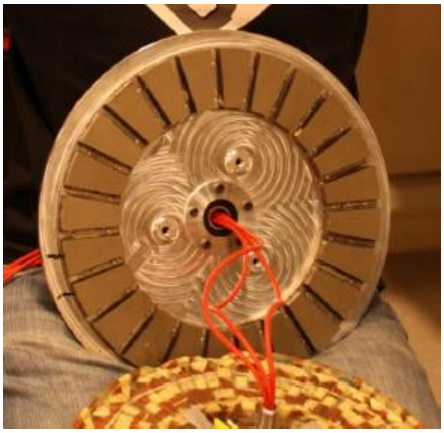

Figure 3.3.1.1.2: 2011 axial flux motor with rotors and stator separated [24]

Figures 3.3.1.1.1-2 clearly illustrates what the motor looks like completely assembled as well as separated. In figure 3.3.1.1.2 it is shown that the unreliable plywood rotor plates have been replaced by Alumec 89 by the 2011 team. [24] From the same figure it is also possible to see the pole number of the motor by counting the number of magnets. Thus the pole number of the motor is 24. This number is very important for motor control purposes as it is the link between mechanical and electrical frequency/speed. See part 5.5.

The motor proved to be fully functional. See part 8.2 and 8.5. It ended up being the motor used for SEM 2014. However, some concern was raised considering sudden changes in rotor position. It could be caused by either sudden slip in the stator or an encoder fault. See part 9.5 for more on this issue.

3.3.1.2 2013 axial flux motor

The design of the 2013 axial flux motor is based on a master thesis written by Lubna Nasrin [25] in the spring semester of 2011 which greatly improves the efficiency potential of this type of motor. The building process was actually started by the 2012 team, but it was not finished in time for SEM 2012. The task was handed on to John Ola Buøy, member of 2013 DNV GL Fuel Fighter team. He finished the motor in time for SEM 2013 competition. See [22] for the full master thesis on the motor production and analysis.

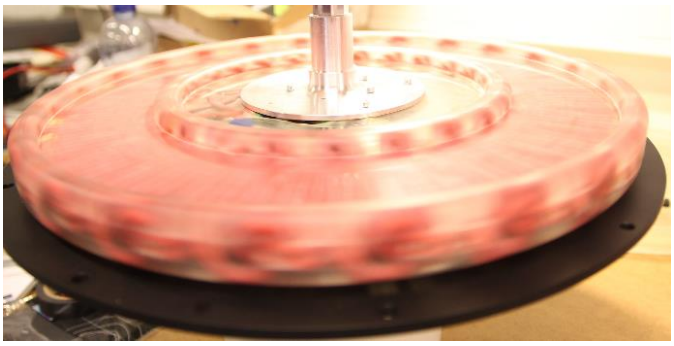

Figure 3.3.1.2.1: 2013 axial flux motor stator [12]

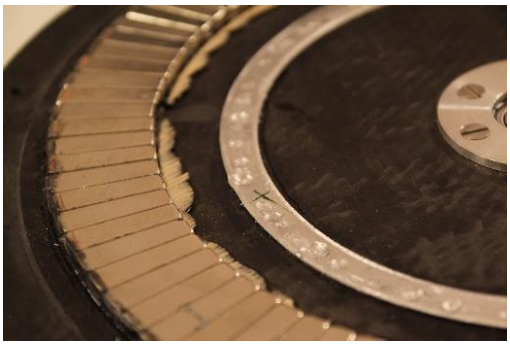

Figure 3.3.1.2.2: 2013 axial flux motor rotor [12]

Figures 3.3.1.2.1-2 illustrates the stator and rotor of the motor. There are several solutions to this designs which increases its overall efficiency compared to the 2011 axial flux motor:

Litz wires in stator	Reduces the armature resistance due to reduced skin effect. See [14] or [22].
Carbon fibre rotor plates	Reduced weight.
45 degree Halbach array	Increases the induced voltage. See part 3.2 and [22].
Better stator production methods	Properly aligned stator wires means higher efficiency.

List 3.3.1.2.1: 2013 axial flux motor design advantages

Not as accurate testing, compared to the 2011 axial flux tests, was done in 2013 on this machine due to time issues, but the tests that were done implied an efficiency as high as 97%. However, the greatest strength of the motor design also proved to be the greatest weakness. Due to the 45 degree Halbach array feature magnets with almost the same polarity direction had to be glued next to each other. This means that magnetic forces will always try to separate the magnets. Unfortunately the glue that held the magnets in place proved to be too weak. See part 8.1. Magnets already started to get loose during SEM 2013 and at the start of the spring semester 2014 a lot more fell off. Due to this the seemingly more efficient axial flux motor was not used during SEM 2014 as it was not operational.

3.4 Prototype vehicle motor selection and gear solution

3.4.1 Available motors

3.4.1.1 EC 60 flat motor

The EC 60 flat 100W brushless DC motor, [26] #412825, was ordered by the 2014 team short time before the thesis work was started. Brushless DC is a confusing term as one would believe that such a motor operates on DC power supply. The truth is that this motor runs on 3-phase AC power and is practically the same as a permanent magnet synchronous machine. Figure 3.4.1.1.1 is the illustration of the motor given by the producer, Maxon motor [27]. The motor datasheet is found at [26]. An advantage with this motor is that it is very lightweight: 470g according to the datasheet.

Figure 3.4.1.1.1: EC 60 flat motor [27]

As the rating of this motor is very low, only 100W, it was uncertain if the motor would be able to withstand the loads needed to accelerate the vehicle. In worst case scenario the motor would fail during a SEM 2014 attempt. Thus proper testing had to be done. A simulation model was developed early in order to have some idea of how the motor would perform and how much load it would have to withstand. See chapter 7. When the motor finally arrived it was connected to the motor test rig which was developed. This is described in part 8.6.

The simulation results did not bring any good news for the motor as a very slow acceleration was required in order to be anywhere near its rated area of operation. And when it was connected and tested on the motor test rig the insulation between the windings seemed to have burned up, after being operated with medium load. As there was ordered only one of this motor, which now was defect, it could not be used for SEM 2014. Please see the simulation part and the test rig part as mentioned above for more info.

3.4.1.2 AXI motor

Luckily two identical AXI 5360/20 brushless DC motors was found, while cleaning up the DNV GL Fuel Fighter workshop at the start of the 2014 spring semester. Having two of the same motor meant that there would be one spare motor ready if the first one breaks down. It also meant that one could be used for testing while the other was put in the prototype vehicle. This motor was used during SEM 2008 when the team, at the time called PureChoice, achieved 2nd place in the urban concept hydrogen/fuel cell class. As mentioned in part 3.4.1.1 a brushless DC motor is basically the same as a permanent magnet synchronous machine.

Figure 3.4.1.2.1: AXI 5360/20 motor [28]

AXI 5360/20 GOLD LINE	Order no. 536020
No. Of cells Betriebsspannung / Počet článků	10s Li-Polv
RPM/V / Drehzahl/Volt / Ot./V	120
Max. efficiency / Max. Wirkungsgrad / Max. účinnost	94 %
Max. efficiency current Strom bei max. Wirk. / Proud při max. účinnosti	20 - 59 A (> 85 %)
Current capacity / Max. Strom / Max. zatížitelnost	65 A / 30 s
No load current / Leer Strom / Proud na prázdno 30 V	1,8 A
Internal Resistance / Innenwiderstand Ri / Vnitřní odpor Ri	68 mΩ
Dimensions (Ø x L) / Abmessungen / Rozměr	89x94 mm
Shaft diameter / Achsdurchmesser / Průměr hřídele	8 mm
Weight with cables / Gewicht / Hmotnost vč. kabelů	1350 g

Figure 3.4.1.2.2: AXI 5360/20 motor datasheet [28]

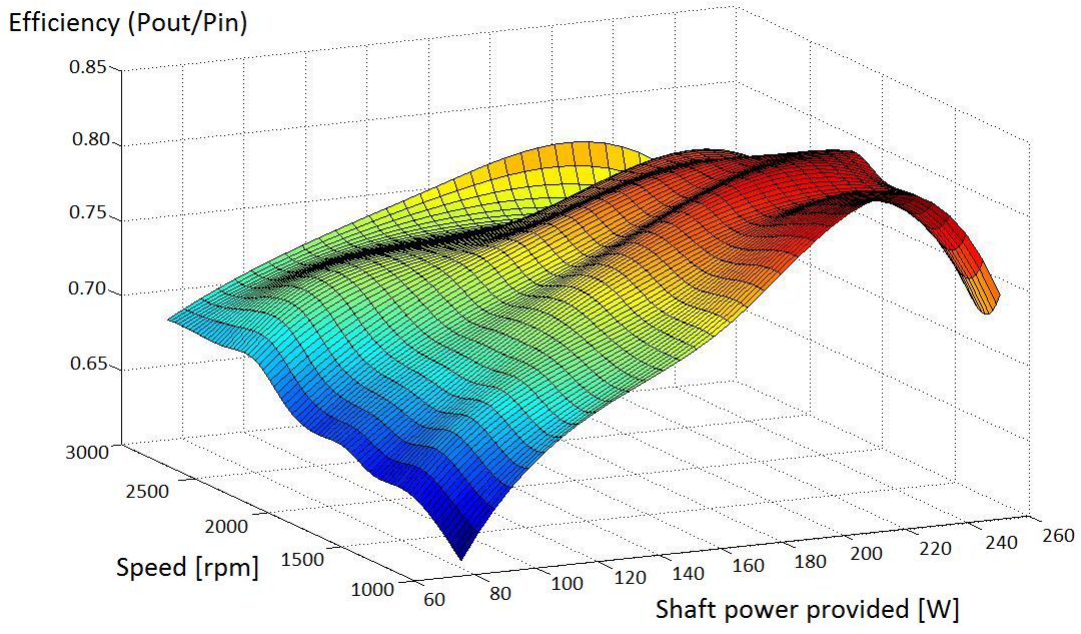

Figure 3.4.1.2.3: AXI 5360/20 motor 3D efficiency diagram [28] *(edited)*

The engineering student Bjørn Ola Wiik, from the department of Electric Power Engineering, wrote a master thesis on several different motors for the Shell Eco-Marathon. See [28]. He ended up choosing the AXI motor for its light weight and high efficiency. The AXI motor is actually made for model airplanes. Thus the weight has to be low in order to fly and the efficiency high in order to get maximum air time.

A similar efficiency test to the one that would be done for the 2011 axial flux motor, part 8.5, was already done in 2008. This result is illustrated in figure 3.4.1.2.3. The 3D efficiency diagram shows that the AXI motor works most efficient while providing about 200W at a speed range from 2000 to 1000 rpm. The efficiency of the motor is not that good. A more efficient motor should be found for SEM 2015.

As the AXI motor has 14 poles and 12 slots [28] it has a significant cogging effect. See part 3.2 for the cogging theory. This cogging effect is undesirable as it introduces vibrations, which may lead to worse effects like resonance. This actually happened to the motor test rig. See part 8.7. Cogging also introduce the need for a greater force just to get it to start rolling. Reduced rolling capability of the prototype vehicle was observed after connecting the motor. In order to counter this effect the team changed the gear to another type that slips when forces act the opposite way of the forward direction. More on that in part 9.1.

3.4.2 Gear configuration

The mechanical part of the 2014 team was responsable for the gear and the motor mount which is illustrated in figure 3.4.2.1, but some inputs had to be given from the electrical side in order to create a suitable gear configuration.

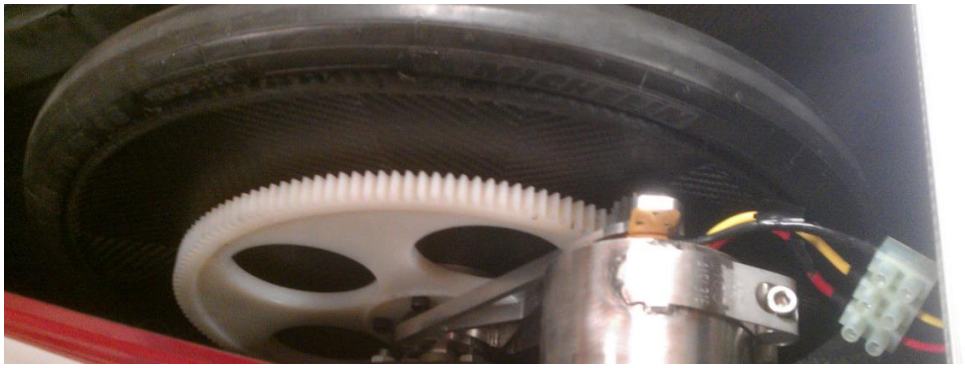

Figure 3.4.2.1: Motor mount and gear on the back wheel of the prototype vehicle

The gear ratio had to be adapted to the rated speed of the motor relatively to the average speed of the vehicle. At the time of gear production the team did not know for sure which of the two motors, the AXI or the EC 60 flat, that would be used in the prototype vehicle, but as there had been a lot of doubt already that the EC 60 flat motor would survive testing and driving it was decided to go for the optimal AXI motor gear configuration. Bjørn Ola Wiik had already done this analysis in 2008 for his master thesis. He chose a 1:10 ratio based on calculations and the efficiency diagram produced. [28] The same ratio was therefore implemented for the 2014 prototype vehicle gear configuration.

Chapter 4: Inverter board theory and production

In this chapter the inverter is presented. It starts off with some basic theory of the main components, how they are connected and how it works. Eventually an inverter circuit board was built. The production process of this circuit board is also described in this chapter.

4.1: Inverter theory

Most of the theory presented in this part is based on theory presented and knowledge gained from the book "Power Electronics" [29] by Mohan, Undeland and Robbins.

Figure 4.1.1 illustrates the three-phase inverter circuit. It may also be referred to as a two-level three-phase voltage source converter (VSC). A, B and C indicates the three-phase output and V_d indicates the DC voltage input. There are in total of six switches in the circuit. Each connected in parallel with a diode. For each phase there are two sets. One for positive and one for negative voltage input. The diodes operate when the current, in that part of the circuit, goes in the opposite direction of the battery. If MOSFETs are used in the circuit then they represent both the switch and the diode in this circuit as the body diode of a MOSFET allows blocking in only one direction. It is not unusual to observe a higher current in the AC part of the circuit than the DC part as circulating currents occur frequently. The capacitors connected to the DC side is there to handle ripple current.

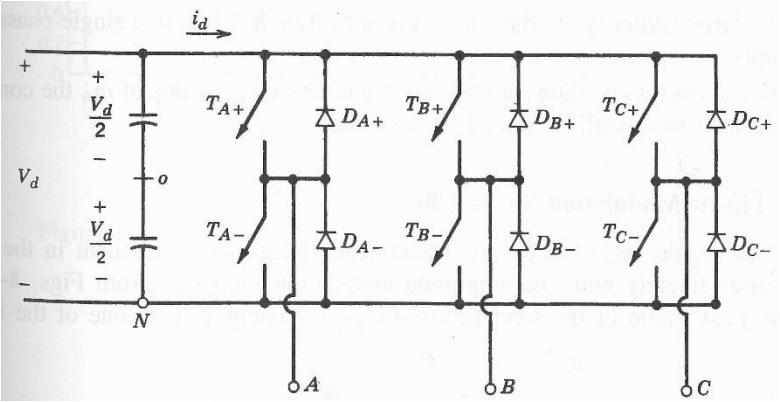

Figure 4.1.1: Three-phase inverter circuit [29]

The on/off signal to the transistors, also known as pulses, may be generated by a pulse width modulation (PWM) algorithm. By generating a triangle signal and comparing the sinusoidal control voltage signal the pulse sequence is generated. Figure 4.1.2 illustrates this process. When the phase control voltage signal is greater than the triangle signal the upper (high side) transistor for that phase, in figure 4.1.1, closes and the maximum voltage is applied. For the opposite situation the lower (low side) transistor is the one that is closed while the upper is open and the minimum voltage is applied. This logic was implemented in the simulation model in part 7.3.1. Figure 4.1.2 (b) illustrates the generated fundamental voltage component between phase A and phase B. The frequency of the triangle signal regulates the

switching frequency of the circuit as the number of crossings between the control signal and the triangle signal for a given time period increases with the frequency of the triangle signal.

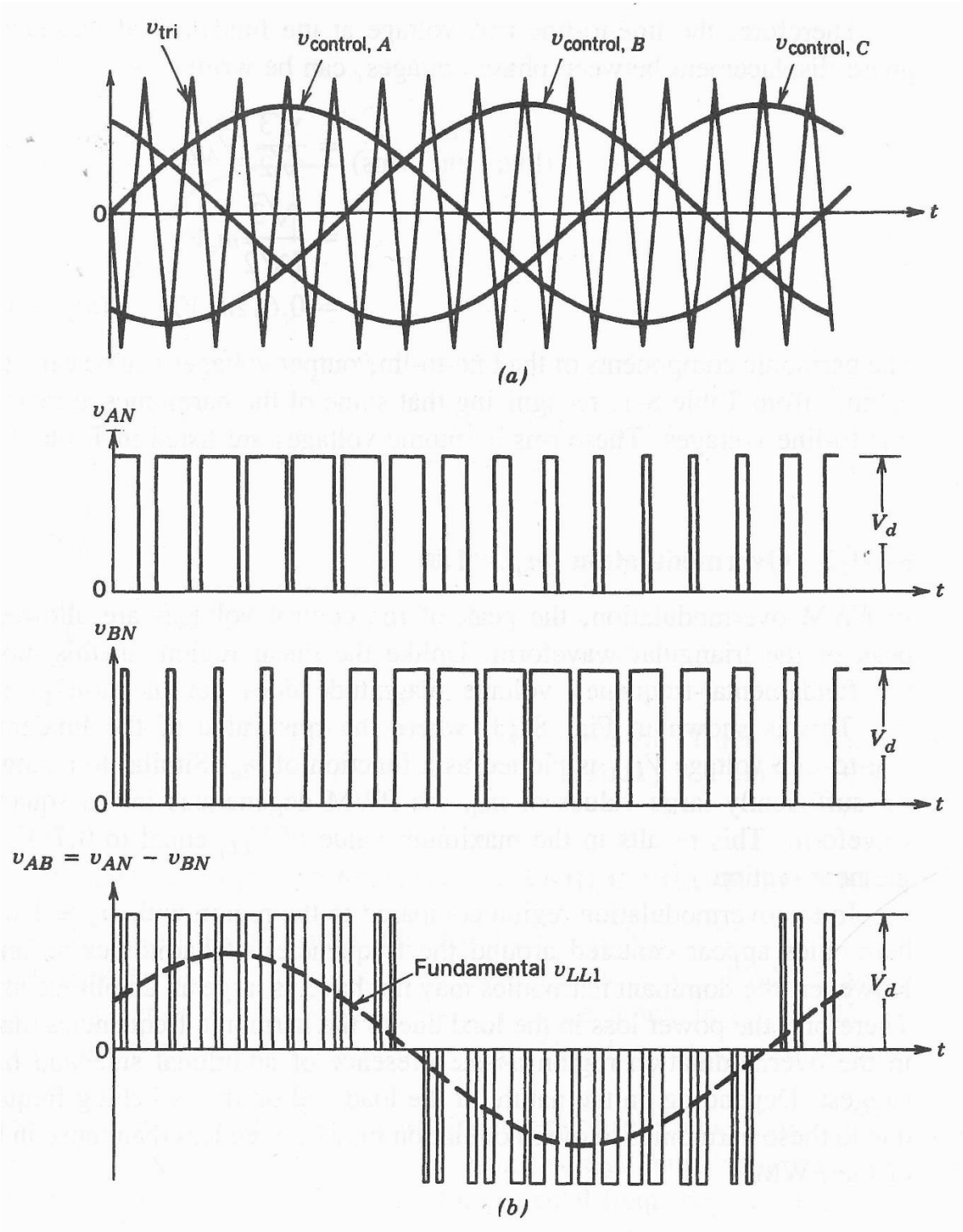

Figure 4.1.2: PWM pulse signal generation and the fundamental voltage component [29]

The pulses given from the logic circuit is not enough for controlling the switching behaviour of a transistor alone. Transistor drive circuits are necessary between the control algorithm signal and the transistors. More on that subject in part 4.2.

In order to choose the proper transistor type for the inverter circuit board the expected electrical conditions has to be taken into account. Figure 4.1.3 shows a diagram which illustrates the capabilities when it comes to switching frequency, voltage and current for different types of semiconductors. MOSFETs and IGBTs are the most relevant transistors for this thesis. By investigating the diagram it is revealed that MOSFETs are best suited for low power applications with high switching frequencies and the IGBTs are suited for higher power purposes with lower switching frequency capabilities.

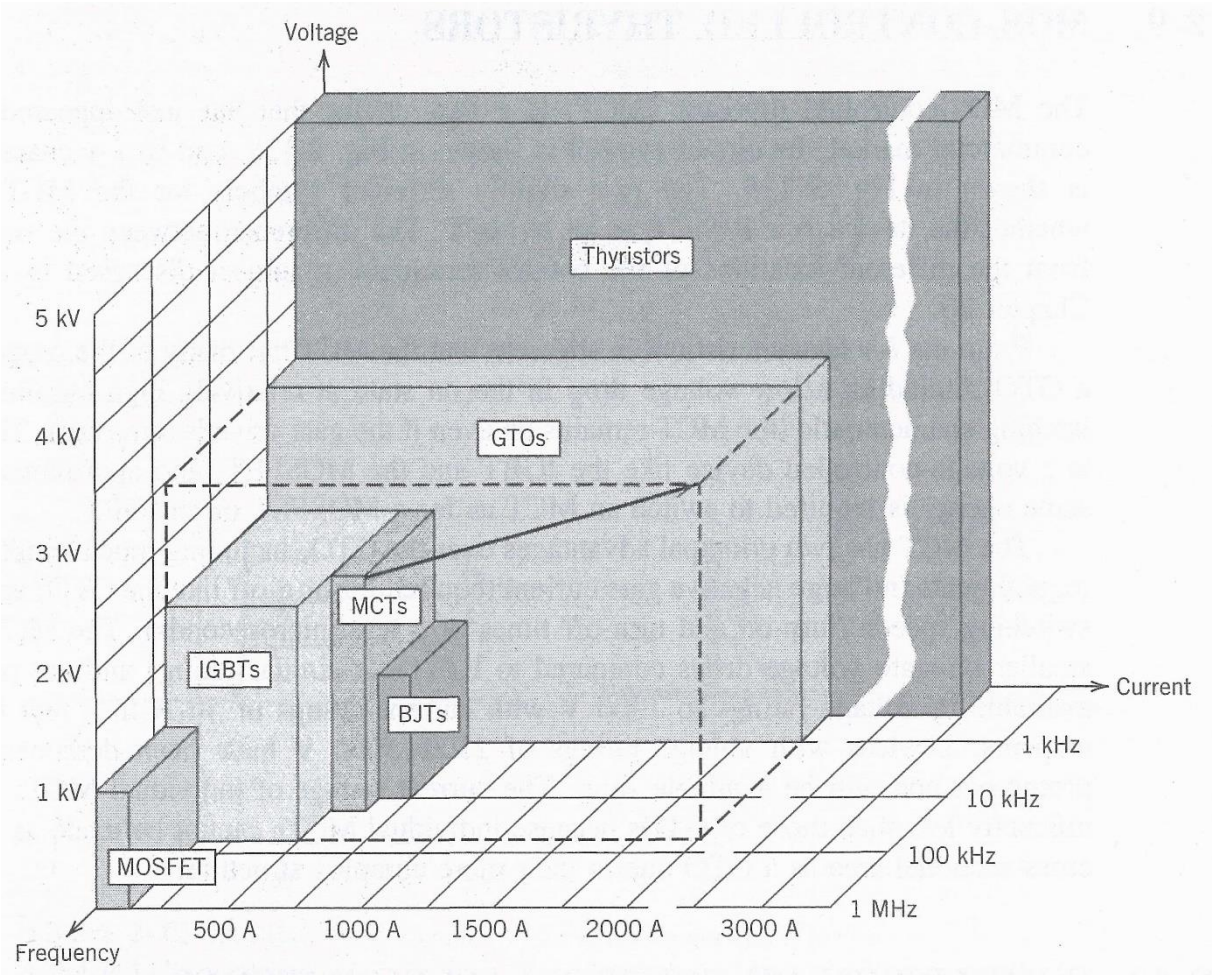

Figure 4.1.3: Diagram illustrating the different semiconductor device capabilities [29]

4.2 Considered inverter circuit options

During the initial process of this thesis several different inverter circuit solutions was considered. Several applicable inverter solutions was found. Especially in the International Rectifier (IR) [30] on-line product list there was a lot of components that could be used for the inverter purpose. List 4.2.1 mentions a few of these possibilities:

Inverter solution:	**Product examples:**
Using three MOSFET gate drivers with both high and low side output to control 6 transistors.	IR2101 [31] or similar.
Using one three-phase gate driver to control 6 transistors.	IRS2336D [32], IRS26310DJPbF [33] or similar.
Using a full inverter circuit IC or circuit board.	IRAM136-3023B [34], IRMDKG6-400W [35] or similar

List 4.2.1: Other considered inverter options

What was decided, in the end, was actually to use the ACPL-333J [36]. It is an IGBT gate driver optocoupler, but it works just as well for MOSFETs. It only provides control for one gate. So six of them were needed in order to control all transistors. The optocoupler feature means that the signal and power supply of the gate driver is connected optically. This way the component isolates the signal side of the circuit from the power electronics side. Other external optocouplers was also used to isolate other parts of the circuit. The gate driver also provides other features like integrated desaturation detection, fault status feedback, active miller clamp and auto-fault reset. [36] The active miller clamp prevents unwanted turn on while switching. [37] More on the circuit safety features is found in part 4.3.2.2.

If the inverter circuit board production failed or was delayed at any point in the process it was important to have a plan B ready. Transistor gate drivers for a 22kW IGBT inverter circuit was available and would be used if the original plan failed.

4.3: Inverter circuit board documentation, production process and result

4.3.1 Documentation

Creating an inverter circuit board may seem like an easy job at first, but there are several factors, other than just turning six transistors on and off, that has to be implemented in the design. Here are some examples which were of major importance:

1. The inverter board must be reliable.
2. Produce proper feedback and action when something goes wrong.
3. Be compatible with the FPGA board hardware and software.
4. Produce correct measurements for the controller.

List 4.3.1.1: Important factors for the inverter circuit board design

These factors requires a whole new level of expertise. Luckily Kjell Ljøkelsøy, an employee at SINTEF Energi [11] and also the co-supervisor for this thesis, decided to step in and provide the necessary documentation for the inverter circuit board.

The full inverter board documentation document is not provided in this thesis. Please see [37]. It contains board layout, component list, circuit diagrams, descriptions and other relevant information.

In the documentation it was specified that the letters “SEM” had to be printed on the circuit boards as it was stated as a requirement in the SEM 2014 rules. See part 2.2.2. The end result had “SEM” printed both on the board in white and in the circuit board copper.

4.3.2 Circuit board components and features

4.3.2.1 Component ordering process

A lot of the time and effort spent on this thesis went to the realization of the inverter circuit boards. The first step was to acquire the needed electric components that was listed in the documentation.

Noca [38] had agreed to solder the components to the circuit boards as a sponsoring agreement to the project, see part 4.3.5. Many of the components needed for the circuit this firm already had in stock. Therefore the firm component stock list had to be compared with the component list provided in the board documentation. The excel sheet for the stock comparison and further ordering status, including product web links or product number, for the parts that were not in stock, is found in appendix E and on the DNV GL Fuel Fighter team 2014 server.

4.3.2.2 Board features, component descriptions and decisions

Board status is indicated with three different LED signals: “Fail”, “OK” and “ON”.

Figure 4.3.2.2.1: Inverter LED illustration

If any on the safety features on the board triggers the gate drive signals are blocked and the LED indicating a fault is activated. The “OK” signal only indicates that the system is ready, but the gate drives are still blocked in order to avoid unintentional switching. The system has to receive a separate “ON” signal from the controller in order to be operational. This is done through the same cable as the pulses. Initial testing on the inverter circuit board indicated that the “Fail” and “OK” signal had to be swapped. See part 8.9.

List 4.3.2.2.1 mention some of the safety features:

1. Trips when overheating.
2. DC over voltage tripping.
3. Short-circuit tripping.
4. Blocking signal input from battery contactor.
5. Delay between high and low side gate driver signal prevents short-circuit.
6. Driver supply under voltage tripping.

List 4.3.2.2.1: Inverter board safety features

As will be described in part 4.3.6 a PTC thermistor, [39], was mounted on the heat sink is the component that trips the circuit when overheating occur. The desaturation function in the gate driver optocoupler described in part 4.2 is the feature that enables tripping if a short-circuit condition occurs. The Dubox connection named "X6" on the circuit board may be connected to the main battery switch in order to provide a blocking signal when the battery is disconnected. Some issues and solutions concerning this feature is described in part 9.4.

Some effort was put into choosing appropriate transistors for the inverter purpose. Thus the transistors with the lowest expected losses was of main interest. First it had to be decided what kind of transistors that were to be used. As the transistors were to be used in a relatively low power application MOSFETs was chosen rather than using IGBTs. See figure 4.1.3. Tore M. Undeland, professor in the department of electric power engineering, NTNU, recommended finding a MOSFET with high current rating as that would mean that the current used was relatively small. Leading to a minimized conduction loss. The voltage rating should be low, as the efficiency of the transistor drops with increased voltage rating. It should also be noted that switching losses increase proportionally with voltage applied. The body diode is also a very important factor to consider when choosing a suitable MOSFET. This part of the MOSTFET description is often left out of the datasheet. A very good sign is therefore when the producer chooses to include this information because it means that the body diode is good enough for the buyer to see.

Three different MOSFETs types was bought. All from different producers. See list 4.3.2.2.2.

1. FDP032N08: 75V, 235A, 3.2mΩ, N-channel MOSFET by Fairchild Semiconductor [40]
2. IRFB3077PbF: 75V, 210A, 3.3mΩ, N-channel MOSFET by International Rectifier [41]
3. STB75NF75: 75V, 80A, 9.5mΩ, N-channel MOSFET by STMicroelectronics [42]

List 4.3.2.2.2: The three different MOSFETs bought for the thesis work

All of the MOSFETs chosen had a voltage rating of 75V because a lower voltage rating than that would come too close to the maximum voltages in the circuit when considering that voltage spikes would occur. The original plan was to have enough time to test all of the different MOSFETs mounted on separate, but identical, inverter circuit boards and find out which MOSFET that was the most efficient. Unfortunately time pressure did not allow this to

be done. See part 4.3.6 to find out which MOSFET that were used on the inverter circuit boards.

Both the needed DC voltage and the three-phase AC current measurement was done by components on the inverter circuit board. The DC voltage measurement is done with an optocoupler in combination with a RC circuit and a differential amplifier. The circuit is isolated from the power circuit because of the optocoupler. The current measurement is done with three LEM current measurement devices which acts just like small transformers with a 1:1000 transfer ratio and a nominal output signal of 25 mA. [37] Because of the very nature of the transformer configuration this output is also isolated from the power circuit. Both the voltage and current measurement has to be calibrated with the FPGA software. See list 5.5.1.

4.3.3 Printed circuit board layout

Documentation and circuit drawings are not enough data for producing the printed circuit boards (PCBs). A proper layout of the circuit boards had to be made. The printed circuit board layout design was done by Midcom [43].

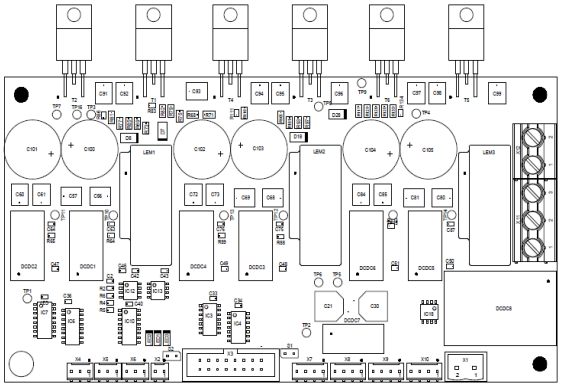

Figure 4.3.3.1: Inverter circuit board assembly drawing, top side [37]

Creating the lay out for a PCB involves ensuring proper insulation between the different power and signal circuits. All of the different components has to be placed in such a way that the insulation is good enough and so that it is possible for all conducting paths to go where they should without crossing each other. The circuit board has more than one layer and has components on both sides in order to cope with this challenge.

The final result from the job is a set of computer files suited for the machines that would eventually produce the PCBs. These files are accessible on the DNV GL Fuel Fighter, team 2014 server. Contact the current team for access. The files may be opened with Cadstar [6], which shows the different conducting pathways, layers, drill holes, etc.

4.3.4 Printed circuit board production

When the circuit board lay out files was finished they were sent onward to another sponsor, Elprint Norge [44], which had agreed to produce the PCBs for us. The problem was that the factory workers in China was on a holiday which started just before the files were finished. The PCBs would therefore not arrive soon enough for the component soldering to be done before Easter.

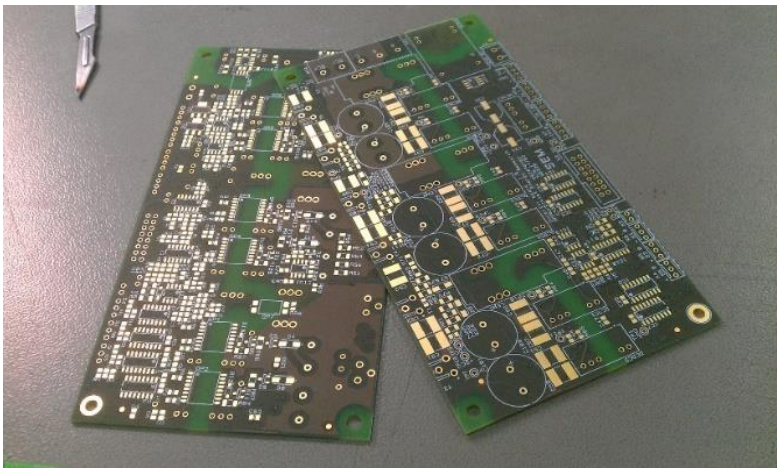

Figure 4.3.4.1: Finished PCBs from WE direct

Because of the delay two PCBs were quickly ordered form another firm, WE direct: [45]. Figure 4.3.4.1 illustrates the finished PCBs as delivered from WE direct. As soon they arrived they were taken straight to Noca [38] for soldering, see part 4.3.5, in order to finish the circuit boards before Easter.

The rest of the circuit boards from Elprint Norge arrived just before Easter and the components was soldered on them just after Easter.

4.3.5 Soldering

The job done by Noca was done through a sponsor agreement. As the main job of soldering the components to the boards was done by Noca the task became mostly logistics work. All of the components was ordered in time and delivered to Noca before the PCBs arrived. After that the job was to help out mapping out where each of the components where to be placed before they were soldered on to the circuit board one by one. Figures 4.3.5.1-2 illustrates this process.

Figure 4.3.5.1: Component position logistics work

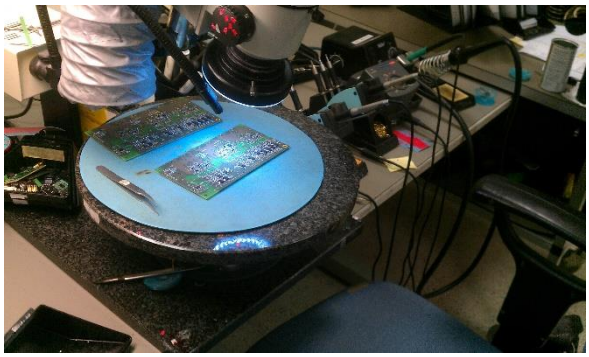

Figure 4.3.5.2: Components being soldered on to circuit board at Noca workshop

After a couple of days of hard work all of the components, except the PTC thermistor and MOSFETs, was finally in place. Figures 4.3.5.3-4 illustrates the finished result.

Figure 4.3.5.3: Inverter circuit board with components mounted, top view

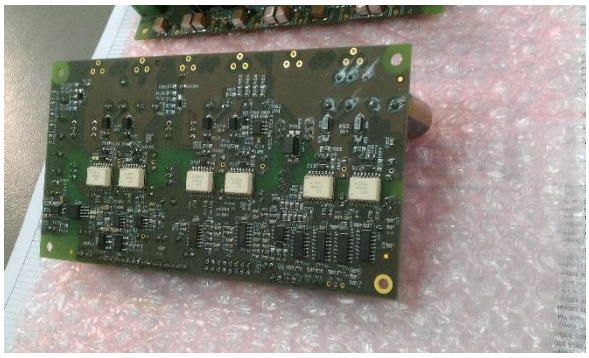

Figure 4.3.5.4: Inverter circuit board with components mounted, bottom view

The PTC thermistor and the MOSTFETs were not to be soldered to the board as this would be done later. It was done this way because those parts would also be mounted to the heat sink. See part 4.3.6.

4.3.6 Heat sink and the finished inverter circuit board

When the circuit board component soldering process was done the last step was to mount it to a heat sink along with the PTC thermistor and MOSFETs. A suitable heat sink was found. Three heat sink pieces was cut from the main piece. One for each vehicle along with one reserve. Figure 4.3.6.1 illustrates the process of drilling out the holes needed for each part that would be mounted on it. The way this should look is described in the inverter board documentation: [37]. Figure 4.3.6.2 illustrates the process of soldering on the MOSFETs. Note that an electrically insulating, but heat conducting, material was placed between the MOSFETs and the heat sink so that they do not short-circuit.

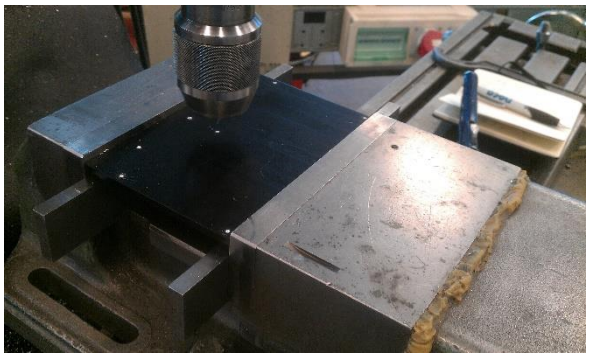

Figure 4.3.6.1: Drilling holes in heat sink suitable for the inverter circuit board

Figure 4.3.6.2: MOSFET soldering process for the inverter circuit board

A serial number was written in the corner of each inverter circuit board in order to separate them. Figure 4.3.6.3 illustrates the production process of board number 1, 2 and 3 respectively (from left to right). What was done, considering the different MOSFET types, was to solder MOSFET number 3 in list 4.3.2.2.2 to circuit board number 1 and 3, as STMicroelectronics is known for delivering very reliable products. MOSFET number 2 on list 4.3.2.2.2 was soldered to circuit board number 2, hoping that there would be time for some testing.

Figure 4.3.6.3: All of the three different inverter circuit boards under production

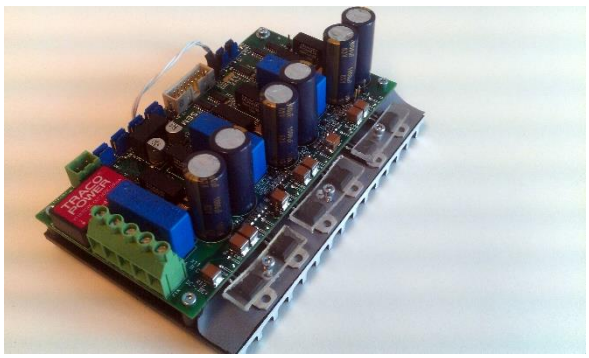

Figure 4.3.6.4: Final inverter circuit board mounted to heat sink

Figure 4.3.6.4 is the final inverter circuit board on display. Three pieces of thick plastic were used to press the MOSFETs down on the heat sink as illustrated. The PTC thermistor was

mounted to the heat sink underneath the circuit board by a twisted wire soldered to connection X4 on the circuit board.

Finally the testing could commence. See part 8.9. Two design faults was discovered. Some resistances in the voltage measurement circuit had had to be replaced by other values and two LED signals had to be swapped. Everything else was functioning properly.

4.4 Inverter inputs, outputs and other necessary hardware connections

Figure 4.4.1 illustrates the connection row on the inverter circuit board. Only the DC input (+ and -) and the three-phase output (A, B and C) is not visible. The relevant connections will now be described from left to right in list 4.4.1.

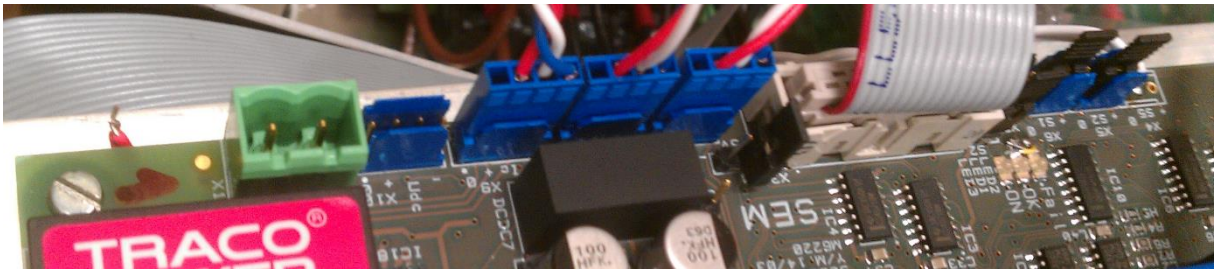

Figure 4.4.1: Inverter circuit board connections illustration

For more information about how some of the different outputs and inputs are connected to the FPGA see part 5.4.

X1	24V driver supply	Connection for using an auxiliary 24V power supply. This connection is not used in the final system.
Udc	DC voltage measurement	The DC voltage measurement output is connected to the FPGA. Dubox connector with four twisted wires must be used instead of three wires like the current measurements.
Ic, Ib and Ia	Phase C, B and A current measurement	The phase current measurement outputs are connected to the FPGA. Dubox connector with three twisted wires.
S1	Common driver voltage supply	Sets whether or not the inverter board and the FPGA has common 5V driver supply. It is best to have these separated. Thus no jumper is connected here in the final system.
X3	Driver interface	The main signal cable between the inverter and the FPGA. Provides the pulses and status, among other signals.
S2	Auto reset	Placing a jumper on this connection enables the auto reset function. This is used in the final system as it would automatically reset the system if something goes wrong during the race. Which is better than stopping completely.
X2	Manual reset	For using a push button to manually reset the circuit. Not used.
X6 and X5	Blocking	If pin 1 and 2 is not connected on both X5 and X6 then a blocking signal trips the circuit. One out of two solutions may be used: Either use a jumper to connect them or use them for implementing trip conditions externally. A jumper was used on X5 in the final system, but X6 was used for blocking the inverter if the battery relay was open.

List 4.4.1: Inverter circuit board connection descriptions

For more information about the different connections see the documentation: [37].

Chapter 5: Controller theory and operation

In this chapter the controller theory and operation is presented. The controller circuit used in this thesis is the field-programmable gate array (FPGA). Information like the motor controller algorithm, different FPGA hardware options, inputs, outputs and tuning is described here.

5.1: Controller theory

Some of the theory presented here is based on knowledge gained from the book "Advanced Electric Drives" by Ned Mohan: [46].

Figure 5.1.1 represents a PMSM, or brushless DC machine, vector control structure. It is based on the dq-transformation, also known as Park's transformation, which was described in part 3.1.2.

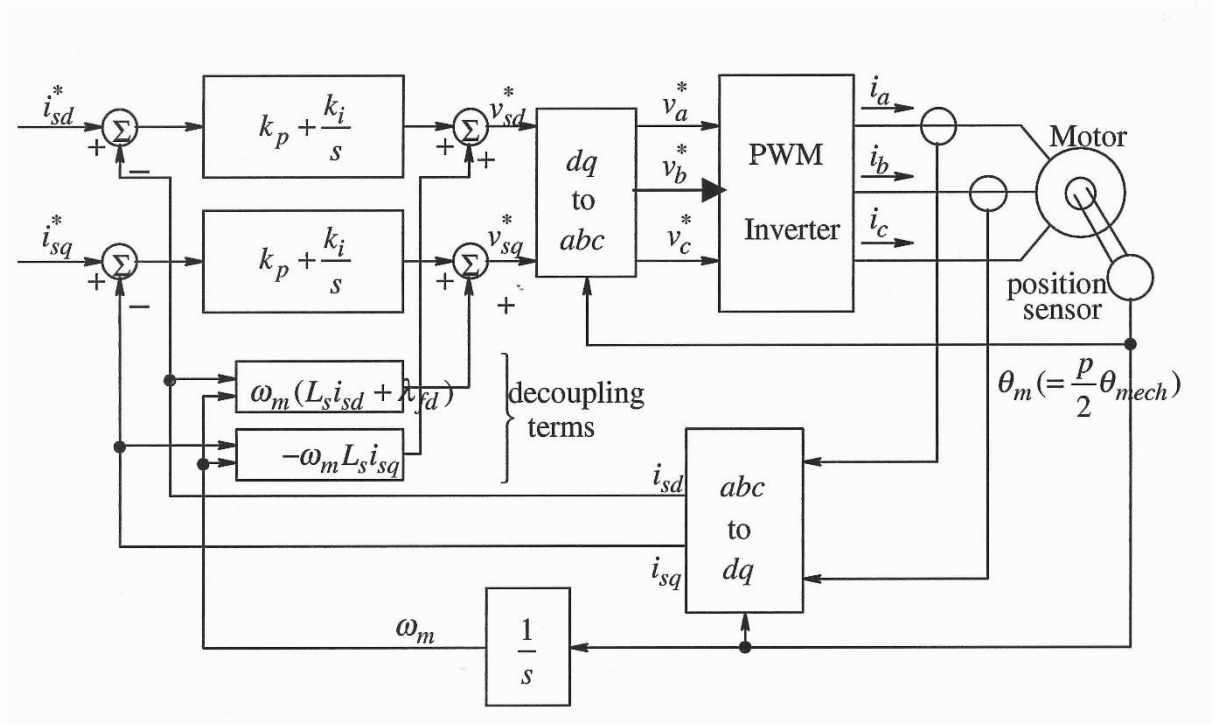

Figure 5.1.1: PMSM vector control structure [46]

The q-axis current (i^*_{sq}) represents the part of the total current which results in motor torque. The d-axis current (i^*_{sd}) is the part which represents flux weakening. Thus the part of the total current that induces a flux which weakens the total magnetic flux in the air gap of the motor. Flux weakening can therefore be used to lower the induced voltage from the machine. See equation 3.1.1.6. Lowering the induced voltage is useful in several cases. For example, when the motor operates at a speed so high that the equivalent induced voltage is equal to the supply voltage then a possible way to accelerate further is to lower the induced voltage. The d-axis current reference value is usually set to zero in normal simulation scenarios as the d-axis current does not contribute to any torque. The q-axis current, on the other hand, is actively used to control the torque/speed of the motor.

In order to regulate the actual currents compared to their reference values PI regulators usually used. In figure 5.1.1 these PI regulators are represented by $k_p + k_i/s$. k_p is the proportional (P) part of the regulator. It is simply a constant multiplied with the difference between the measured current and the reference which equals the gain. Often when there is an external load on the system the proportional regulator is not enough as a constant error may occur. The integral (I) regulator solves this issue as the gain, even for a constant amount of error, increases with time. The constant parameters of both regulators (k_p and k_i) is tuned to the actual system in order to achieve a satisfying control behaviour.

Requested dq current gains are interpreted onwards as dq voltage gains (v^*_{sd} and v^*_{sq}) and then transformed back to abc voltage signals (v^*_a, v^*_b and v^*_c). These are voltage control signals given to the PWM algorithm, described in part 4.1, which translates it into needed voltage pulses provided to the PMSM.

An unfortunate mathematical issue is that the d- and q- axis voltages are partly coupled. The dq-transformation theory in part 3.1.2 assumed two magnetically independent axes, but this is not completely true. While trying to control one of them the other is also affected to some small degree. The decoupling terms in figure 5.1.1 removes the link between the d- and the q-axis by removing the coupling component from both the d- and q- voltage segment. For further descriptions of the decoupling terms see [46].

The position sensor illustrated in figure 5.1.1 has the same function as the encoder described in chapter 6. Exact rotor position is needed in order to achieve correct dq-current transformations which is a very crucial part of the control strategy used.

5.2: FPGA hardware and software solutions

5.2.1 Considered FPGA options and solution

Figure 5.2.1.1 illustrates the NI sbrio-9626, [47], by National Instruments [48]. It is the FPGA that was used for the driver interface system. The thesis involving this part of the system is found at: [49]. This FPGA allows implementing Labview [5] software which makes it much easier to implement control software. Two sets of these was ordered as the original plan was to use this FPGA both for the driver interface and the motor controller system. Figure 5.2.1.2 illustrates the FPGA developed by SINTEF Energi [11] for inverter control purposes.

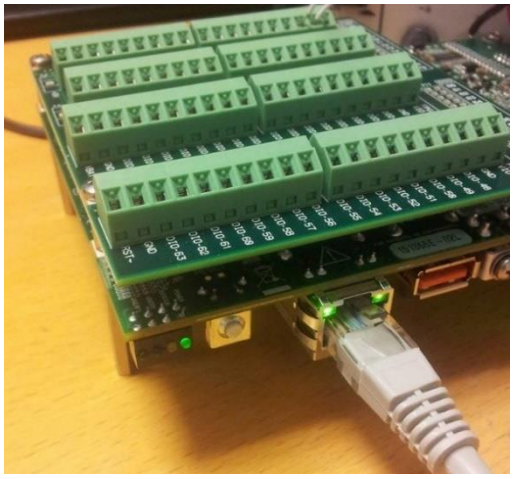

Figure 5.2.1.1: NI sbrio-9626, National Instruments [49]

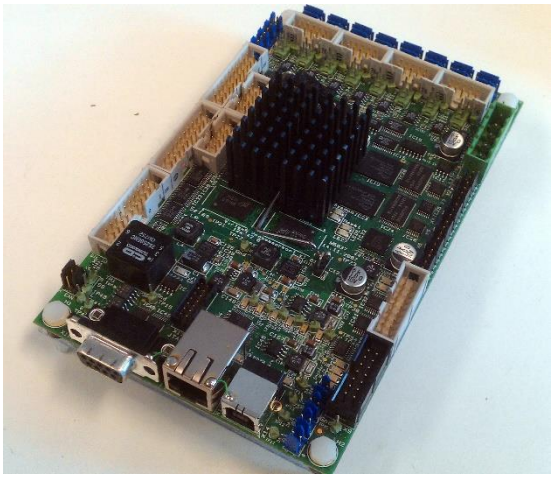

Figure 5.2.1.2: VIRTEX 5, XILINX, FPGA circuit board developed by SINTEF Energi

The National Instruments (NI) forums offers a lot of help when it comes to programming a motor controller on their FPGA modules, but in order to make it compatible to the inverter circuit board a lot for adapter circuits would have to be developed. The FPGA circuit board developed by SINTEF Energi was already compatible and the needed software was already developed.

It was decided early to use the SINTEF FPGA circuit board as there would not be enough time to develop the adapter circuit and needed software for the NI FPGA before the competition. Despite the fact that the NI FPGA could potentially introduce a lower standby power consumption and/or operation load than the SINTEF FPGA. Keep in mind that the controller was only 1 out of 4 critical parts in the system developed for this thesis. See figure 2.6.1. If the controller had been the only concern in this thesis then the time available would probably have been sufficient to use the NI FPGA as well and test which FPGA that was best suited for the efficient control purpose. It should also be mentioned that a new and upgraded version of the SINTEF FPGA is under development which may be available for later SEM competitions. Exactly when this upgraded FPGA will be available is still uncertain.

5.2.2 The SINTEF inverter controller

Only a few parts of the inverter controller logic will be described here as most of it is either too specific or not relevant enough for the rest of the work presented in this thesis. The SINTEF FPGA inverter controller project memo is found here: [50]. Please see the project memo for further information on subjects which are not presented here.

Some of the controller functions of the SINTEF FPGA inverter controller is actually implemented in the hardware rather than the software. The "FPGA IP MODULE MAP" found on page 35 of the project memo illustrates the different hardware modules. Something worth noticing is that the Park's transformation blocks, dq current regulator, current filters, voltage filters and PWM modulator is there. The modules that are implemented in hardware modules operates at 40 MHz, rather than 10 kHz [50] which is the software operating speed. In short this means that all of these functions becomes very precise.

Figure 5.2.2.1 illustrates the model block diagram of the motordrive system that was used for controlling the inverter, thus also the two different electrical motors, used for SEM 2014:

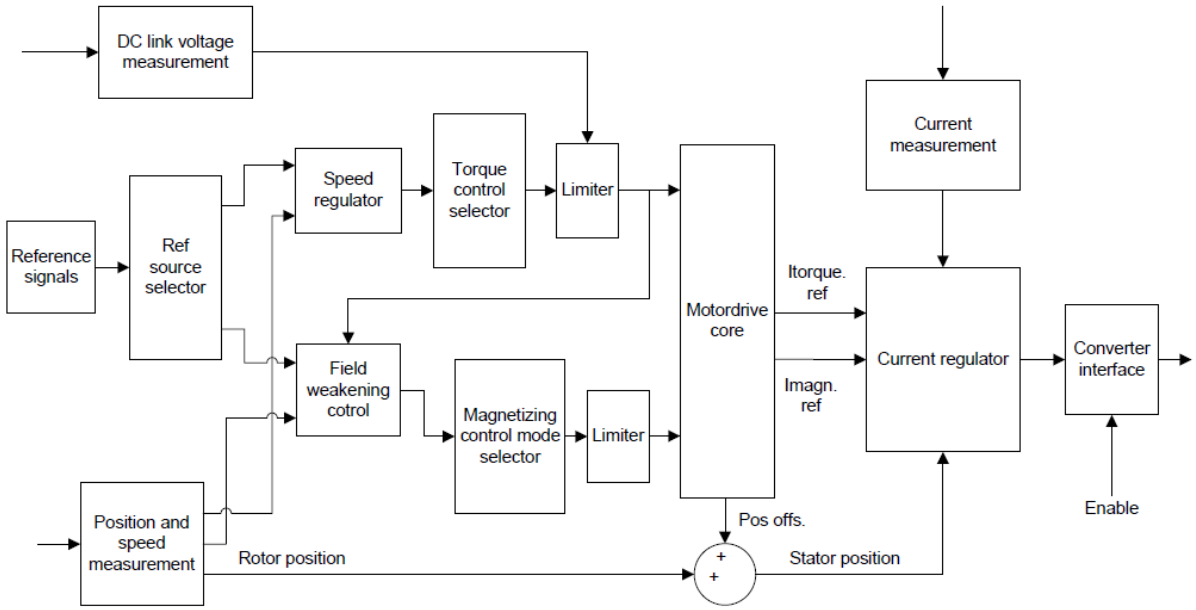

Figure 5.2.2.1: The motordrive system block diagram as illustrated in the project memo [50]

The motordrive system works for both induction and synchronous machines by adjusting the parameters provided to the motordrive core. More on the parameter subject is found in part 5.5. The rotor position is given by the encoder. See chapter 6. The active control function is set to torque control in this thesis. Thus the speed regulator is not relevant. In order to compare this motordrive system with the one presented in part 5.1, the parts of most interest hides inside the current regulator block. Figure 5.2.2.2 is the dq current regulator block diagram as illustrated in on page 31 of the project memo:

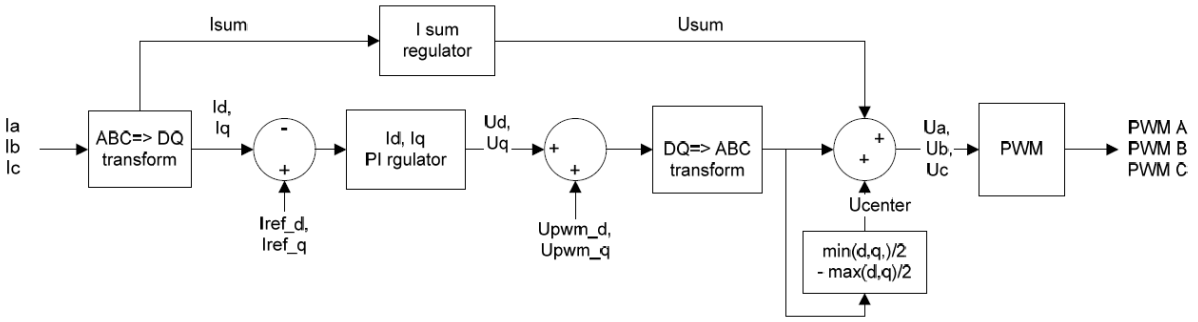

Figure 5.2.2.2: The dq PI current regulator block diagram as illustrated in the project memo [50]

PWM voltage d- and q- axis voltages (U_{pwm_d} and U_{pwm_q}) are not used for motor controller purposes, so these inputs are just set equal to zero. There are three important differences between this diagram and the one displayed in figure 5.1.1:

The first difference is that the current regulator implemented in the SINTEF FPGA does not have the decoupling terms. As the current regulator operates on 40 MHz, it is so fast that ignoring the coupling effect has a negligible impact. Adding the decoupling terms would need several motor parameters (like stator inductance, rotor produced flux and stator resistance) which would have had to be added into the motor parameterization process.

The second difference is that the regulator illustrated in figure 5.1.1 does not include a feed forward regulator which centres the voltage control signal. This function is implemented in the SINTEF FPGA current regulator. What it does making sure that the maximum and the minimum voltage control signal has the same distance to the overmodulation limit by adding a centring value (U_{center}) based on the maximum and minimum control voltage signal. This way overmodulation is avoided as much as possible. Overmodulation happens when the voltage control signal becomes much greater than the triangle signal so that the voltage pulse out the inverter becomes constant.

The last difference is that the SINTEF current regulator includes a forward feed proportional regulator that regulates the sum of the current signals (I_{sum}) towards zero. This feature is not included in figure 5.1.1.

5.3 FPGA power supply solution

The SINTEF FPGA described in part 5.2.2 requires a power supply with several different voltage levels: 5V, 15V and -15V. It was not only the voltage levels that had to match. The power supply also had to deliver the needed current with tolerable efficiency. As the signal circuit is supposed to be isolated from the power circuit the power supply had to provide this feature as well.

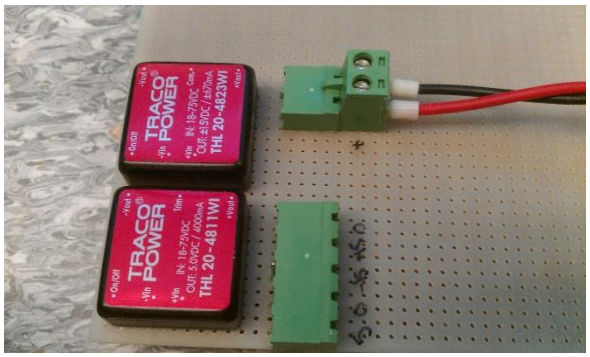

Figure 5.3.1: FPGA power supply, top

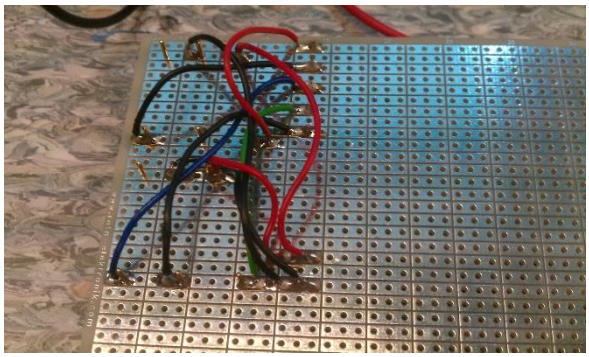

Figure 5.3.2: FPGA power supply, bottom

Based on these needed power supply features it was decided to use DC/DC converters delivered by Traco Power [51]. In their internet catalogues two suitable DC/DC converters was found in the "General Purpose 2 to 30W" category. Figures 5.3.1-2 illustrates the power supply circuit board and in list 5.3.1 the DC/DC converter data is found.

Order code	**Input voltage range**	**Output voltage**	**Output current max.**	**Efficiency typ.**
THL 20-4811WI	18 – 75 VDC (48 VDC nominal)	5.0 VDC	4000 mA	90 %
THL 20-4823WI	18 – 75 VDC (48 VDC nominal)	±15 VDC	±670 mA	89 %

List 5.3.1: Data for the Traco Power DC/DC converters used for the FPGA power supply circuit board [52]

The large input voltage range was important as the DC bus voltage varies a lot with how the motor is operated. Output current max., multiplied with their respective output voltages, equals 20W for the 5V supply and 10.05W for the +/-15V supply, which should be more than enough supply power for the FPGA. Efficiencies of 90 % and 89 % respectively was assumed to be good enough as the main propulsion current would not go through these converters. Only the controller supply current. Higher efficiencies could have been achieved if converters with weaker insulation and isolation capabilities were chosen.

It was discovered during system testing that these DC/DC converters became quite warm if the system was on standby for a while. See part 8.10.3. At this point it was too late to consider new power supply options. This aspect should therefore be considered for further work.

5.4 FPGA inputs, outputs and other necessary hardware connections

This part of the thesis describes the different relevant connections considering the FPGA. There are two connections not illustrated in figures here: The driver interface connection with the inverter and the encoder connection. However, both of these are illustrated in the final system, figure 9.1.2, and the encoder is connection further described in part 6.4.

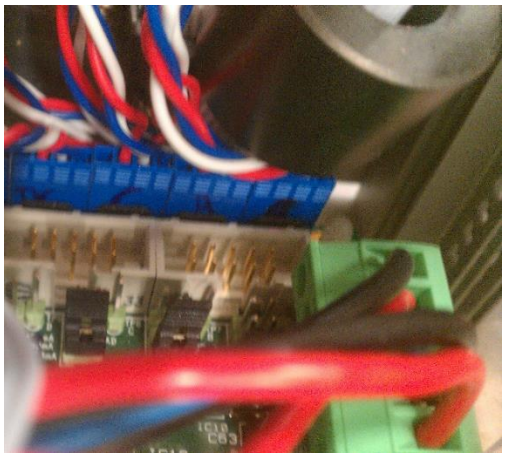

Figure 5.4.1: FPGA power supply, DC voltage measurement and three-phase current measurement connection illustration

Figure 5.4.1 illustrates the different measurement connections and the power supply connection. Measurement connection placement from left to right: DC voltage, phase C current, phase B current and phase A current measurement. Power supply connection placement from lower to upper position: 5V, 0V, -15V, 15V and 0V.

See list 4.4.1 for the inverter measurement connection descriptions and part 5.3 for the power supply description.

Now the needed jumper connections will be described. Figure 5.4.2 illustrates the jumper needed to replace the on/off switch originally used with this FPGA. Without the jumper or the switch the system will not be able to operate.

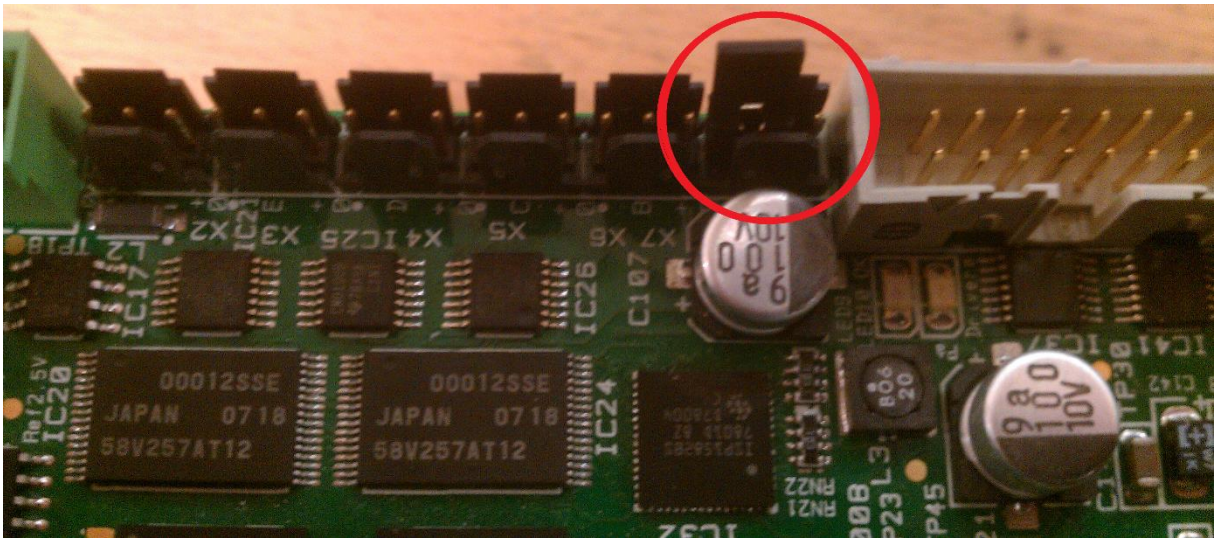

Figure 5.4.2: FPGA jumper connection (red circle, X7) in order to replace on/off button

Three other very important jumper placements are related to the current measurements. They are supposed to be placed on the pin pairs which equals 25 mA because that is the nominal current of the LEM current measurement components. See part 4.3.2.2.

Unfortunately there is fault in the FPGA circuit board print. The pin pairs marked as 25 mA is actually 100 mA and the 100 mA is actually 25 mA. Thus the jumpers must be placed on the pin pairs marked as 100 mA as illustrated in figure 5.4.3.

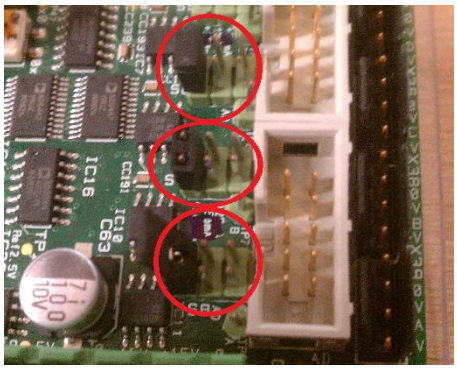

Figure 5.4.3: Current measurement FPGA jumper connections (red circles)

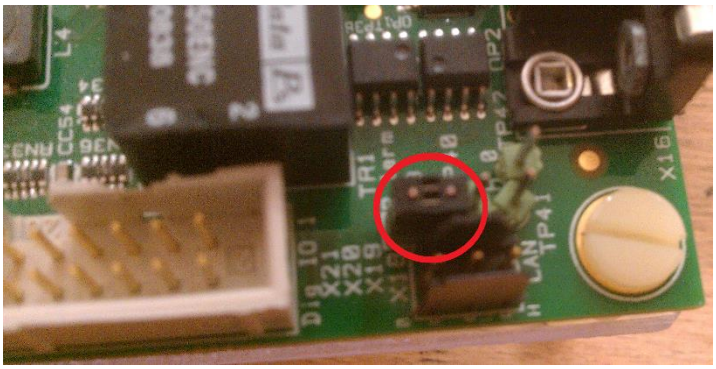

Figure 5.4.4: Jumper terminating the CAN bus (red circle) on the FPGA

Figure 5.4.4 illustrates one last jumper connection. This is for terminating the CAN bus in order to minimize signal reflection. The CAN bus connection, marked with CAN in the print, is also illustrated in the same figure just under the terminating jumper. This will not be described in further as it is not that relevant for this thesis. See [1] for more information on the CAN bus system.

5.5 Controller operation and tuning

Only the relevant parts considering tuning and operating the motordrive system will be described here. The motordrive controller has a lot of functions and parameters, but not all of them are relevant enough for the work presented in this thesis.

The first thing to be described is how to activate and deactivate the screen used for parameterizing the motordrive controller settings. A bug in the software did not allow the screen to be deactivated at the start of the thesis work, but it has now been fixed. In order to access the screen enabling parameter the FPGA software has to be accessed by computer. The software used is called ActiveDSP. Ask the power electronics service lab at NTNU Gløshaugen for access to this program. Both NTNU and SINTEF have a valid licence. The initial setup is description is found in appendix C.

When the FPGA answers the ping commands from the computer the screen enable parameter may be changed. Go to the ungrouped variable list in the upper left corner and find the parameter called “menusystem_enable” in the drop down list and drag it over to the “Variable [Parametre]” list. Setting the “menusystem_enable” parameter to 0 and pressing enter deactivates the screen and setting it to 1 activates it. The FPGA must be turned off then on again in order for the parameter change to have any effect.

With the screen activated in the software and connected to the FPGA circuit board the different operating conditions, settings and parameters may be accessed. Figure 5.5.1 illustrates the main screen which first appears when you start up the system.

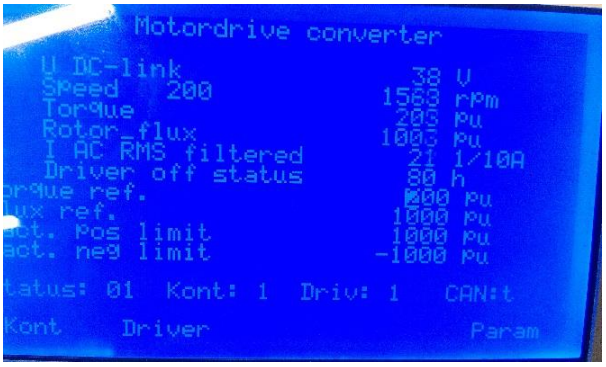

Figure 5.5.1: Motordrive converter main screen illustration

The main screen illustrates several different things. What is displayed on this page may be configured in the parameter list. There are three different things the user can select on this screen: “Kont”, “Driver and “Param”. In order to activate the “Driver” state the “Kont” must be activated first. When in “Driver” state and no fault conditions or limitations has been triggered the status display shows “Status: 01, Kont: 1 and Driv: 1. The CAN bus status is also displayed on the same row. For more on all of the different status messages see the project memo: [50].

When in the “Driver” state the torque ref. and the flux ref. may be set. The torque ref. is what accelerates the motor as long as the system is set up correctly. Reducing the flux ref. increases flux weakening. See part 5.1.

If the “Driver” and “Kont” status is deactivated the “Param” feature may be selected. Selecting this opens up the motordrive parameter list. There is a total of 15 different pages with a lot of different parameter settings. List 5.5.1 describes the most important ones. The full parameter list used for SEM 2014, for the urban and the prototype vehicle, is found in appendix D.1-2.

Contol signal source	Set to “Menu” for the tuning and testing purposes of this thesis. Finally set to CAN bus control in order to allow the driver interface FPGA to control the system.
Rotor time constant	Set to 0 ms. No time rotor time constant for PMSMs as the permanent magnets are the only rotor flux source. [50] This function is for motors using squirrel cage windings.
Reluctance	(=1000*(1-Xq/Xd)) [50] = 0 pu. Surface mounted magnets in the motors means that Xq=Xd. See part 3.2.
Remanence	The remanent magnetism is set to 1000 pu. Rated flux. [50]
Pole number	Pole numbers for the urban and prototype vehicles is set to 24 and 14 respectively. See parts 3.3.1.1 and 3.4.1.2.
Position sensor direction	If the motor is spinning the wrong way, but the motordrive still reads a positive speed, then change this parameter to the opposite direction.
Phase sequence	If the motor won’t start spinning, despite the fact that the other parameters have been set correctly, then it is possible that the phase sequence is wrong. In such case try changing this parameter.
I meas. AD full scale	= transfer ratio*nominal current full scale (2*I_{nom}) [1/10 A] = 1000*2*25mA = 50A = 500 [1/10 A], see parts 4.3.2.2 and 8.4.3.
AD offset I A, B and C	Has to be calibrated for every inverter circuit board. This done by choosing the “AD I phase” A, B and C to be displayed. Observe how many bit they are away from 0 bit with the system off and adjust the offsets accordingly. See part 8.7 for more about how the current calibration was done in practice.
Switching frequency	The switching frequency can influence the efficiency of the system. See part 8.5. Higher frequency means greater switching losses, but also smoother AC phase currents.
Pos. sensor type	Sets the encoder type. The type encoders studied in this thesis are optical encoders with A, B and index pulse (I). Thus “Enc+ref”. See part 6.1.
Pulses per.rev	Sets the CPR (cycles per revolution), also known as pulses per revolution, of the encoder. This is set to 2048 pulses for the ROD 420 encoder and 2500 pulses for the US Digital encoders. See part 6.2.
Stator pos. offs.	This is the parameter that required the most attention during this thesis work. It is the parameter that relates the electrical and the mechanical rotor position. The parameter spectre is from 0 to 3600 [0.1 deg]. If it is not tuned correctly then currents are not used properly to create torque. Thus lowering system efficiency. More about this parameter in part 6.5.
Overspeed trip level	Set to 390 rpm for the urban and 4000 rpm for the prototype

	vehicle. The prototype vehicle has a 1:10 gear, so it's about 40 km/h for both vehicles, which is far above the desired vehicle speed. See part 2.2.1.
Max speed limiter start and end	When max speed limiter triggers it limits the amount of power the driver can put into the motor, thus limiting the speed. See part 9.3.
Reversal inh. lim start	Limits the breaking torque when the speed is lowered. Set it to -1 if you want the motor to be able to go backwards without having to activate the reverse function. Was set to 10 rpm for SEM 2014.
U DC link AD full scale	Used to calibrate the DC voltage measurement. Measure the DC voltage and adjust the parameter so that the correct voltage is shown.
U DC high limit start, limit end and disable	When breaking torque, also known as regenerative breaking as it charges the battery, is used the DC voltages rises. These functions are used to limit the DC voltage by limiting the amount of regenerative breaking applied.
CAN bus enable	Enables the CAN bus communication.
CAN message valid time	Control messages has to be spammed at a certain frequency in order to operate the system. This function prevents the system from operating while the CAN bus unit is not.

List 5.5.1: Descriptions of the important parameters in the motordrive controller software

The temperature parameter list was not mentioned in list 5.5.1 as no temperature measurement devices was connected to the FPGA. The display parameters allows the user to change what is displayed in the main screen which was shown in figure 5.5.1.

Chapter 6 Encoder solutions

The encoder is the component that measures the motor rotor position compared to the stator in the form of an electrical/mechanical degree. There are many ways to measure this position. Only the method used for this thesis will be presented in this chapter.

6.1 Optical encoder theory

The encoders used for this thesis are of the optical type. It means that the rotor position is measured in a way that uses the behaviour of light. The output level used is TTL (transistor-transistor logic) compatible which, among other specifications, means that the encoders operate on a 5V supply. The optical encoders presented in this chapter operates identically or similarly to the method that is presented in figure 6.1.1:

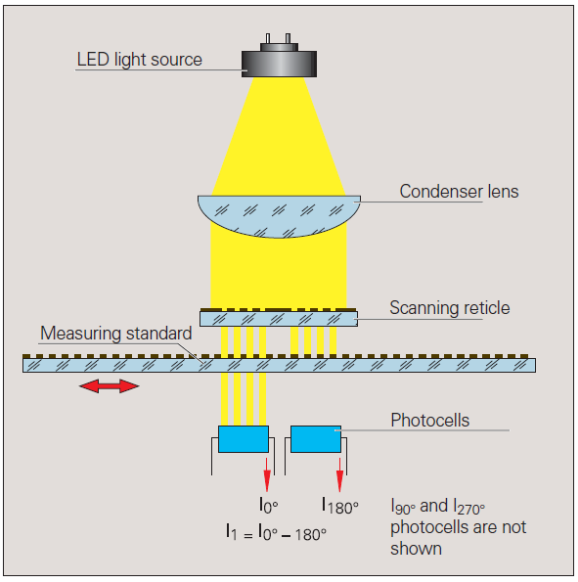

Figure 6.1.1: Optical encoder scanning illustration [53]

A led light source emits a light beam that passes through a lens that concentrates the beam which passes through a scanning logic were the light is converted into electrical signals by photocells. The component called "Measuring standard" in figure 6.1.1 is the only moving part. This is a transparent disc with stripes on it. The light beam does not go through these stripes. This way pulse signals are created. The amount of stripes per revolution defines the resolution of the signals. In some literature this resolution is referred to as cycles per revolution (CPR). As it defines the number of electrical cycles per revolution. The encoders used for controlling the PMSMs has a total of three channels as illustrated in figure 6.1.2.

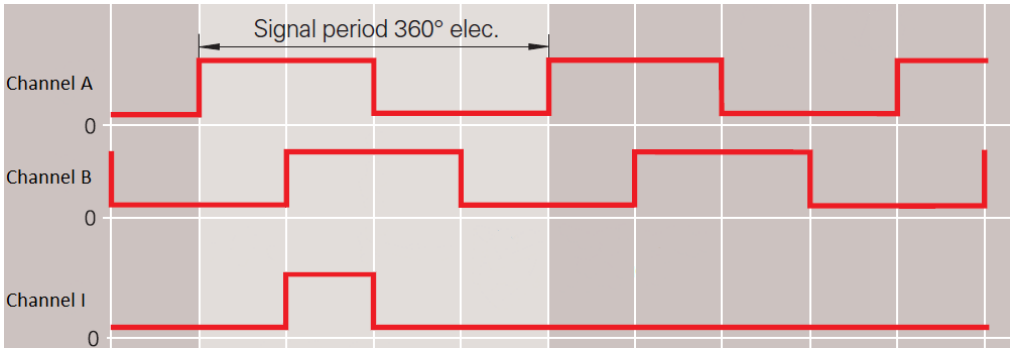

Figure 6.1.2: A, B and index channel optical encoder pulse illustration [53] *(edited)*

The most common channels are the A and B channel. By registering these pulses controller algorithms are able to identify changes in rotor position. They are displaced 90 electrical

degrees apart. This displacements allows the motor controller to identify the direction of the rotation depending on which pulse that is activated first. The third channel is the index (I) channel. It registers light on a separate area of the disc with only one stripe. Thus the index channel only provides one pulse per revolution. This is used to register the exact disc position on the rotor.

6.2 Encoder options

6.2.1 HEIDENHAIN

The HEIDENHAIN ROD 420, [53], is illustrated in figure 6.2.1.1. It was used on the motor rig presented in part 8.4.2. It was also involved some other tests which revealed an issue with the US Digital encoders which will presented in part 6.2.2.

Figure 6.2.1.1: HEIDENHAIN ROD 420 [54]

ROD 420 is a commonly used and very reliable encoder. The resolution of the component is 2048 pulses. This has to be implemented in the controller parameter list in order to use the encoder. See list 5.5.1. It was not used for the final system in this thesis though because it is designed for bigger motors: It requires too much space, is too heavy and has rotor friction and inertia which is greater than what is acceptable for the small motor system developed. Other HEIDENHAIN products was investigated, but all of the required too much space for the purpose of this thesis.

ROD 420 provides all of the three needed channels as illustrated in figure 6.1.2, but it also provides their inverted signals in order to reduce the effect of noise. Thus the wires of the ROD 420 are the incremental signal outputs: A, -A, B, -B, I and –I. Including the power supply input: 5V and 0V.

6.2.2 US Digital

US Digital has a lot of different encoder solutions for smaller motors available on their websites: [55]. The ones that finally were considered was encoder solutions based on the EM1 encoder illustrated in figure 6.2.2.1. It represents the parts that provides the same solution as the stationary parts of figure 6.1.1. The encoder type ordered and tested was the EM1-2-2500-I. “2-2500” means that it is designed for 2” discs with 2500 CPR. The final code, “I”, means that the index channel is included. The pins of the encoder, from left to right, is the B, 5V, A, I and 0V connection. The disc is illustrated in figure 6.2.2.2. It is a 2” outer diameter and 1” inner diameter plastic disc designed to include the index channel and compatible for EM1 encoders. Thus the final order code was “DISK-2-2500-1000-IE”. This is the same solution as the 2013 team used: [12]. The third picture, figure 6.2.2.3, illustrates the S1 encoder module which was ordered a short time after the first order due to some issues with the first solution, which soon will be described.

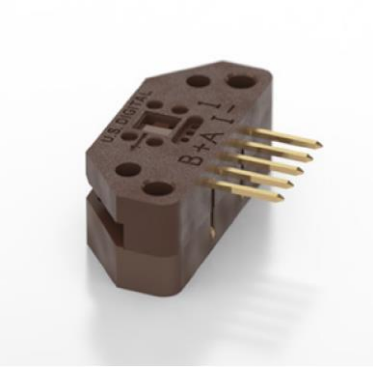

Figure 6.2.2.1: US Digital EM1 optical encoder [55]

Figure 6.2.2.2: US Digital DISC-2 plastic encoder disc [55]

Figure 6.2.2.3: US Digital S1 encoder module [55]

The S1 encoder module uses the same parts as the first solution, only with a smaller disc with the same CPR. Encoder and disc is placed within a hard plastic casing which protects them from the outside conditions. It is connected mechanically to the rotor with its own rotor equipped with ball bearing which allows a max speed of 10 000 rpm [55]. Final order code: S1-2500-250-IE-B-D.

A cable driver, figure 6.2.2.4, and suitable cable, figure 6.2.2.5, was needed as the output of the encoder did not include the inverted signals for noise reduction like the outputs that the ROD 420 has. See part 6.2.1. Final order codes: PC5-H10 and CA-C10L-SH-NC-6 respectively.

Figure 6.2.2.4: US Digital PC5 line driver [55]

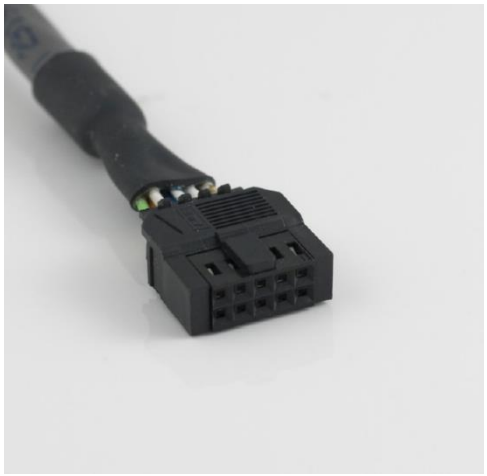

Figure 6.2.2.5: US Digital CA-C10L-SH-NC twisted pair 24 AWG cable [55]

The first issue encountered was that the first solution (using EM1 with DISC-2) was very unreliable. Placing the two parts correctly on the rotating part and perfectly relatively to each other is hard. Misplacing the encoder on the disc leads to very abnormal control behaviours as one, or more, channel pulses becomes wrong in some way. Another problem was that the disc easily got dirty or bent due to external conditions which lead to the same abnormal behaviours. The different tests are described in parts 8.10.1-2. This is why the S1 encoder module was ordered and also used in the final system for both vehicles.

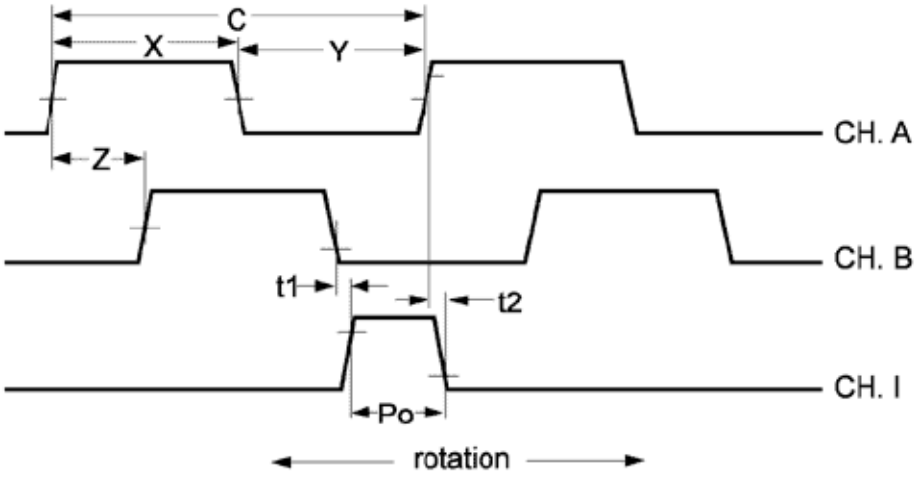

Figure 6.2.2.6: 3 channel US Digital EM1 encoder pulse output illustration [55]

Figure 6.2.2.6 illustrates the pulse outputs for the different channels of the US Digital encoder solutions. Compared with the pulse sequences given in figure 6.1.2 one important difference is found. The US Digital encoders index pulse triggers 180 electrical degrees later than the index pulse provided by HEIDENHAIN encoders. Meaning in practice that the A and B signal polarity is opposite. The result of this design difference was that the index pulse of the US Digital encoders was not registered by the motor controller encoder logic. If the index pulse is not registered the motordrive controller uses a random rotor position. A lacking index pulse can be identified by turning the system off then on again. If the motor behaviour changes each time then the index pulse is probably absent. When the problem finally was identified it was fixed by switching the A and B signals inputs with their inverted signals: -A and –B. See part 8.10.2 for more information on the testing procedures leading up to this critical fix. This encoder measurement logic weakness has been fixed in the updated motordrive controller software.

6.3 Encoder mounts

6.3.1 Urban concept encoder mount

Relevant urban vehicle encoder mount tests, results and solutions are described to detail in parts 8.10.2 and 8.11, but some of the conclusions are also presented here.

Mounting an encoder to the urban concept vehicle axial flux motor is difficult for mainly two reasons. The motor is also the wheel, which is connected to a damper. This means that the motor position relatively to the rest of the vehicle varies vertically with the weight load on the vehicle as well as bumps on the road. The second reason is that the middle axle is stationary which means that is hard to find a suitable rotating axle on which to connect the rotating part of the encoder.

Figure 6.3.1.1: EM1 on DISC-2 urban vehicle encoder mount

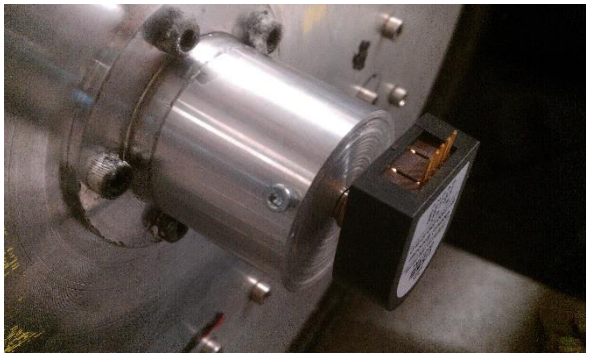

Figure 6.3.1.2: S1 urban vehicle encoder mount without vertical fork

Figure 6.3.1.1 illustrates the encoder mount solution which was created by the 2013 team. See figure 3.2.3 and [12]. The disc is glued to the rotating surface around the stationary axle and the EM1 encoder is attached to an aluminium part that is attached to the stationary axle designed so that the disc is partly in the encoder gap. This solution is not that affected by the vertical movement issue, but it is however very vulnerable to external forces and conditions. After the old disc was switched with a new one it only took 2 days for this part to be defect again. Another issue was that the encoder position had to be very carefully adjusted in order to provide proper position readings. If the encoder changed position by a very small amount somehow then the motor started to act very strange straight away.

Initially the S1 encoder unit was ordered for the prototype vehicle system only, but as the initial urban concept vehicle encoder solution proved to be flawed a S1 solution for the urban vehicle was developed as well. The solution developed is shown in figure 6.3.1.2, just without the vertical fork. This part of the solution is visible in figures 8.11.1 and 9.3.1. The vertical fork is what ensures that the stationary part of the encoder does not rotate to either side while it is free to move vertically. The rotating part of the solution is a cylinder that is glued to the rotating part around the axle. The encoder rotor is inserted into a suitable hole on the outer side of the cylinder and a radial screw is used to lock the encoder rotor to the cylinder. The mechanical part of the team helped by doing the creation process of the cylinder. The first design didn't take into account that the aluminium EM1 mount had to be replaced by a nut which tightens the stationary axle. This caused the stator to slip a lot which leads to a constantly changing stator position. This was fixed in the final design by creating a longer cylinder and tightening the stator properly with a nut before gluing it on again, but stator slip may still have been the cause of some later fault events. See parts 8.10.2 and 9.5.

6.3.2 Prototype vehicle encoder mount

Some early testing with 3D printed encoder mounts was done to find out if the EM1 with DISC-2 solution could be used for the EC 60 flat or the AXI motor. See part 8.10.1. Results showed that such an encoder solution would be very unreliable and was therefore not investigated further and the S1 encoder modules was ordered.

As the EC 60 flat motor failed testing, parts 7.5 and 8.6, the AXI motor was the only option at this point. AXI motor encoder mounts developed are illustrated in figures 6.3.2.1-2. Designing encoder mounts for this type of motor proved to be a much easier task as the whole backside of the motor is rotating. Enabling easy access for an S1 encoder module rotor connection. The only motor design that would be easier to adapt to than this would be a secondary rotor on the backside of the motor, like the one illustrated in figure 8.4.2.7 on backside of the DC motor used for the test rig.

Both of the AXI motor encoder mounts developed were created by the NTNU power electronics workshop. On the backside of the AXI motor there are suitable screw holes available to mount a cylinder. In the middle of this cylinder there is a hole with a rubber ring along the edge with is designed for the diameter of the S1 rotor. When the S1 rotor is pressed into this cylinder there is enough friction between it and the rubber ring so that it follows the rotation of the cylinder. Note that as there was very limited space on the backside of the AXI motor inside the prototype vehicle, only 22mm, the S1 rotor length had to be reduced.

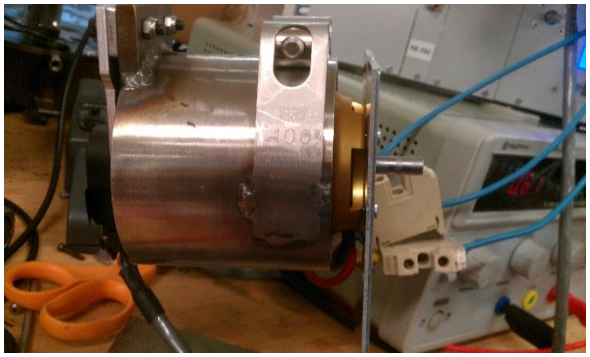

Figure 6.3.2.1: Initial S1 prototype vehicle encoder mount

Figure 6.3.2.2: Final S1 prototype vehicle encoder mount

The initial encoder mount design, figure 6.3.2.1, was very rigid, but also very heavy. A heavy encoder mount is unfortunate as the mechanical system design is as light as possible. It did not have good heat conducting properties either, as it surrounded the whole motor with a thick metal cylinder. During early testing the motor and encoder mount became warm fast as a result of this. See part 8.10.3. As soon as the first design proved to work well a new and lighter encoder mount was made based on the same design. The final solution is the one shown in figure 6.3.2.2.

6.4 FPGA compatible encoder input adapter

As the encoder FPGA connection is only 14 pole flat cable compatible encoder input adapters had to be made for both electrical systems. List 6.4.1 is an overview of the different channels, their wire colours, depending on encoder type, and to which flat cable pole they have to be connected to in order to be compatible with the FPGA. See [53] for more on the HEIDENHAIN wires and [55] for the US Digital wires.

Pole#	1	2	3	4	5	6	7	8	9	10	11	12
Description	B-	5V	I+	I-	A+	A-		B+		0V	0V	5V
Rod 420	Pink	Blue	Red	Black	Brown	Green		Gray			White	
EM1/S1 with cable driver	White, green stripe*	Orange, white stripe	Brown, white stripe	White, brown stripe	Blue, white stripe*	White, blue stripe*		Green, white stripe*			White, orange stripe	

*The A and B signal for the US Digital encoders should be inverted. See part 6.2.2.
Pole 13 and 14 are not used.

List 6.4.1: Pole number, description and encoder cable colours

Two different adapter solutions were developed. They are basically just two different ways of connecting the flat cable wires to the correct encoder cable wire. Figure 6.4.1 illustrates the first adapter made. As all of the wires can be easily connected and disconnected with the screw lock solution it was well suited for the initial testing as encoders had to be switched frequently. When the US Digital inverted A and B channel difference was discovered, part 6.2.2, it was also very easy to just switch the wires. However, this is adapter was not well suited for use in the vehicles as vibrations may create a fault in loose wire connections and because it requires a lot of space. Because of this a new compact and rigid adapter solution, figure 6.4.2, was developed right before leaving for SEM 2014.

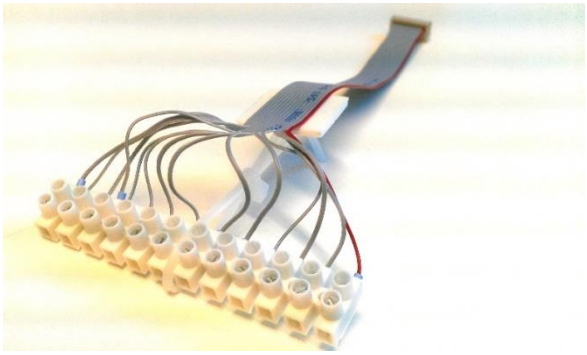

Figure 6.4.1: Test bench encoder adapter

Figure 6.4.2: Compact encoder adapter

The newest adapter solution was achieved by soldering together the correct cable pairs and insulating each one of them afterwards. The finishing touch was using insulation around all of the wire pairs, after insulating every pair, in order to wrap them together. The end result was a very compact encoder adapter which would withstand the expected vibrations. It is also much less likely to be affected by external elements like conducting materials which could lead to a short-circuit. As space was only an issue for the prototype vehicle, which also

was the vehicle that did not have any damping, the compact encoder adapter was made for the prototype vehicle electrical system first. The plan was to make one for the urban vehicle as well, but it was not done due to other pressing issues at the time. Switching encoder cables in the urban vehicle would be a bit more time consuming as it is fixed to the vehicle in order to go over and behind the wheel/motor and through a small hole into the trunk. This should be fixed before SEM 2015 if the same encoder system is to be used. It is still uncertain what caused the urban concept vehicle index pulse malfunction described in list 9.5.1. It could have been caused by a loose adapter wire connection.

6.5 Motordrive controller encoder tuning

In part 5.5 the motordrive parameterization was described, but not how to tune the "Stator pos. offs." parameter in detail. As this is such an important part of the thesis the process of finding the correct stator position offset is described here.

First operate the motor controller with the screen. Not the CAN bus. Remember to change the control source parameter to "Menu". The process involves changing the stator position offset parameter and then applying torque, observe and repeat until the correct stator position offset is found.

Now, in "Driver" state, apply torque. If the motor starts turning in negative direction when torque is applied then change the stator position offset by 180^{o}. If the motor does not start turning try applying flux weakening. If flux weakening does not make the motor start turning either, there might be something wrong with the phase sequence. If flux weakening accelerates the motor change the stator position offset by 90^{o}.

Once the motor is turning in the positive direction when torque is applied the fine tuning may commence. Run the motor at a low speed. If the motor is run fast the DC voltage may limit the speed and the motor will accelerate when flux weakening is applied. See part 5.1. Apply flux weakening and observe if this effect accelerates or slows down the motor. If the stator position offset parameter is wrong then one of these events happens because the currents are a bit off and applies a bit of torque (q-axis current) to the motor instead of just suppressing the permanent magnet flux (d-axis current). When this is done change the parameter a little and redo the previous step. Notice the effect and adjust the parameter accordingly. Once flux weakening does not apply torque in any direction the stator position offset parameter is set correctly.

Chapter 7: Electrical system model setup, simulation and results

This chapter describes the development of a simulation model of the electrical system and the simulation results achieved. The model is supposed to represent the prototype vehicle using the EC 60 flat motor. See parts 2.4 and 3.4.1.1.

7.1 Overall system model

A model of the electric drivetrain with motor was developed early. This was needed in order to get a sense of how the subsystems will work together and typical ratings needed for the design. Figure 7.1.1 illustrates the total model of the system. The software used is MATLAB [2] with the Simulink [3] and SimPowerSystems [4] expansion.

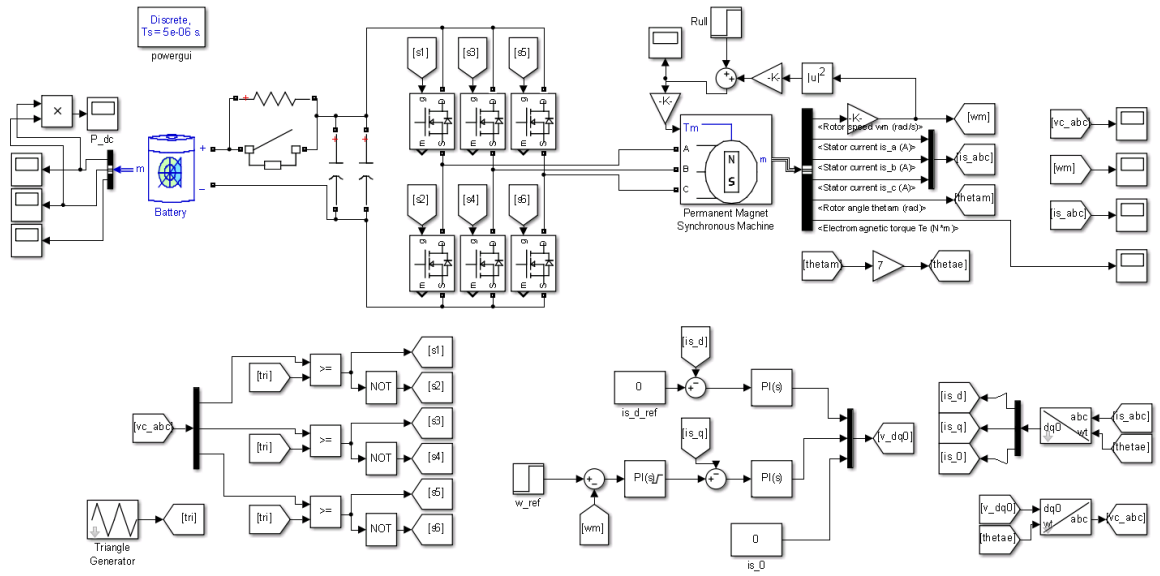

Figure 7.1.1: Overall electrical system model

As the model is rather complex the different subcomponents will be described separately in parts 7.2-4. The powergui block, located in the upper left corner of figure 7.1.1, is required for all SimPowerSystems [4] simulation. In this block it is possible to specify a large variety of different system settings. The only change made in this block is the “Simulation type” setting. See part 7.3.

The main concern early on was that the EC 60 flat motor, that had been ordered earlier, would be too weak to accelerate the vehicle. In order to get a better insight in that issue the electrical model represents the prototype vehicle with the EC 60 flat motor on a 1:10 gear.

7.2 PMSM and load model

7.2.1 PMSM model description and parameterization

For a better understanding of how the SimPowerSystems [4] PMSM block works mathematically see part 3.1.4.

As the motor is connected to a 1:10 gear the rotor speed of rotation is 10 times greater than the rotation speed of the vehicle wheel. This effect is modelled by multiplying the speed output of the motor by 1/10. See figure 7.2.1.2, figure 7.2.2.1 and equation 7.2.1.1.

$$\omega_{wheel} = \frac{1}{10}\omega_{rotor} = g_r\,\omega_{rotor} \qquad (7.2.1.1)$$

The opposite relation yields for torque. As in equation 7.2.1.2:

$$T_{rotor} = \frac{1}{10}T_{wheel} = g_r\,T_{wheel} \qquad (7.2.1.2)$$

The EC 60 flat motor is modelled by a PMSM block, figure 7.2.1.2, found in the SimPowerSystems [4] library. For a good motor representation the values given in the EC 60 flat motor datasheet, [26] #412825, is used for the parameterization illustrated in figure 7.2.1.1. Not much calculation was needed, except for the inertia, which is used to describe the total inertia of the vehicle.

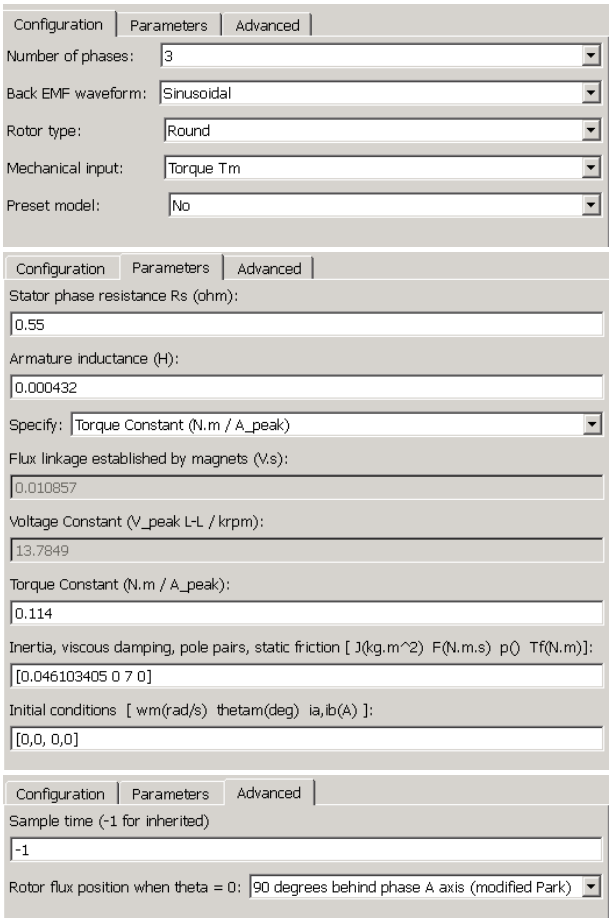

Figure 7.2.1.1: PMSM parameterization

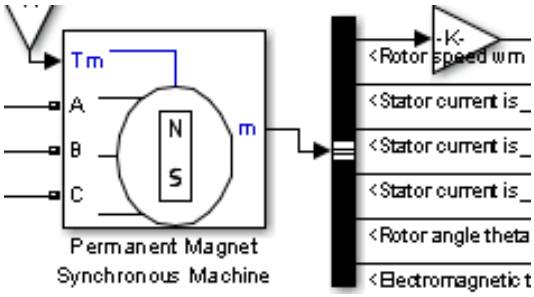

Figure 7.2.1.2: PMSM block with gear multiplier on output speed

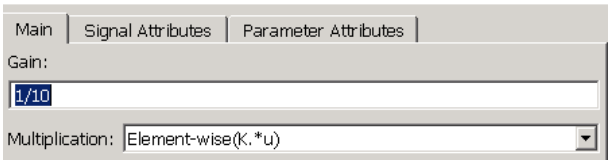

Figure 7.2.1.3: Gear multiplier block parameterization

The first page, “Configuration”, of figure 7.2.1.1 was pretty straight forward. As the EC 60 flat motor is three-phase and has sinusoidal back induced voltages these settings where set directly. In the data sheet the terminal inductance is defined as a constant value that does not vary with rotor position. This indicates that the motor has surface mounted magnets. See part 3.2. Magnets has almost the same permeability as air thus it is safe to assume that the rotor may be set as round, and not salient pole. Torque is set as mechanical input as the load model, part 7.2.2, will be set as a torque load. The model is not pre-set as the next variables will be set manually.

List 7.2.1 describes how the parameters found on the "Parameters" page in figure 7.2.1.1 is set from the datasheet: [26]. Total vehicle weight includes the driver, thus 80kg (50kg+30kg). See part 2.4. Wheel radius is assumed to be 0.239 m based on mechanical data provided by the mechanical part of the team: [1].

Stator phase resistance	Wye (Y) connected: $R_s = 1.1\ \Omega_{phase-phase} = \frac{1.1}{2}\Omega = 0.55\ \Omega$	*(7.2.1.3)* [26]
Armature inductance	Wye (Y) connected: $L_a = 0.864\ mH_{phase-phase} = \frac{0.000864}{2} H = 0.000432\ H$	*(7.2.1.4)* [26]
Torque constant	$T_{const} = 114\frac{mNm}{A} = 0.114\frac{Nm}{A}$	*(7.2.1.5)* [26]
Inertia	$\frac{1}{2}m_{tot}v^2 = \frac{1}{2}m_{tot}(r\ g_r\ \omega_{rotor})^2$ $\frac{1}{2}J^*_{car}\omega^2_{rotor} = \frac{1}{2}m_{tot}r^2g_r^2\omega^2_{rotor}$ $J^*_{car} = m_{tot}r^2g_r^2$ $J^*_{rotor,eq.} = J^*_{car} + J_{rotor} + J_{wheels}$ $J^*_{rotor,eq.} = m_{tot}r^2g_r^2 + J_{rotor} + \frac{1}{2}m_{wheel}r^2g_r^2$ $J^*_{rotor,eq.} = 80 * 0.239^2 * \left(\frac{1}{10}\right)^2 + 0.000121 + \frac{1}{2} * 1 * 0.239^2 * \left(\frac{1}{10}\right)^2$ $J^*_{rotor,eq.} = 0.046103405\ kg\ m^2$	*(7.2.1.6)* *(7.2.1.7)* *(7.2.1.8)* *(7.2.1.9)* *(7.2.1.10)* *(7.2.1.11)* *(7.2.1.12)*
Pole pairs	$p = 7$	*(7.2.1.13)* [26]
Static friction and viscous damping	Neglected. Set to zero.	
Initial condition	All set to zero. Standard initial conditions.	

List 7.2.1: PMSM model parameter calculation

The total rotor inertia equivalent calculated in equations 7.2.1.6-12 needs to be tested. A way of doing this is checking to see if the acceleration constant of the vehicle, with a 200W supply, is within realistic limits.

$$\tau_{200W} = \frac{\frac{1}{2} J^*_{rotor,eq.} \omega^2_{rotor,nom}}{P_{nom,200W}} = \frac{\frac{1}{2} * 0.046103405\ kg\ m^2 * (29.06 * 10)^2\ rad^2/s^2}{200\ kg \frac{m^2}{s^3}} \quad (7.2.1.14)$$

$$\tau_{200W} = 9.73\ rad^2\ s \quad (7.2.1.15)$$

In equations 7.2.1.14-15 the acceleration equivalent was calculated. The result was 9.73 seconds. Note that angles (like rad) are dimensionless. This is a realistic acceleration for the vehicle, thus the total rotor inertia equivalent was assumed to be a good enough estimate.

On the last page of the PMSM block parameterization, “Advanced”, the sample time is set to -1 so that the sample time matches the rest of the system as set in the powergui block. The rotor flux position is set to modified park so that it matches the other park transform blocks in the system. See parts 3.1.2 and 7.4.

7.2.2 Load model description and parameterization

Equations 7.2.2.1-6 is the mathematical derivation for the load model of the system in figure 7.2.2.1. The rolling resistance force (F_{roll}) and the air resistance constant (c_{air}) was calculated by the mechanical part of the team. See [1]. The rolling resistance force is assumed constant while the vehicle is rolling and the air resistance force increases with 2nd exponent of the vehicle speed. Steady state friction load is not included as it has a very small impact compared to the initial force required by the large inertia constant of the vehicle.

$$T_{m,rotor} = g_r T_{m,wheel} = g_r (T_{roll} + T_{air}) \quad (7.2.2.1)$$

$$T_{m,rotor} = g_r (F_{roll}\, r + F_{air}\, r) \quad (7.2.2.2)$$

$$T_{m,rotor} = g_r (F_{roll}\, r + c_{air}\, v^2\, r) \quad (7.2.2.3)$$

$$T_{m,rotor} = g_r (F_{roll}\, r + c_{air}\, (\omega_{wheel}\, r)^2\, r) \quad (7.2.2.4)$$

$$T_{m,rotor} = g_r (F_{roll}\, r + c_{air}\, r^3\, \omega^2_{wheel}) \quad (7.2.2.5)$$

$$T_{m,rotor} = \frac{1}{10} (1.05 * 0.239 + 0.02286 * (0.239)^3\, \omega^2_{wheel}) \quad (7.2.2.6)$$

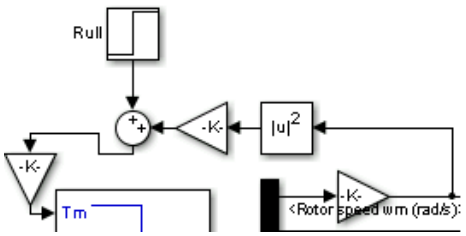

Figure 7.2.2.1: Load model blocks

Rolling resistance force is represented in the model, figure 7.2.2.1, as a step function which triggers from zero at 0.5 seconds of simulation time. It is done this way because the vehicle will not start rolling before 0.5 seconds has passed. See part 7.4.

7.3 Inverter model

7.3.1 Complex inverter and battery model

For the complex inverter model the simulation type setting has to be set to discrete. If this is not done the simulation will most likely crash, due to zero crossings during MOSFET model calculation. Simulation time step was set to 5µs. The switching frequency was set to 17 kHz, thus the simulation time step is much faster than the switching speed time step. See equation 7.3.1.1. A switching frequency of 17 kHz was a realistic value for the model, but an optimal frequency had to be found by measurements, which was not done at the time of simulation. For more information about switching frequency. See parts 4.1 and 8.5.

$$T_{tri} = \frac{1}{f_{tri}} = \frac{1}{17000\ Hz} = 58.8\ \mu s \qquad (7.3.1.1)$$

Figure 7.3.1.1 illustrates the complex inverter system model with battery and soft start circuit. Starting off with the description of the battery model.

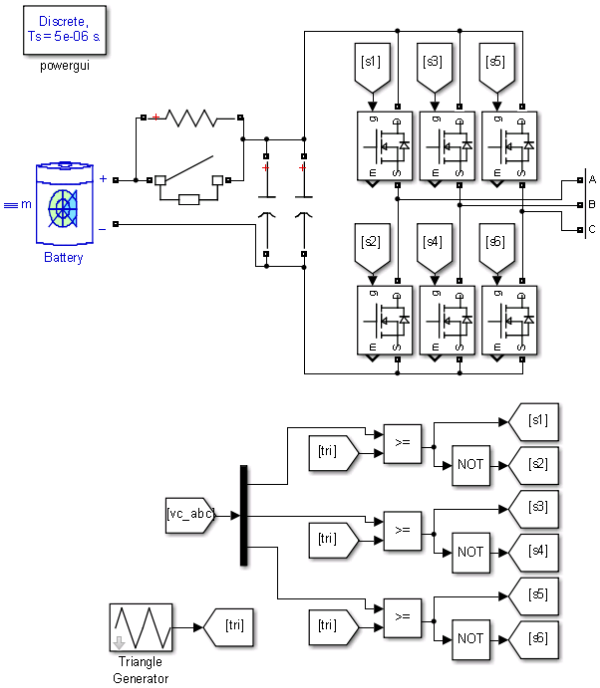

Figure 7.3.1.1: Inverter and battery, with soft start circuit, model

The batteries used are the ANR26650M1-B bought from Gylling. See part 2.5 for the competition energy source description and [56] for the data used for the battery model.

The battery type was set to lithium ion, which is the battery type that will be used in the vehicle. There was fourteen batteries connected in series with a nominal voltage of 3.3 V each [56]. The total nominal voltage is calculated as in equation 7.3.1.2:

$$14 * 3.3\ V = 46.2\ V \qquad (7.3.1.2)$$

The rated capacity of each battery is 2500mAh [56]. As there was two series connected in parallel the total battery capacity becomes twice that amount. As in equation 7.3.1.3:

$$2 * 2500\ mAh = 5000\ mAh = 5\ Ah \qquad (7.3.1.3)$$

Initial state-of-charge was set to 95%. The rest of the battery parameters was automatically set based on the nominal values.

The circuit that is between the battery and the three-phase inverter bridge in figure 7.3.1.1 is the soft start circuit. It is a circuit that ensures low current during start-up of the system. Without this circuit the capacitors on the three-phase bridge would draw very high currents while charging up. During the first 0.45 seconds of simulation time the switch in the circuit is open, thus all current has to go through a 10 ohm resistance instead. Assuming that the capacitors are ideal short circuits at start up, then the maximum current in this period is calculated as in equation 7.3.1.4:

$$I_{start-up,max} = \frac{V_{max}}{R_{soft}} = \frac{3.6V * 14}{10\ \Omega + 0\ \Omega} = 5.04\ A \qquad (7.3.1.4)$$

100% charge voltage found at [56].

After 0.45 seconds of simulation time the capacitors have had enough time to charge and the switch is closed. Thus ending the start-up period.

Connected on the right side of the soft start circuit model in figure 7.3.1.1 is the three-phase bridge with two capacitors in parallel. The capacitors is needed to handle ripple current from the three-phase bridge. For more information on how the inverter works see chapter 4. One capacitor was set to 2.2 µF while the other was set to 6000 µF. As on the inverter circuit board used in the vehicle. The last one is the sum of six 1000 µF capacitors in parallel.

The switches of the three-phase bridge was modelled with six MOSFET models found in the SimPowerSystems [4] library. Standard model parameter settings was used as the MOSFETs that would be used in the vehicle was not known at this time. When a positive gate signal is applied the MOSFET model turns on. A gate signal equal to zero turns off the MOSFET model. The connections between the MOSFETs and phases are clearly shown in figure 7.3.1.1 and explained in part 4.1.

In order to control the switches of the three phase bridge six inputs, one gate signal for each switch, are produced by the PWM circuit found on the bottom of figure 7.3.1.1. See also figure 4.1.2. The input of the PWM circuit are the three voltage control signals, one for each phase, from the controller circuit. Each of the voltage signals are compared with a triangle signal with an amplitude of 1. If, in an instant, the voltage signal is greater than the triangle signal the upper switch of the corresponding phase is turned on. If that is not true then the lower switch is on. This way the voltage signal is mimicked with pulses on each phase of the PMSM. The frequency of the triangle signal was set to 17 kHz, which also decides the switching frequency of the system.

7.3.2 Simple inverter model

The inverter model presented in part 7.3.1 was very complex, thus very demanding to simulate. For some purposes, like tuning PI regulators and testing, great detail was not needed. In order to reduce calculation time a simple inverter model developed. Illustrated in figure 7.3.2.1.

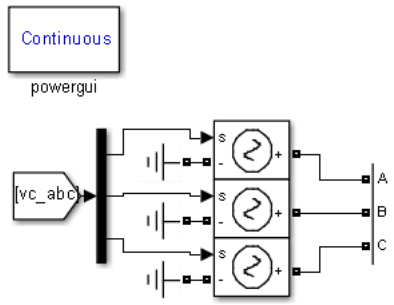

Figure 7.3.2.1: Simple inverter model

Controlled voltage sources replaced the inverter model. These model blocks takes the three controller voltage signals as inputs and translates them directly to phase voltages. The phase voltages connected to the motor are sinusoidal, not pulsed, when these blocks are used instead.

As there are no switch models in the simple inverter model continuous simulation was used.

The simple inverter model was not used to produce results for the thesis. Only for testing. A comparison of simple and complex inverter test results is found in appendix A.5. The main difference between using the simple and the complex model, is the high frequency component in the complex inverter model simulation results. This happens because the phase voltages are pulses instead of sinusoidal.

7.4 Controller model

Now the controller model will be described. The model blocks used for this purpose in the simulation model is presented in figure 7.4.1. Compared to the current regulator presented in part 5.2.2 and the PMSM vector controller presented in part 5.1 there are some differences. The d-axis current (is_d) reference is set to zero which would mean zero flux weakening. In order to simulate the effect of the driver a speed PI regulator is added on the q-axis current (is_q) reference input. At 0.5 seconds the driver is assumed to require a speed of 29.06 rad/s. Simulated as a step function going from 0 to 29.06 at simulation time 0.5 seconds. It is the same as 25 km/h according to equation 7.4.1. 25 km/h is the required average speed in the competition as mentioned in part 2.2.1.

$$25\frac{km}{h} * \frac{1000}{(60*60)}\frac{h}{ks} = \frac{6.944\frac{m}{s}}{0.239\frac{m}{rad}} = 29.056\frac{rad}{s} \qquad (7.4.1)$$

The PI regulator used for the speed regulator also has a saturation function which is used to limit the available acceleration. See how this affects the results in part 7.5.

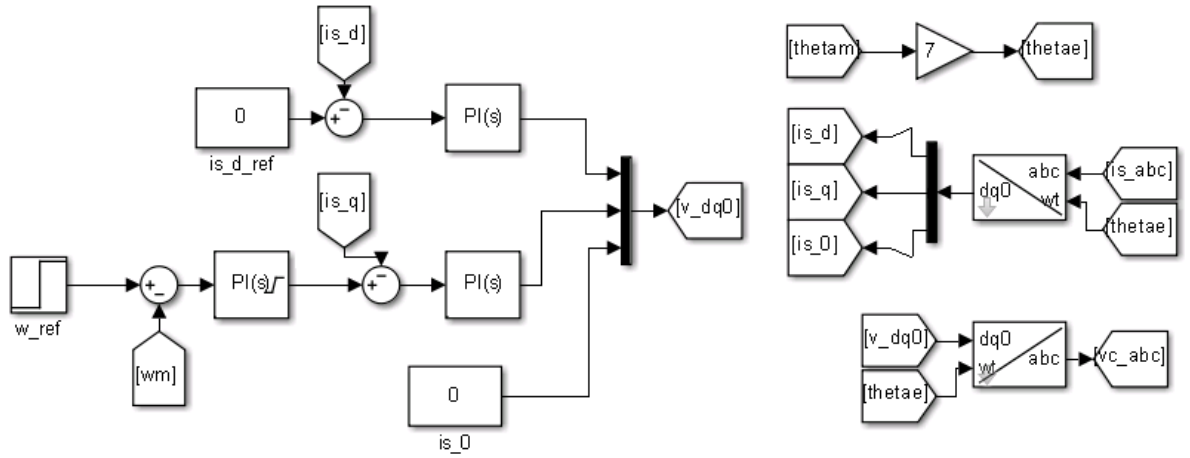

Figure 7.4.1: Controller system simulation model blocks

The simulation controller model lacks some of the functions featured in the two other controller models previously presented in this thesis. It does not include the decoupling terms presented in figure 5.1.1 and the current sum and voltage centring regulators presented in figure 5.2.2.2. Including the decoupling terms could have reduced the variation in d-axis current PI regulator gain as seen in appendix A.5. The current sum and voltage centring regulators could also have been included. The zero sequence component (is_0) is set to zero. See equation 3.1.2.6. The dq transformations are set as "modified Park's transformations". This is described in part 3.1.2. Including the missing regulator circuits in the simulation model is relevant for further analysis.

7.5 Prototype vehicle with EC 60 flat motor simulation results and discussion

Observations from the first simulation results lead to choices made for the next simulations. The discussion of this part is therefore mixed with the results instead of being separated in two different parts.

The main simulation analysis goal was to estimate the motor power needed to initially accelerate the prototype vehicle. It was expected that the initial acceleration was the state that would require the largest power spike. Based on the results it was possible to estimate the performance of the EC 60 flat motor. The process of creating this full system model also gave valuable early insight in how the system works in theory. All of the relevant simulation results are found in appendix A. Not all of these results will be described here. Only the ones that lead to the main thesis conclusions.

Different simulation results was produced by varying the available vehicle acceleration. This was done by changing the saturation limit parameter in the speed PI regulator as mentioned in part 7.4. Figure 7.5.1 illustrates some of the simulation results at saturation limit 20:

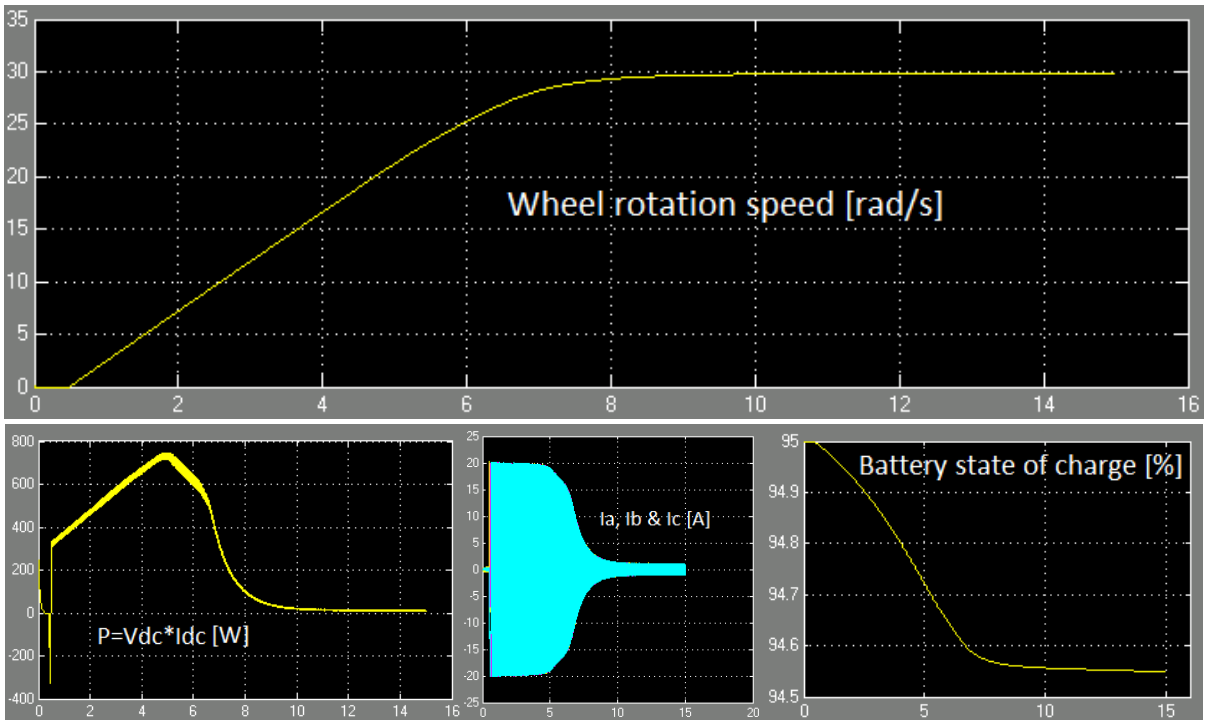

Figure 7.5.1: Prototype vehicle EC 60 flat motor simulation results, saturation limit = 20

The acceleration with saturation limit 20 is relatively fast. Desired speed is achieved after a bit more than 8 seconds. This acceleration is reflected in the power drawn from the battery which varies from 300W to 750W increasing with the speed of the motor. Remember equation 3.1.1.4. Don't mind the -300W power spike at 0.45 seconds as this is related to the relay described in part 7.3.1. With such high power consummation the 100W rated EC 60 flat motor would definitely malfunction. So fast acceleration time is not needed though in order to achieve the average 25 km/h, equation 7.4.1, requirement as the prototype vehicle only

has perform the initial acceleration once. Figure 7.5.2 illustrates simulation results using a saturation limit of 10 which leads to a less powerful acceleration.

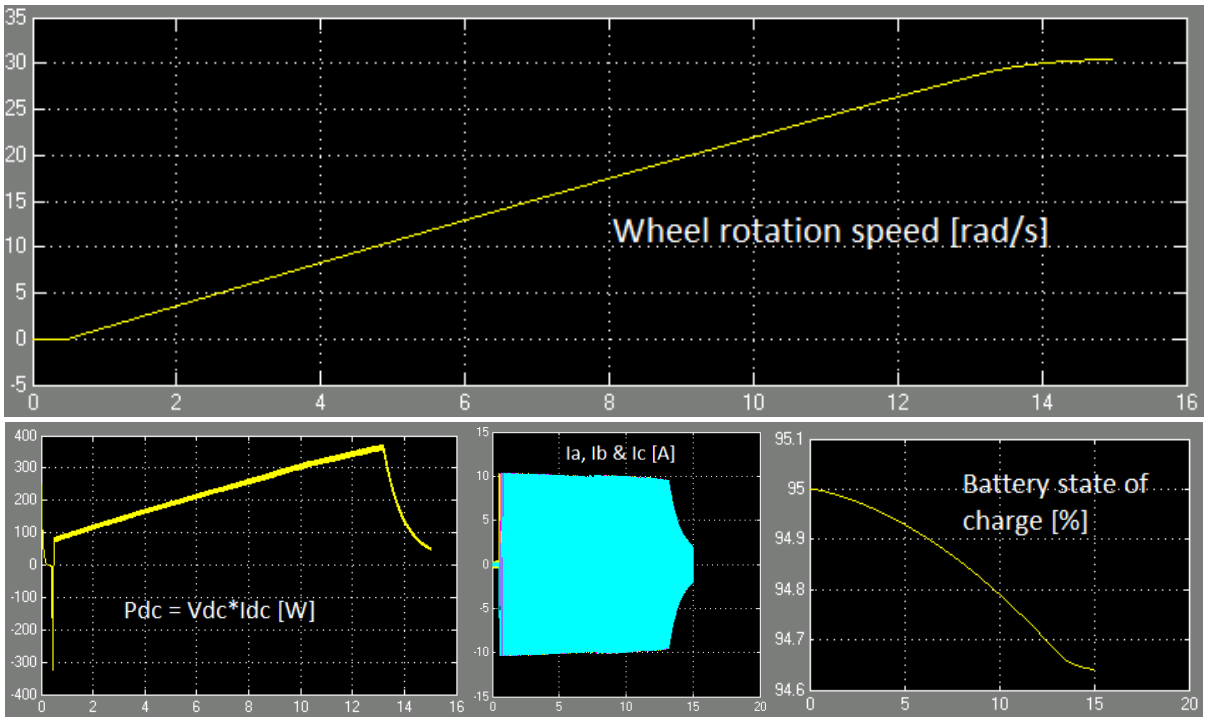

Figure 7.5.2: Prototype vehicle EC 60 flat motor simulation results, saturation limit = 10

With a saturation limit set to 10 the acceleration time was about 14 seconds and a power consumption ranging from about 100W to 375W. The acceleration time is likely close to what is expected for SEM 2014, but the power consumption is still uncomfortably high compared to the EC 60 flat power ratings given in the datasheet: [26]. In order to achieve simulation results which would be less likely to indicate a motor malfunction the acceleration time was increased further by reducing the saturation limit to 5. As the previous simulation acceleration time almost exceeded the total simulation time it was doubled to 30 seconds of simulation time for this test as shown in figure 7.5.3.

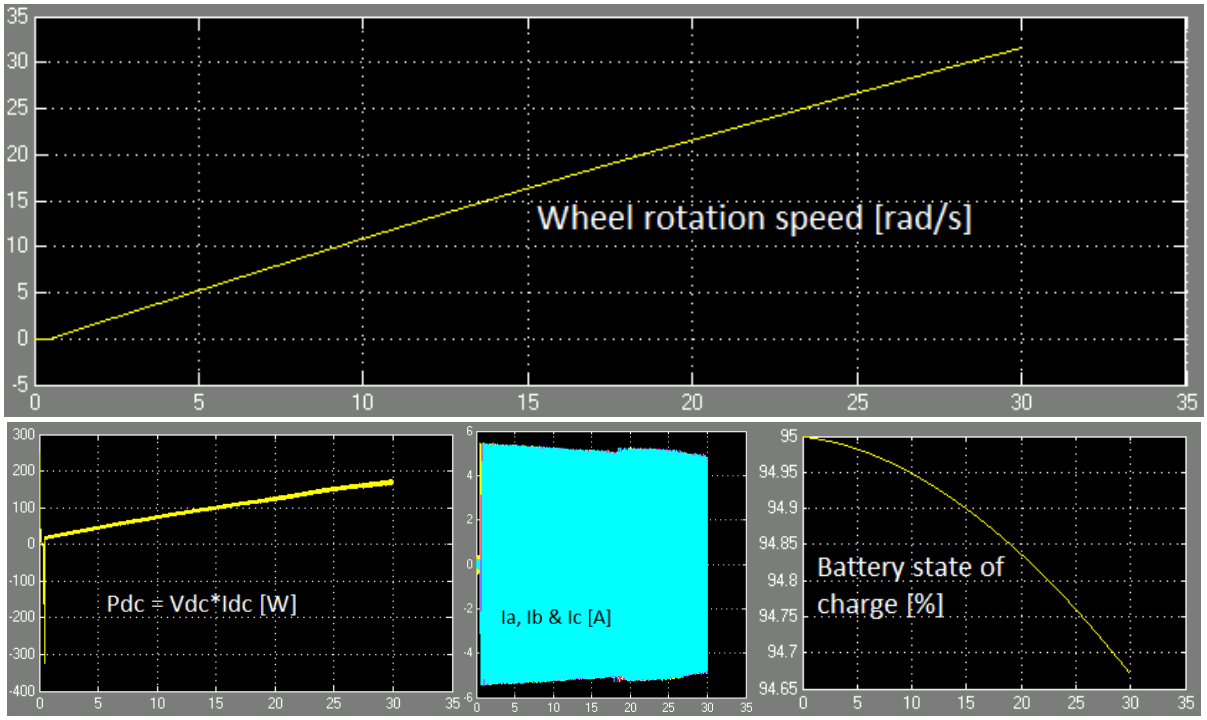

Figure 7.5.3: Prototype vehicle EC 60 flat motor simulation results, saturation limit = 5

During the last two seconds of the simulation a speed overshoot is clearly visible. This happens because the integrating part of the regulators accumulates during the long period of time that the saturation limit is active. It can be fixed by using the reset function of the integrator part of the PI regulators in the system model.

Saturation limit of 5 led to an acceleration time of about 28 seconds. So weak acceleration would mean that the vehicle must be accelerated much greater speeds in order to catch up for the time spent at low speeds. The power consummation varies from 20W to 180W. With this conditions the EC 60 flat motor was more likely to survive, but as the acceleration time is longer it also means that the motor has to handle power above the rated value of 100W for a longer period of time. Thus it was still uncertain if the motor would survive, even if the acceleration time was increased to 28 seconds, without proper testing with a real machine.

The main conclusion of this analysis was that the EC 60 flat motor had a too low power rating for its purpose, and would therefore most likely malfunction during testing or while driving. Because of this the AXI motor, part 3.4.1.2, was found and became of main interest with its higher power ratings. Some secondary solutions using the EC 60 flat motor was also developed, but it was not of main concern for the design of the other mechanical parts of the system.

A larger gear ratio could have been used to reduce the load torque, but that would just reduce increase the acceleration time even further.

The concerns made because of the poor EC 60 flat simulation performance were confirmed by a motor malfunction when it was tested on the motor test rig. See part 8.6. If simulations had not been done then the AXI motor would probably never had been found in time which could have led to failure for the whole prototype vehicle project. This proves how critical simulation is early for important decision making. It should be noted that some components of the inverter circuit board, part 4.3.2, were also replaced with components with higher current ratings because of the higher AXI motor current ratings. So it was not just the motor part of the prototype vehicle project that could fail if this discovery had not been found early.

Chapter 8: Laboratory and full system testing

A large variety of different tests was performed in order to be prepared for the competition in Rotterdam. This chapter describes all of the tests that are worthy of mentioning. How the tests were done is described, with equal priority as describing the results and conclusions made, so that the reader should be able to redo the tests if necessary.

8.1 Functional test: 2013 axial flux motor

The axial flux motor made and used for the 2013 Shell Eco-Marathon was much lighter and had a higher efficiency than the previous designs, see part 3.3.1.2, but early on in the semester the motor suddenly was not able to turn properly. The greatest weakness of this motor was that the glue between the magnets and the rotor plates was not strong enough. Because of this some magnets could get dragged off due to the strong magnetic forces inside the machine. This had already happened once during the competition in 2013.

In order to investigate the lack of turning ability the plates had to be separated. This is done by inserting four bolts into one of the rotor plates. Try to insert the bolts evenly so that the plate doesn't get skewed. Never place fingers between rotor and stator because of the large magnetic forces involved.

What was found is shown in figures 8.1.1-2. A lot of the magnets had come loose on both of the rotor plates. In order to fix the motor new magnets has to be bought and stronger glue has to be found. As the team already had more than enough tasks to take care of it was decided that fixing the motor would have to be done by the next team as long as the 2011 axial flux motor was still working.

Figure 8.1.1: 2013 axial flux motor loose magnets on rotor plate 1

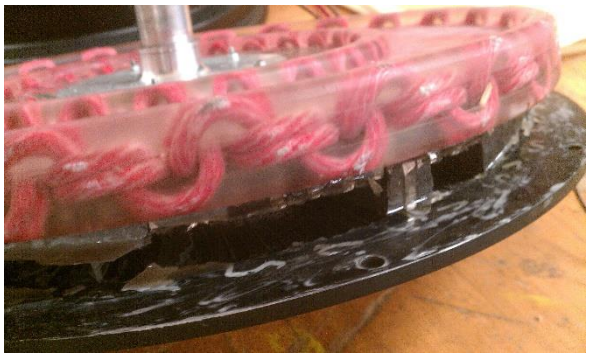

Figure 8.1.2: 2013 axial flux motor loose magnets on rotor plate 2

8.2 Functional test: 2011 axial flux motor

In order to be sure of that the axial flux PMSM from the 2011 competition was still operational a functional test had to be performed.

Test:
2011 axial flux motor functional test

Measured:
Induced RMS voltage between phases.

Equipment:
Multimeter

Result:
An average of $7V_{rms}$ induced voltage between phases. The magnitude of induced voltage varied proportionally with the speed of rotation.

Figure 8.2.1: 2011 axial flux motor functional test illustration

20.02.2014

As a result of the induced voltage between all phases it was safe to assume that the motor was still working properly. This was important to find out early as a motor test rig had to be built and an operational motor for the urban concept vehicle had to be found.

8.3 Functional test: AXI motor

The AXI motor found in the workshop had to be tested to ensure that it was still working. This was done much in the same way as the axial flux motor functional test.

Test:
AXI motor functional test

Measured:
Induced voltage between phases.

Equipment:
Oscilloscope
Drill

Result:
Sinusoidal 2.5V_{rms} voltage between phases. The magnitude of induced voltage varied proportionally with the speed of rotation.

Figure 8.3.1: AXI motor functional test illustration

26.02.2014

Using the same assumption as in part 8.2 it was concluded that the AXI motor was still working. This was good as it was important to have a plan B in case the ordered EC 60 flat motor fails testing.

8.4 Motor test rig set up

8.4.1 Overview

A motor test rig was set-up in order to test the overall system efficiency and control. This part describes how it was set up. Some of the work will not be described in great detail. Especially the mechanical part of the test rig as most of it was done by the power electronics workshop.

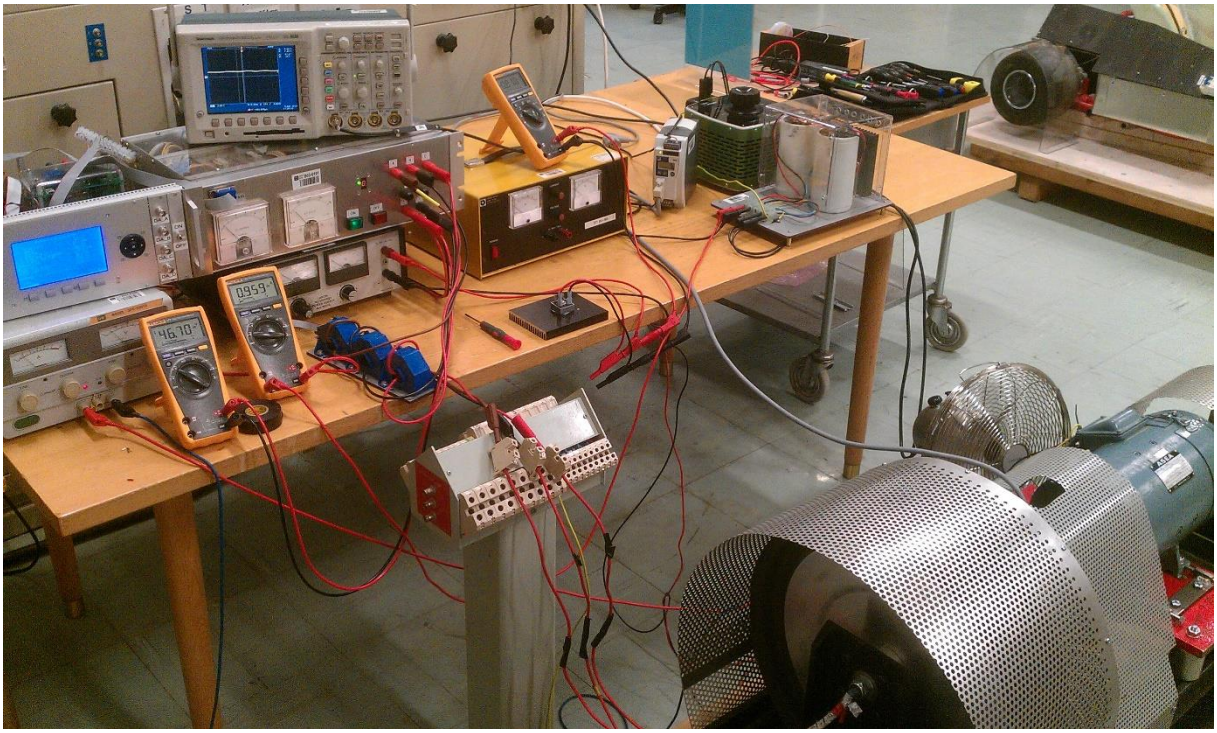

Figure 8.4.1.1: Overall test rig system with 2011 axial flux motor mounted to the rig

Figure 8.4.1.1 illustrates the overall test system. There were several different parts of the system that needs to be described. How to set up the test rig will now be described in two main categories: Mechanical and electrical.

8.4.2 Mechanical set-up

The mechanical part of the system is described first. This part of the system may be seen in the lower right corner of figure 8.4.1.1. It is also shown in figures 8.4.2.1-2.

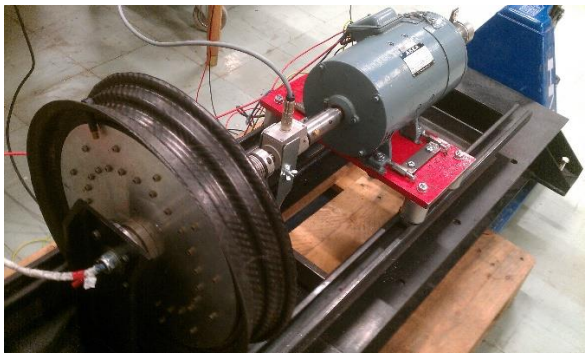

Figure 8.4.2.1: Test bench mechanical system with 2011 axial flux motor mounted to the rig, picture angle 1

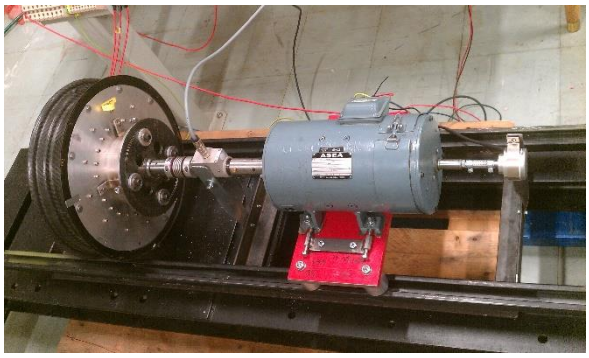

Figure 8.4.2.2: Test bench mechanical system with 2011 axial flux motor mounted to the rig, picture angle 2

The first challenge that had to be dealt with was the stationary axle of the 2011 axial flux motor. As the outer part was the one spinning some sort of connection between the motor and the main rotating axle, an axle adapter, had to be made.

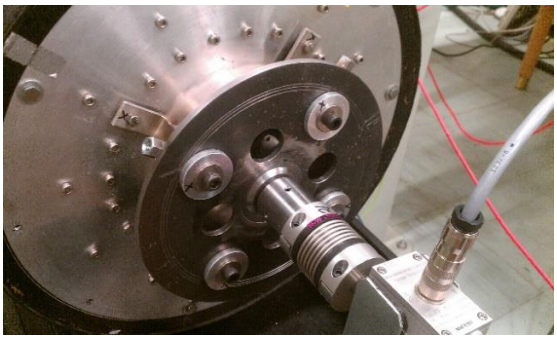

Figure 8.4.2.3: Axial flux motor axle adapter illustration

The solution used is illustrated in figure 8.4.2.3. Some investigation of old pictures of the motor production, [24], proved that the screws seen from the outside are the ones that holds the magnet plates in place. All of the screws holds the same plate, thus loosening four of these screws would not damage the motor. The axle adapter was connected to these four screws based on this assumption.

A torque transducer was needed for measuring the torque between the motor and the breaking machine. It was an expensive device. To make matters worse it is also easy to break such devices. Therefore proper axle fixing for the torque transducer was important. The middle part in figure 8.4.2.4 is the torque transducer. On the left side a device that absorbs bending force is placed. Additionally, the axle is carefully aligned to prevent bending.

It is not only bending force that may break the thin axle within a torque transducer. Providing a greater torque than the rated value may also break it. The torque transducer which was used for this thesis work was rated for 10 Nm, but it could go as high as 30 Nm without breaking.

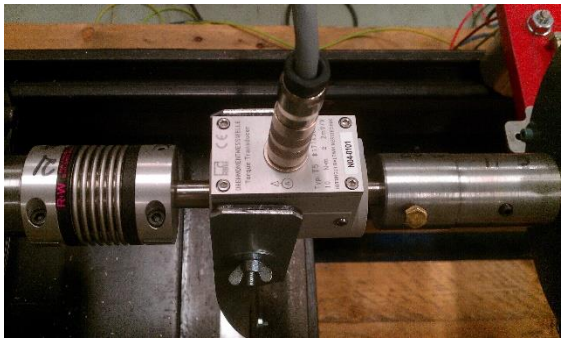

Figure 8.4.2.4: Torque transducer mount illustration

Initially a couple of roller bearings separated the transducer and the motor in order to provide safer operation. See figure 8.4.2.5. This was not used in the final set-up, however, as there was too much friction. This friction would lead to that the transducer would measure a much lower torque than what the motor was actually providing.

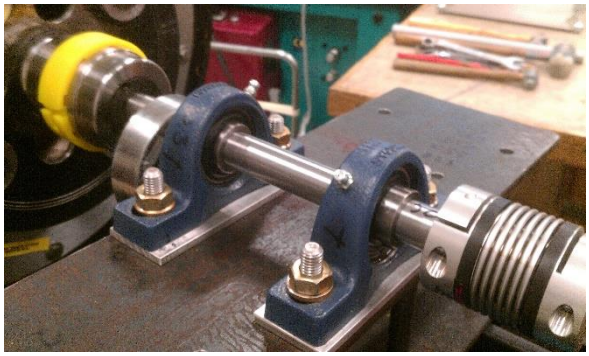

Figure 8.4.2.5: Torque transducer mount illustration

Figure 8.4.2.6 illustrates the DC machine that is used to electrically provide breaking force on the axle. The input of a DC machine is field current and the output, operated in this way, is the armature current. How the machine is electrically connected to the rest of the test bench system is described in part 8.4.3.

How the ROD 420 encoder was mechanically connected to the axle is shown in figure 8.4.2.7. It is supposed to measure the rotor position of the mounted motor, not the DC machine, but as the axle is very stiff the rotor position measured from this side is accurate enough. The connection between the encoder and the axle was made by a simple plastic tube, including a pair of tube clamps, as the encoder has a relatively low inertia and friction.

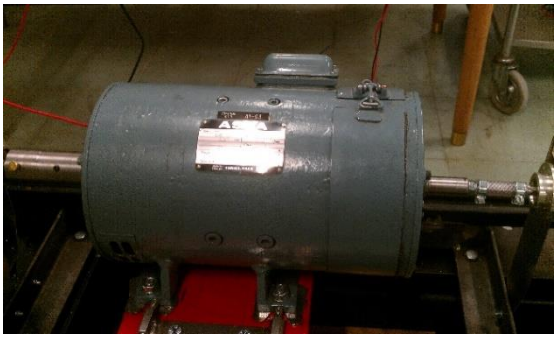

Figure 8.4.2.6: DC machine illustration

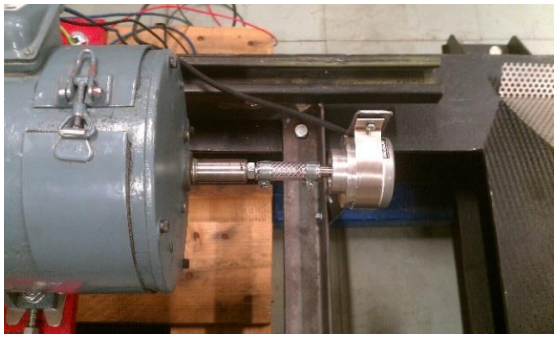

Figure 8.4.2.7: Encoder, ROD 420, test bench axle connection illustration

8.4.3 Electrical set-up

Starting off with the DC-source. The DC-source were used to represent the batteries of the electrical system.

Figure 8.4.3.1: DC source 40V/10A, B02-0365

Figure 8.4.3.2: Rectifier, B02-0562, (left) and variac 0-240V, B01-0426, (right)

During the first measurements the DC source in figure 8.4.3.1 was used, but it proved to be too weak for some of the high power measurements. Because of this it was later replaced by a variac and a rectifier, figure 8.4.3.2, which could provide more power.

The DC source provides power to the inverter. While the inverter circuit board, part 4.3, was not finished the tests that were done used a 3kW IGBT inverter instead. See figures 8.4.3.3 and 8.4.3.4.

Figure 8.4.3.3: 0-350V 10A, 3U rack, inverter, B03-0191, front

Measurements of the DC voltage for the controller and multimeter were connected to the front + and – as may be seen in figure 8.4.3.3. The three output phases A, B and C of the inverter was connected to the three phase PMSM. The cable in the upper left corner of figure 8.4.3.3 was for the 6 pulse input, and was also the driver interface connection, from the controller.

Figure 8.4.3.4: 0-350V 10A, 3U rack, inverter, B03-0191, back

A concern was that power would go in the reverse direction and damage the DC source when the motor was breaking. In order to prevent this the DC source was connected to the INN ACDC input at the back of the inverter as illustrated in figure 8.4.3.4. Connected in this way the DC source is rectified into the inverter. Thus DC current would not be able to go in the opposite direction and damage the DC source. The other connected cable in figure 8.4.3.4 is the supply for the control and display system of the inverter.

At first an identical inverter did not function properly. The DC voltage increased slowly, but that was just because of leakage current coming from the drive circuit. After some investigation it was discovered that a fuse, located inside the inverter, was the cause of the problem. The fuse has a long delivery time so the inverter was replaced by the one described earlier instead of changing fuse. This fuse, figure 8.4.3.5, is often the problem if this kind of inverter is not working.

Figure 8.4.3.5: Fuse inside 3kW inverter

Figure 8.4.3.6: SINTEF FPGA module for inverter control front

The inverter presented previously did not control itself. It was controlled by 6 pulse inputs given from an inverter controller module. Figures 8.4.3.6-8 illustrates the controller used on this test bench. The actual control unit was the SINTEF FPGA, part 5.2.2, located in the centre of figure 8.4.3.8. Remaining parts were for power supply, adapters, FPGA menu screen and voltage measurement.

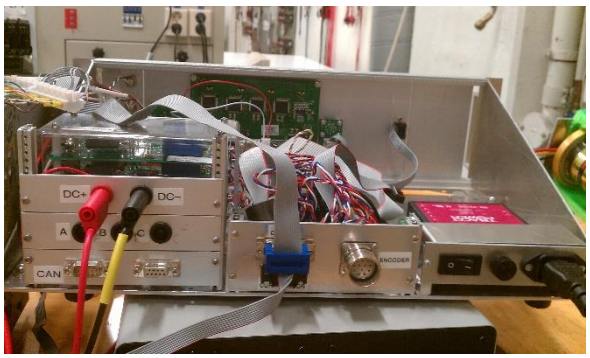

Figure 8.4.3.7: SINTEF FPGA module for inverter control back

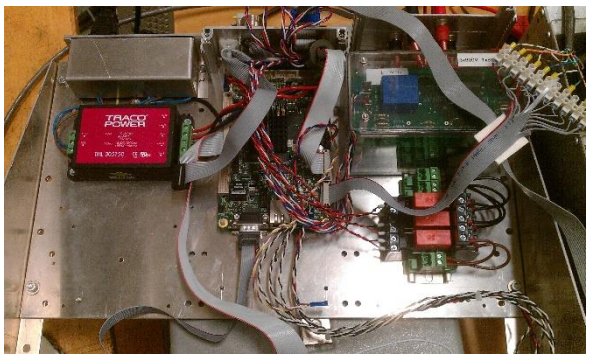

Figure 8.4.3.8: SINTEF FPGA module for inverter control top

On the upper right side of figure 8.4.3.8 a similar adapter of the one illustrated in figure 6.4.1 is visible. This encoder adapter was presented in part 6.4. In figure 8.4.3.7: The DC+ and DC- connection was for the DC voltage measurement which was connected to the + and – connection on the inverter, figure 8.4.3.3, as described earlier. The upper cable in the middle of figure 8.4.3.7, with blue connector, is the driver interface connection of the controller which was used to control the inverter. On the lower right side the power supply for the controller is plugged in. The lower cable in the middle of figure 8.4.3.7, with black connector, is the current measurement input. Connected here are the LEM current measurement devices. See figure 8.4.3.9.

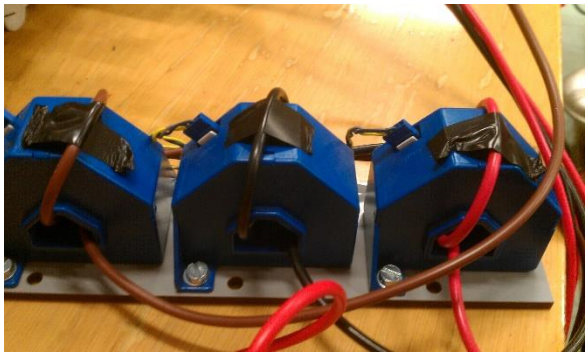

Figure 8.4.3.9: LEM current sensors used for the motor test rig

These LEM devices are simply transformers. By twisting the A, B and C phase wires a couple of times a coil in each device induces a much smaller current in the measurement wires. Watch the arrow on the top of each device and let the wires pass through the ring in the same direction. The fact that the wires is passed through the devices two times needed to be considered when calculating the "I meas. AD full scale" in list 5.5.1. Because of this the parameter actually became identical to that for the inverter circuit board LEM devices, part 4.3.2.2, as the transfer ratio is double:

$$I\ AD\ param. = \frac{2000}{2} * 2 * 25mA = 500\ [\frac{1}{10}A] \qquad (8.4.3.1)$$

In order to provide breaking power to the rig the DC machine had to be provided with a field current as well as an armature current connection. Figure 8.4.3.10 illustrates the DC source used to provide the field current. By regulating the field current with this DC source the right amount of breaking power may be achieved.

Figure 8.4.3.10: DC source, B02-0360, providing field current to the DC machine

Figures 8.4.3.11-12 illustrates the two components connected in parallel to the armature connection of the DC machine. The rectifying bridge protected the armature DC source from reverse currents/over voltages by creating a short circuit when the DC machine output voltage became higher than the armature DC source voltage.

For high speeds the DC machine provided enough breaking power with the armature DC source turned off so twhile the rectifier bridge acted like a short circuit. The rectifier bridge should be mounted to a heat sink, as illustrated in figure 8.4.3.12, in order to prevent overheating during this operation. For low speeds, however, the short circuit was not enough. By turning up the armature DC source voltage a reverse force was applied, thus enabling greater breaking force. In order to ensure that the rectifier bridge was connected in the correct direction a test having only the armature DC source connected to it was applied. If it did not short circuit when the DC voltage was applied then it was connected correctly. By

switching the polarity it could be ensured that it did short circuit in the opposite direction. Note: Remember to switch back to original polarity after this test.

Figure 8.4.3.11: DC source, B02-0389, providing armature current to the DC machine

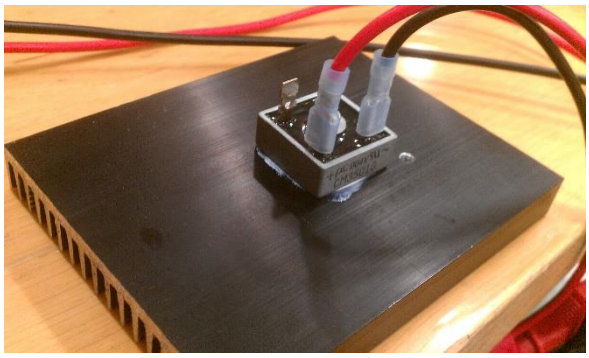

Figure 8.4.3.12: Rectifying bridge connected in parallel with the armature DC source and DC machine windings

Figure 8.4.3.13: Torque transducer signal receiver, N04-0096

A transducer signal receiver, figure 8.4.3.13, was needed in order adjust the system for the different torque values. The input to this device came from the torque transducer displayed in figure 8.4.2.4. It had a small screen that illustrated the current torque input signal. During operation the torque would alternate to some degree. In order to get an idea of the torque ripple that was occurring in the system the torque signal was shown on an oscilloscope as well: Figure 8.4.3.14.

Two multimeters was used for measuring the inverter DC side voltage and current as illustrated in figure 8.4.3.15. The multimeter measuring DC voltage was connected to the connections marked with + and – in figure 8.4.3.3. The multimeter measuring DC current is connected in series between the positive polarity of the DC voltage supply, figures 8.4.3.1-2, and the inverter AC power IN connection, figure 8.4.3.4.

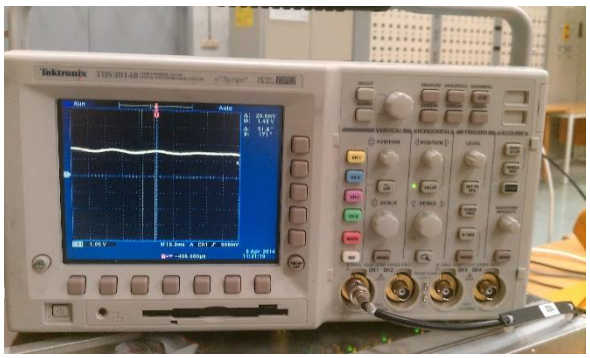

Figure 8.4.3.14: Oscilloscope with torque transducer input for torque ripple analysis

Figure 8.4.3.15: Multimeters for measuring inverter DC side voltage and current

A fan was used to keep the DC machine cold while testing over a longer period of time. The lid covering the brushes on the machine may be removed, as in figure 8.4.3.16, for better cooling. The fan that was used was not optimal for the purpose of cooling the DC machine. A fan with more concentrated air flow would have been better, but the machine was kept cold enough for the tests performed during this thesis work.

Figure 8.4.3.16: Fan set-up for preventing overheating in the DC machine

8.5 Efficiency test results and discussion: 2011 axial flux motor

8.5.1 Results

All of the results from the 2011 axial flux motor, part 3.3.1.1, efficiency test is found in appendix B.1. Not all of them will be described in detail. The first and most important result achieved was the diagram illustrating the efficiency of the 2011 axial flux motor for varying motor output torque and rotation speed. As there are two variables the results may be presented as a three dimensional graph as in figure 8.5.1.1:

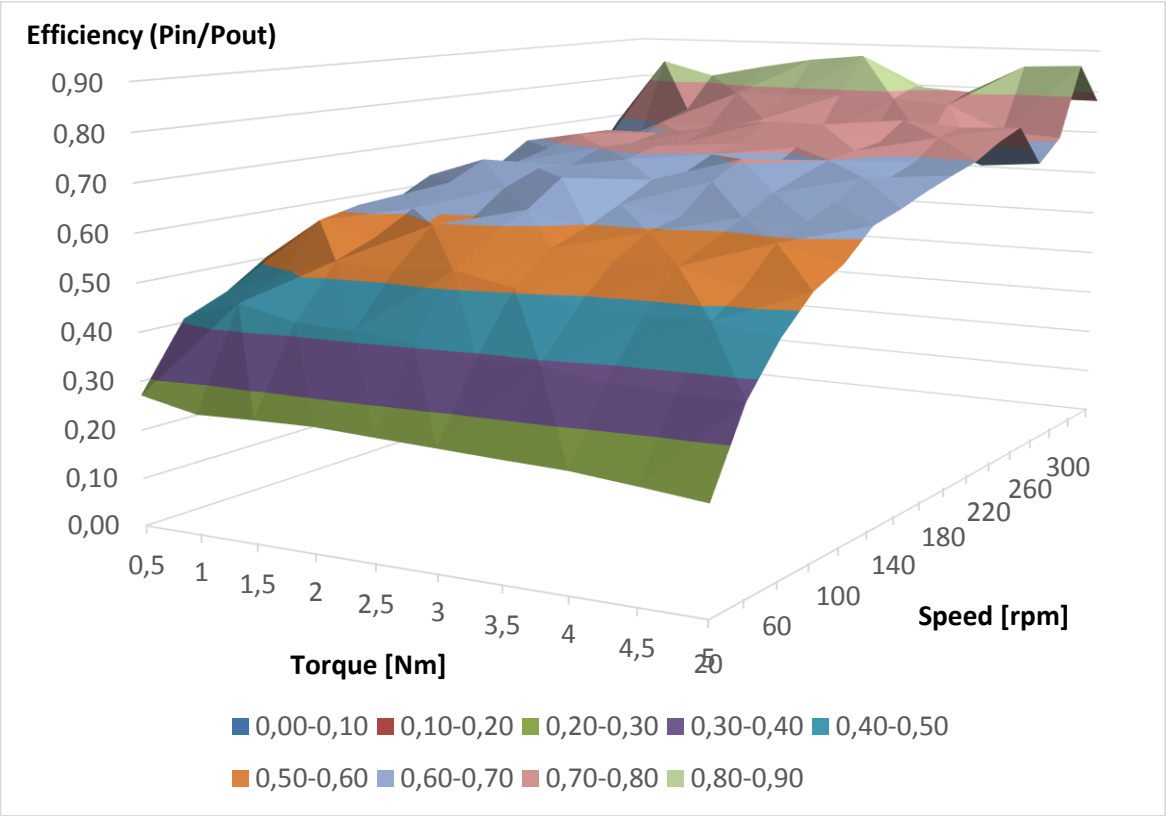

Figure 8.5.1.1: 3D efficiency diagram for 2011 axial flux motor

As three dimensional models are not easy to analyse a couple of two dimensional plots were produced from the same data set. One plot for constant 2 Nm torque, figure 8.5.1.2, and another for constant 280 rpm motor rotation speed as in figure 8.5.1.3.

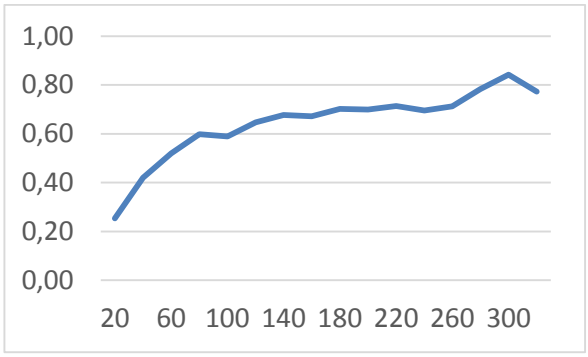

Figure 8.5.1.2: Efficiency diagram 2011 axial flux motor: 2 Nm plot, speed [rpm] on horizontal and efficiency on vertical axis

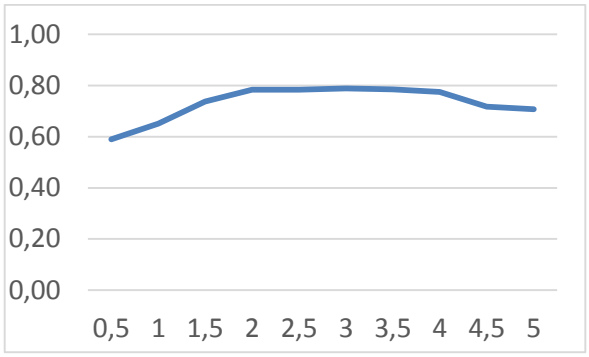

Figure 8.5.1.3: Efficiency diagram 2011 axial flux motor: 280 rpm plot, torque [Nm] on horizontal and efficiency on vertical axis

Next similar data to what is represented in figures 8.5.1.1-3 was produced again, but with a few changes. First the step size was doubled in order to be able to produce the results in time. The work was under a constant time pressure as the test rig had to be delivered quickly back to the power electronics workshop in order to switch motors for other tests. The next data that was produced was done with a higher voltage, about 50V-56V instead of about 30V-46V, which was used earlier. Another data set was also produced by only changing the switching frequency from the previous 15 kHz to 4 kHz. These results are not presented here as they became very similar to the ones presented in figures 8.5.1.1-3. They are, however, found in appendix B.1.

In order to properly investigate the effect of switching frequency an efficiency test with switching frequency varying from 1-25 kHz was done. The result is illustrated in figure 8.5.1.4:

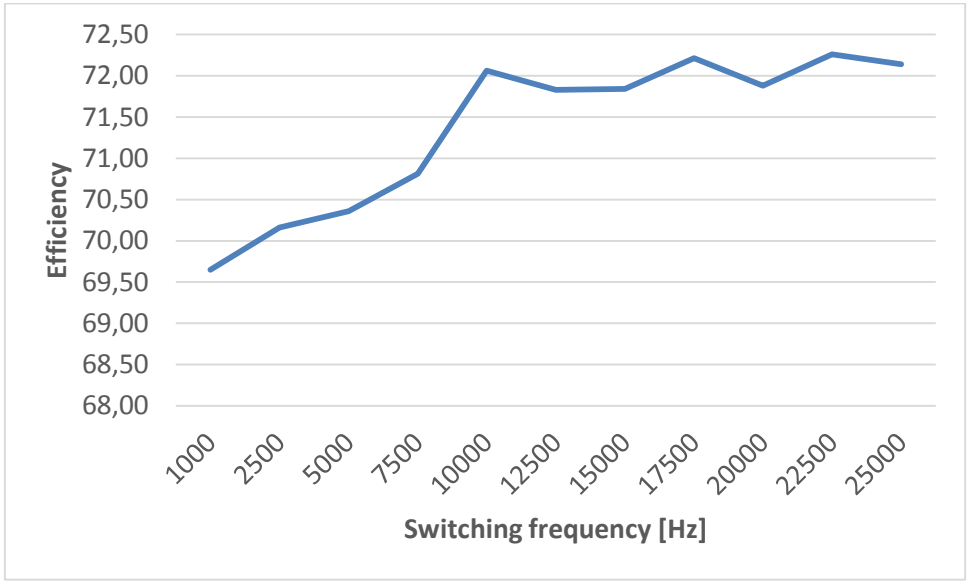

Figure 8.5.1.4: Efficiency diagram, 200 rpm, 3.5 Nm, 1-25 kHz, for 2011 axial flux motor

8.5.2 Discussion

It should be noted that all of the efficiency tests presented in the previous part were performed by measuring the DC power input to the system. This means that the IGBT 3kW converter losses, except for the inverter drive circuit losses, are also a part of the total loss calculation of the measurements. Another important factor is that the motordrive controller was not supplied by the DC bus which means that the losses in the controller unit was not included in the total power losses.

The main efficiency test results shown in figures 8.5.1.1-3 indicates that the motor is most efficient at high speed. Preferable operation would be above 300 rpm which would mean about 29 km/h for the urban vehicle. The data also indicated some improvement at increased torque, but the differences was not significant enough for making definite conclusions. Although the high voltage and 4 kHz tests indicated an even stronger efficiency reduction with reduced torque.

Not much variation was found between the increased voltage produced data set and the initial data set. Variations found could be caused measuring inaccuracy to the same degree as the difference found in the data sets. More precise testing with several different and constant DC source voltage level tests would have had to be done in order to achieve a proper data analysis.

The 4 kHz test did not lead to any conclusive data either. This is why the 1-25 kHz test was performed. These results indicated some increase in system efficiency with increased switching frequency. As the IGBT 3kW inverter losses probably would behave a bit differently than the inverter circuit board, and the fact that the controller losses was not included in the analysis, the test results may vary from the final system results. However, MOSFETs operate better than IGBTs at high frequencies: Figure 4.1.3. In part 4.3.2.2 the transistor considerations was presented and a system based on MOSFETs was chosen. A switching frequency of 20 kHz was chosen for the final system based the test results and this fact, but unfortunately the switching frequency for the urban vehicle motordrive controller was set to 17 kHz by accident: Appendix D.1. The switching frequency for the prototype vehicle system was set to 20 kHz. A separate switching frequency efficiency test was supposed to be performed for the AXI motor with final motor controller system, part 8.7, but this test failed due to encoder position slipping. Switching frequency full system efficiency analysis is very relevant for further work.

8.6 Efficiency test results and discussion: EC 60 flat motor

A similar efficiency test as in part 8.5 had to be done for the EC 60 flat motor as well. Not only for estimating the best driving strategy, but for making sure that it would survive the loads during competition.

Test:
Efficiency test EC 60 flat motor.

Measured:
DC bus voltage and current.
Motor torque output.

Equipment:
Part 8.4 motor test rig set up.
2011 axial flux motor replaced with the EC 60 flat motor.
3kW inverter, B03-0191, replaced with the inverter circuit board. MOSFET: STB75NF75.
40V/12A DC source, B02-0365.

Result:
At 0.85 Nm applied torque at 1000 rpm: After 5 seconds of operation some smoke from the motor was observed and half of the motor power suddenly disappeared. Tried to run it again with no-load. This time all power suddenly disappeared and the motor acted like a short-circuit. The phase-phase resistance was initially 1.1 Ω, but after the incident the measured value was 0.4 Ω between all phases.

22.04.2014

Figure 8.6.1: EC 60 flat motor mounted to the motor test rig

The results indicates that the insulation between coils was degraded due to overheating. With defect insulation short-circuits occurred. When the motor was taken off the rig it was hard to turn by hand due to a damping effect. This observation leads to the same conclusion. Even though the motor was operated within the rated 100W (P= ωτ = 1000*0.10472 rad/s *0.85 Nm = 89W) it is clear that it was operated far outside of its thermal limits according to the datasheet. See [26]. The result of this test confirmed the conclusion made from the simulation model results. See part 7.5. The load applied may have been slightly greater than what would have been during the competition if this motor was used. However, it was better that the motor did not survive testing rather than risking an engine failure during the competition in Rotterdam.

8.7 Efficiency test, results, current calibration and discussion: AXI motor

After the EC 60 flat motor failure it was the AXI motor's turn on the motor test rig. At this point of time the full motor controller system was developed, except for the final S1 encoder mount, and was therefore used for the testing.

Test:
Efficiency and calibration: AXI motor test rig.

Measured:
DC side voltage and current.
AC side current.

Equipment:
Motor test rig as described in part 8.4.
AXI motor mounted to the test rig.
Inverter circuit board. MOSFET: STB75NF75.
Virtex 5 FPGA, with SINTEF motordrive controller software and FPGA module screen connected.
Traco power circuit provides power to the FPGA.
40V/10A DC source, B02-0365.
Oscilloscope with current measurement device.
The ROD 420 encoder still used for the test rig.

Result:
+/-4.5 Nm oscillations at 400 rpm. No oscillations at other speeds up to 3200 rpm.

1-25 kHz switching frequency efficiency test failed. Stator position offset changed during the test.

Current measured at all phases. They were symmetrical.

With the inverter board turned off (status 80) the direct phase current measurements, "AD I phase", for A, B and C was 12, 12 and 8 bit respectively. Reduced by the same value in parameter list so that the measurements were changed to 0 bit in this condition.

The "I AC RMS filtered" measurement in figure 8.7.5 was also tested. While in the same condition the oscilloscope measured a peak-peak value of 6.8 $A_{peak\text{-}peak}$ and the "I AC RMS filtered" measurement was equal to 21 1/10A_{rms}.

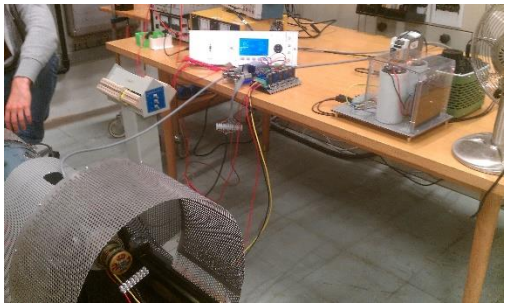

Figure 8.7.1: AXI motor test rig overview

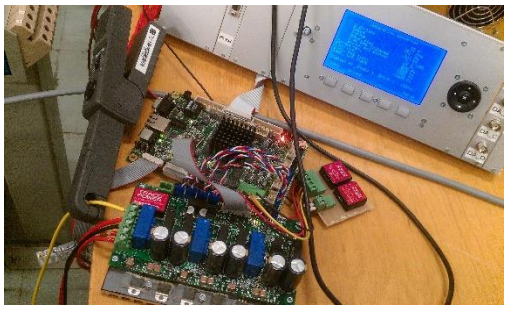

Figure 8.7.2: AXI motor test rig electrical set-up illustration

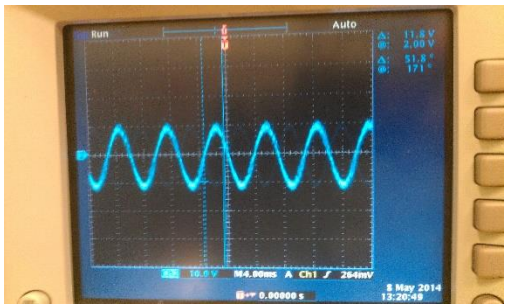

Figure 8.7.3: AXI motor test rig, AC side phase A current measurement

Figure 8.7.4: AXI motor test rig, off condition direct phase current measurement illustration

$$\frac{6.8\,A_{peak-peak}}{2\sqrt{2}} = 2.4\,A_{rms} = 24 * 1/10A_{rms} \quad (8.7.1)$$

Thus, the oscilloscope measured 24 1/10A_{rms} while the controller measured 21 1/10 A_{rms}.

08.05.2014

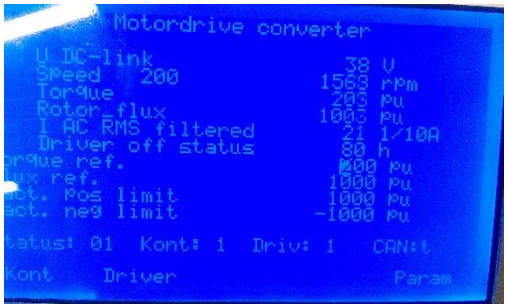

Figure 8.7.5: AXI motor test rig, AC filtered RMS measurement illustration

As mentioned in part 3.4.1.2 the AXI motor has a strong cogging effect. The +/- 4.5 Nm oscillations which occurred only around 400 rpm seemed to be caused by motor cogging vibration becoming equal to a resonance frequency in the mechanical part of the system. These oscillations made a sharp sound. The sound seemed to come from the device that protects the torque transducer from bending force. See figure 8.4.2.4. A concern was that the oscillations might be harmful for the expensive torque transducer, but the conclusion was that a motor as small as the AXI motor would not be able to provide enough force to harm the device. The experiments continued based on this conclusion.

A 1-25 kHz efficiency test, similar to the one in part 8.5, was performed, only this time with the finished inverter circuit board. See appendix B.2. Unfortunately the test failed due to change in the stator position. This fault was most likely caused by some mechanical slip on the axle between the AXI motor and the ROD 420 position sensor on the other side. The oscillations described in the previous paragraph may have been the force that caused this mechanical slip.

Next the current measurements was calibrated. The first step in this process was to check if all currents were symmetrical. Which they were. If this had not been the case then the calibration could not continue as there would be something seriously wrong with the electrical system. The second step was to check the controller current measurements while the inverter was not operating, thus zero current. Initially these measured values did not show zero. Every current measurement device is unique due to internal and external electromagnetic conditions. Thus the current measurements has to be accurately and individually calibrated once they are used in the designated place and condition. This was done now for the test rig, but it also had to be done when the circuit boards was placed inside the vehicles. The last step was checking the accuracy of the filtered phase current rms measurement during operation. The difference between the oscilloscope measurement and the controller measurement was 0.3 amperes. Which is good enough for motor controller purposes. It should be mentioned that the oscilloscope peak to peak measurement was not very precise as there was a lot of electromagnetic noise.

8.8 CAN bus test

As the torque reference of the system would be set by an external FPGA it had to be tested.

Test:
CAN bus test.

Measured:
Motor controller status codes and torque reference
2011 axial flux motor no load rotation speed.

Equipment:
Test rig as described in part 8.4.
External FPGA, with joystick, controller connected to Virtex 5 FPGA module via CAN bus.

Result:
The external FPGA was able to control the Vertex 5 FPGA torque reference. The system acted the same way as it does when a torque reference was set by the screen module.

08.04.2014

Knowing that the system was controlled easily through CAN bus allowed further development of the external FPGA software without having to worry about communication problems.

8.9 Initial inverter circuit board testing

As soon as the first inverter circuit board was ready the initial testing started in order to identify possible design or production errors early. The resulting fixes found after these tests were performed are described in detail in the inverter circuit board documentation: [37]. The thesis work involving these tests was mainly to observe, assist and produce the heat sink configuration including other necessary parts.

Test:
Initial inverter circuit board testing.

Measured:
Observing circuit board status indications.
Input DC voltages and currents.
Internal voltage signals on the circuit board.

Equipment:
Circuit board made for inverter testing (illustrated in figure 8.9.2).
Inverter circuit board. MOSFET: STB75NF75.
DC power source.
Oscilloscope with voltage measuring probes.

Result:
The inverter worked well except for two features:

When inverter drive circuit supply power was applied the "OK" signal was the first one to trigger. See figure 8.9.1. This was not correct as the "Fault" signal should have triggered first which would have indicated that the supply voltage was too low.

The voltage measurement output did not have the correct output. Something seemed to be wrong with the measurement circuit even though the IC involved behaved as it should.

09.04.2014

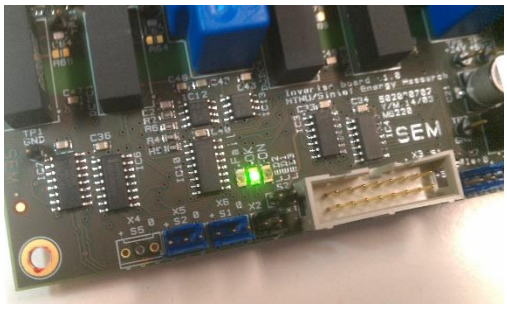

Figure 8.9.1: Inverter circuit board initial "OK" signal fault illustration

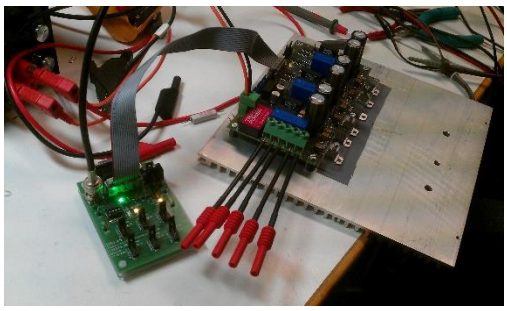

Figure 8.9.2: Inverter circuit board connected to a test circuit

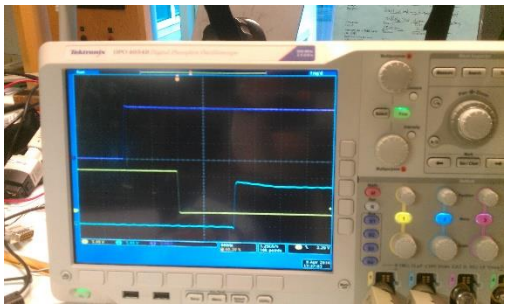

Figure 8.9.3: Inverter circuit board pulse signal test illustration

The status signal fault proved to be a fault in the circuit design. It was easily fixed by switching the conducting paths to the "OK" LED and the "Failure" LED component. The voltage measurement failure was due to a miscalculation which led to wrong values for some of the resistances in the circuit. It was fixed by switching these resistances with other resistances with correct values.

The last inverter circuit board feature that had to be tested after the initial testing was done was the PTC thermistor which is supposed to trip the system when overheating occurs.

Test:
Heat sink temperature tripping test.

Measured:
Heat sink temperature.

Equipment:
FLUKE thermometer, N02-0128.
Electric griddle.
Inverter circuit board. MOSFET: STB75NF75.
DC power supply.

Result:
When the heat sink temperature reached 103 ^{o}C the system tripped and the circuit board status indicator went from “OK” to “Fault”.

07.04.2014

Figure 8.9.4: Heat sink temperature tripping test 28.7˚C, circuit has not tripped

Figure 8.9.5: Heat sink temperature tripping test 104.4˚C, circuit has tripped

The overheat tripping proved to be working as the circuit tripped at an acceptable temperature. A bit lower tripping temperature would have been preferable though.

8.10 Encoder tests

8.10.1 EM1 with DISC-2 solution test for the AXI and the EC 60 flat motor

Some early testing was done in order to see if it would work to use the EM1 in combination with DISC-2 solution, part 6.2.2, for the available prototype vehicle motors.

Test:
EM1 with DISC-2 prototype vehicle encoder system testing.

Measured:
Observing motor behaviour when torque is applied.

Equipment:
AXI motor.
EC 60 flat motor.
3D printed encoder mounts for both motors.
EM1 and DISC-2.
Electrical part of test rig as in part 8.4.3.

Result:
Despite several attempts with both motors a reliable motor behaviour, when it came to spinning constantly while torque was applied, was never achieved. Although the AXI motor encoder solution had a few reliable runs before the disc became defect.

07.04.2014

Figure 8.10.1: AXI and EC 60 flat motor with 3D printed plastic mounts for the EM1 encoder

It should be noted that this test was done before the index pulse problem, part 6.2.2, was solved. This means that the results would never have been fully reliable even if the EM1 and DISC-2 was perfectly aligned and not defect.

What was learned from this test was that it was hard to get the EM1 and DISC-2 to work perfectly together and that the disc very easily became defect. This lead to, among other observations made, that the S1 encoder solution development started for the prototype vehicle motor. See part 6.3.2 and the next test in part 8.10.2.

8.10.2 Urban concept vehicle encoder solution development tests

Finding a reliable encoder solution for the urban concept vehicle was probably the most frustrating part of this project. The tests that involved the development process leading to the final solution is described here. It was during these tests that the index pulse fault was found. For more info about most of the aspects presented here see chapter 6.

Test:
Urban vehicle encoder solution development tests.

Measured:
Observed urban concept vehicle motor/wheel behaviour.

Equipment:
2011 axial flux motor as the back right wheel of the urban vehicle.
EM1 and DISC-2.
S1 encoder.
ROD 420 encoder.
Test rig motor axle adapter part.
Plastic cup.
Oscilloscope with current measurement device.
Inverter circuit board. MOSFET: STB75NF75.
SINTEF FPGA module.
FPGA power supply.
DC source.

Result:
A lot of different things was tried out were most of the attempts led in the wrong direction. The test description will focus on the few tests that lead in the right direction.

It was assumed initially that the EM1 with DISC-2 solution would be the final solution for the urban vehicle even though the electrical system was very unreliable last year: [12]. Figure 8.10.2.1 illustrates the solution mounted on the wheel. The EM1 encoder had to be adjusted perfectly over the disc in order to get smooth spinning, but even when this was done it kept going in a random direction when the system was turned off then on again.

A similar test was performed with the S1 encoder and a plastic cup acting as a rotating axle: Figure 8.10.2.2. It gave the same result as a perfectly positioned EM1. The motor kept changing direction

Figure 8.10.2.1: EM1 with DISC-2 testing

Figure 8.10.2.2: S1 taped to wheel with plastic cup testing

Figure 8.10.2.3: ROD 420 taped to test rig motor axle adapter testing

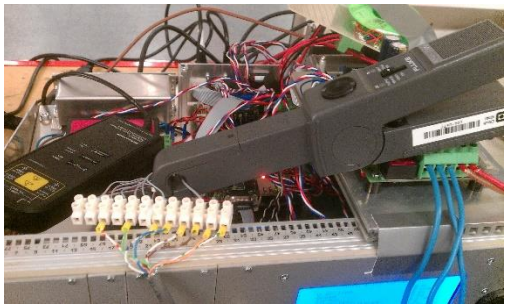

Figure 8.10.2.4: Current measurement connection on the index channel (I+)

randomly after resetting the system.

As there was so much problems with the US Digital encoders, which never happened on the test rig, a similar test as the one done with the S1 encoder was tried with the ROD 420 encoder. See figure 8.10.2.3. The random spin direction after reset problem never occurred with this setup.

It was suspected that the index pulse, provided by the US Digital encoders, was never registered by the FPGA. The FPGA has a LED indicating pulses for each channel (A, B and I). It was also tried to find the index pulse with an oscilloscope, but this did not work as there was too much noise. While rotating the S1 encoder manually the point when the index channel LED pulse trigger was found as illustrated in figure 8.10.2.6. This initially led to the conclusion that the FPGA did register the index pulse, but this conclusion was faulty. It was eventually found out that there was something wrong with how the FPGA registered the index pulse by comparing the ROD 420 and the EM1 pulse signal diagrams. It was fixed by inverting the A and B channel signals. See part 6.2.2.

After the index pulse problem was solved S1 encoder mounts were developed. The first design did not take into consideration that the EM1 with DISC-2 mount also acted as a nut which held the stationary part in place. This led to a continuously changing stator position as the stator slipped inside. This was fixed by creating a new S1 encoder mount which allowed a nut to be screwed tight on the stationary axle before being glued on the outside on the rotating part.

Figure 8.10.2.5: Channel A- pulse train testing with oscilloscope

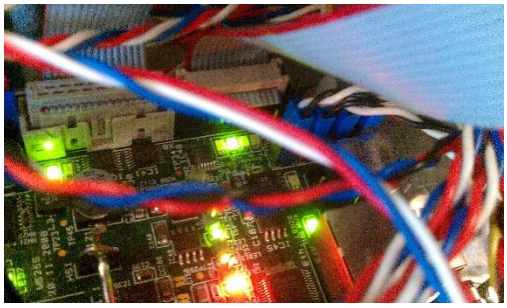

Figure 8.10.2.6: FPGA encoder channel LED illustration with Z (index) pulse triggered

Figure 8.10.2.7: S1 connected first encoder mount design without nut

26.04.2014

These tests had finally led to an urban vehicle encoder solution which actually worked, but there was still some concern regarding the stator slipping. Sudden change in stator position so that the stator position offset parameter had to be tuned again had already happened on numerous occasions earlier while operating the test rig. Especially when applying sudden and large torque references. Not much attention was given to the problem at that time because not enough experience with the FPGA module had been achieved yet. Stator slip

could have been the issue that eventually would lead to an encoder malfunction during the last two urban concept SEM 2014 attempts: List 9.5.1.

8.10.3 Prototype vehicle encoder test

Part 6.3.2 describes the two encoder mounts made for the prototype vehicle. The test described here uses the first encoder mount design as the final design would not be made without proof of that the first one was working, which also is the purpose of this test.

Test:
First prototype vehicle encoder mount design test.

Measured:
AXI motor behaviour with torque applied.
Temperature by touch.

Equipment:
AXI motor.
First prototype vehicle encoder mount made. See figure 6.3.2.1.
S1 encoder.
Inverter circuit board. MOSFET: STB75NF75.
SINTEF FPGA module.
FPGA power supply.
DC source.

Result:
Was able to tune the stator position perfectly straight away. Very reliable operation, even after several system resets.

Required a large torque (about 500 pu) to start spinning because of cogging.

Even though the motor was spinning at no load it became warm fast. The FPGA power supply became very warm.

29.04.2014

As the motor was operated very reliably with this encoder mount solution a new and upgraded mount based on the same design could be made. The large required starting torque was expected and would not be a problem. The heat was a problem though. Cooling capability became an important factor for the next design because of this observation.

The FPGA power supply heat observation indicates that this part is not efficient enough.

8.11 Full system testing in vehicle with driver

As soon as the vehicle worked properly while on the vehicle rig it was time to put it on the ground with a driver to test.

Test:
First urban vehicle full system test including screen.

Measured:
Vehicle acceleration and reliability.

Equipment:
Final urban concept vehicle system as in part 9.1.
SINTEF FPGA screen.

Result:
The vehicle was operated with the screen as illustrated in figures 8.11.1-2.

The first issue that was encountered was the vertical position of the motor relatively to the vehicle monocoque changed when it was put on the ground and even more when a driver sat inside. At the time it was only the encoder cable that held the stationary part of the S1 encoder in the same position, so when the vertical position changed so did the position of the S1 encoder. This was fixed by creating a vertical fork that did not let the encoder position to change, but allowed it to move vertically. See part 6.3.1 for more information on this subject.

After the encoder issue was fixed the urban vehicle still did not behave as desired. The torque provided by the motor was so weak that it did not even manage to start rolling the vehicle with a driver inside. Eventually the root to the problem was found. Three jumpers was needed on the FPGA circuit board in order to achieve correct current measurements. See figure 8.11.3 and part 5.4. The motordrive simply thought that it was giving more current than it was actually providing. After these jumpers was placed the vehicle was operated perfectly, both with the screen menu and by CAN bus, with good acceleration.

06.05.2014

Figure 8.11.1: First urban vehicle full system driving test including screen

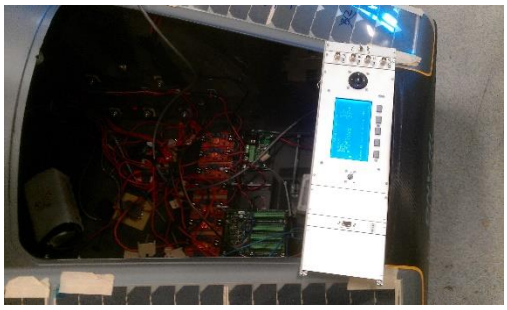

Figure 8.11.2: Urban vehicle driving test with screen, screen mount illustration

Figure 8.11.3: The three critical jumper connections on the FPGA for correct current measurement

The result of the previous testing presented was a fully driveable urban vehicle. As the acceleration problem was fixed with jumpers this was easily done for the prototype vehicle as well. As soon as the full mechanical and electrical systems was ready for both vehicles it was time to increase the testing scale. This was done by moving the vehicles to an ice skating track, which did not have any ice at the time as it was spring, in order to find out if the vehicles could handle the speed required.

Test:
On track full system with driver testing for both the prototype and the urban concept vehicle.

Measured:
Vehicle speed provided to driver by CAN bus and driver interface screen module.
Temperatures measured after each drive by touch.
DC voltage levels.

Equipment:
Both vehicles with final system as in part 9.1, except for the newest AXI encoder mount and gear parts.
FLUKE multimeter.
Laptop with serial port cable for activating and deactivating the SINTEF FPGA screen.
SINTEF FPGA screen for tuning (disconnected while driving).

Result:
As the vehicles had not been taken outside with the full system connected yet so far an unforeseen problem revealed itself. The MPPTs (maximum power point trackers), which adjusts how the power is provided to the battery for maximum output, was initially tuned to provide a way too high voltage. The motor controller system of the urban vehicle was reset as soon as it came on as the maximum DC voltage parameter of the motordrive triggered. It was measured by multimeter to be over 60V. The person responsible for the solar system was not there at the time so the solar cells was just disconnected from the system.

Another problem that soon occurred as the vehicles started to move was that there was too much noise on in the messaging system between the joystick, which is used to provide torque, and the rest of the system. Making the system very hard to operate for the driver as noise made the torque reference reset

Figure 8.11.4: Driver getting into the prototype vehicle for its first test on a track

Figure 8.11.5: Both vehicles ready for racing on ice skating track

Figure 8.11.6: Late evening GPS problem investigation after track test

very frequently. The main goal of this test was to see if the driver could get the vehicles up to 30 km/h. In order to achieve this the drivers was told to try to require maximum torque often in order to override the noise. This worked as both vehicles managed to reach 30 km/h.

As the first design of the AXI motor encoder mount, part 6.3.2, was still in use at the time there was some concern that the motor would become too hot during the test, but the motor was tepid after each run.

At the end of the day a lot of dust from the road had accumulated on the electrical system of the prototype vehicle.

The GPS module of the vehicle was also tested, but it did not work properly yet.

09.05.2014

Figure 8.11.7: Late night further EMI problem solving

The test was very successful when it came to the electrical parts involving this thesis. It managed to accelerate the vehicles to 30 km/h and the AXI motor did not become too hot. Unfortunately there was still some problems with the other parts of the system which this system depends on. The noise on the joystick module was a huge problem, but luckily it was solved later that night, by the cybernetics part of the team, by introducing a couple of filters in the software to remove the influence of electromagnetic noise. Two other critical problems was not solved before both vehicles was shipped for Rotterdam: The solar cell system for both vehicles still provided a voltage which was too high and the GPS did not work properly for reading vehicle position and speed. One last issue discovered that day was that there was a lot of dust on the electrical prototype vehicle system, which had been brought into the vehicle by the back wheel. These problems would have to be solved during the first days at SEM 2014.

Chapter 9: Final electric propulsion system solutions, modifications, events and competition results

This chapter describes the final electric propulsion systems used in the vehicles. This chapter also includes all of the important events of Shell Eco-Marathon 2014, including the final results for both vehicles. The official competition date was from the 15th to the 18th of May, but the technical part of the DNV GL Fuel Fighter team arrived in Rotterdam at 12th of May. These three extra days was used for team registration, fixing remaining issues, passing technical inspection and test driving on the competition track.

9.1 Final electrical system used for SEM 2014 description and illustrations

The final electrical system is illustrated in figure 9.1.1. Note that only the parts relevant for this thesis is displayed. It is a detailed description of the system as it was set up before leaving for Rotterdam. A less detailed version of it was previously presented in part 2.6.1.

The diagram is identical for both vehicles, but the total system is not. What is different between the two final vehicle systems are the encoder mounts and adapters, described in parts 6.3-4, and how the circuit boards are placed in the vehicles. A few minor changes was made to the system during SEM 2014. This is described in parts 9.3-4. Three full sets of this system was made. One for each vehicle and one spare system in case one of the systems used would stop working.

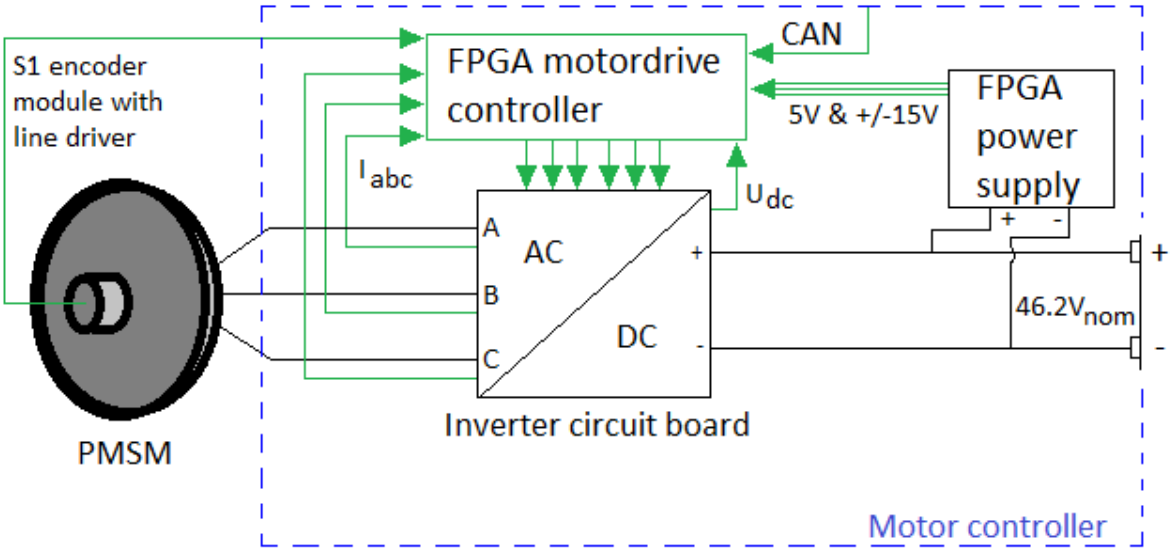

Figure 9.1.1: Final electrical system diagram for both vehicles

For more information about each of these sub components see their respective chapters. Figure 9.1.2 illustrates how the circuit boards are connected in the back of the urban concept vehicle. They were fixed to the surface by the use of Velcro.

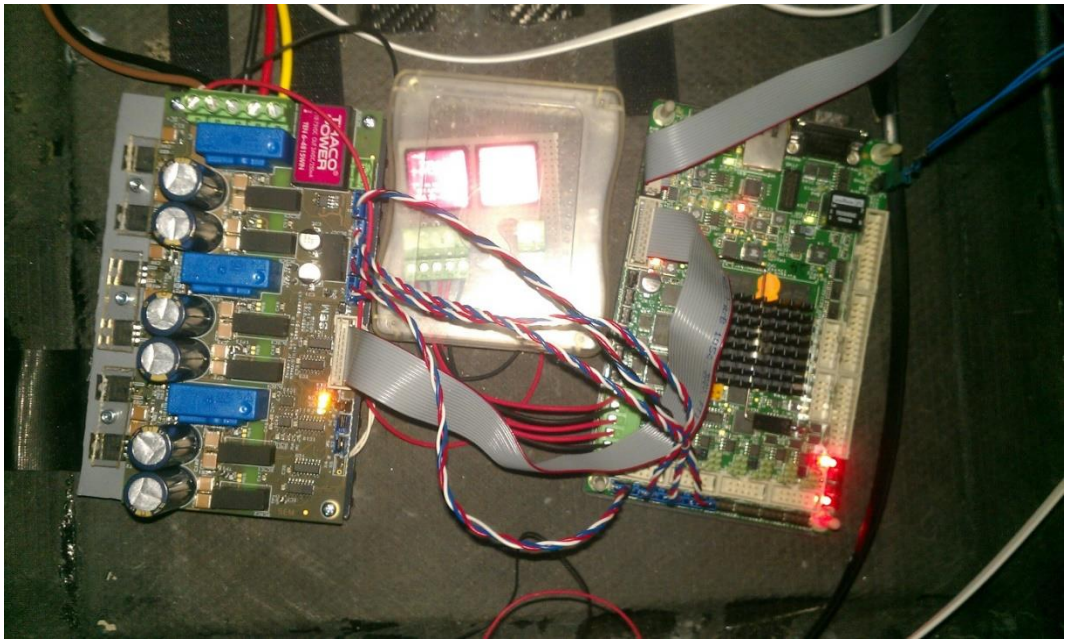

Figure 9.1.2: Final electrical system illustration: Urban concept vehicle

In the prototype vehicle there was a much less space for the electrical system. Figure 9.1.3 illustrates the final solution. The propulsion battery was strapped at the bottom and two transparent shelves along with the wall was left for the rest of the electrical system. The relevant thesis part of the system is barely visible in the picture at the middle of the lower shelf. The open space in the middle of the top shelf was for the joulemeters mentioned in part 2.2.1. Inverter board number 1 was used in the urban concept vehicle and number 2 was used in the prototype vehicle. The MOSFET type used is different for these two boards. See part 4.3.6.

Figure 9.1.3: Final electrical system illustration: Prototype vehicle

It is possible to spot in figure 9.1.3 that the newest encoder mount was in place before sending the prototype vehicle racing on the Rotterdam track, but it is not the only new thing that was in place. As the AXI motor seemed to be reducing the rolling capability of the prototype vehicle, part 3.4.1.2, a new gear solution was developed. The part of the gear mounted on the rotor of the AXI motor was now slipping as soon as the wheel was rotating faster than the gear equivalent motor rotation speed. This way the AXI motor could now only provide force in the forward direction. This feature would prove to be very favourable as the new driving strategy was developed during the SEM 2014 test driving process described in part 9.3. Another new thing that was in place was a back wheel carbon fibre mudguard which was there to prevent external elements like moisture from short-circuiting the electrical system. It is also visible in figure 9.1.3. It was implemented because of the dust observation made in part 8.11.

9.2 Technical inspection

In order to use the track in Rotterdam the vehicle had to pass technical inspection first. In order for the electrical system to pass a technical inspector had to validate the system according to the competition rules. These rules have previously been discussed in part 2.2.2.

Figure 9.2.1: View at SEM 2014 Technical Inspection

Figure 9.2.2: Electrical system being checked by SEM 2014 technical inspector

There was some concern prior to the technical inspection as SINTEF software was used which was not purpose-made for SEM 2014. All of the technical documentation for the electrical system was brought to the inspection along with the e-mail which confirmed the motor controller solution used. This e-mail is found in appendix F.

Both of the electrical systems ended up having no problems getting through technical inspection. The technical inspectors was actually very impressed with the electrical system (especially when the fancy blue LED arrangement in the back of the prototype vehicle was turned on). They also said that it was more than purpose-made enough for the competition.

After some minor mechanical fixes on both vehicles they passed technical inspection and the test driving could begin.

9.3 Test drives on Rotterdam track, issues and new solutions

As the prototype vehicle's first AXI motor was replaced with the other identical motor having the new encoder mount and gear solution the stator position offset parameter had to be tuned again. Unfortunately it was not possible to do with the system inside the vehicle as the screen used for tuning picked up too much electromagnetic noise. It was solved by using the third system made outside of the vehicle for tuning, figure 9.3.1. It was tuned with reversed position sensor direction as the wheel would not turn with the motor this way with the new gear solution. As soon as the perfect stator position offset was found with the external system, the parameter was mirrored over to the system inside the vehicle. This was done at the end of each day to ensure that the system was still perfectly tuned. The position changed about 0.7° during the whole period spent in Rotterdam. This change so small that it is almost negligible. It could just as likely have been caused by some inaccuracy in the tuning process rather than change in the actual encoder position.

Figure 9.3.1: Tuning process of prototype vehicle using third system externally

Figure 9.3.2: Tuning urban concept vehicle while on ground with driver inside

Tuning the urban concept vehicle stator position offset was a different story. The vertical fork was not completely vertical which lead to a small change in encoder position as soon as someone sat inside the vehicle. It was decided to tune the vehicle with a driver inside. This was done by running behind the vehicle with the tuning screen. See figure 9.3.2. Hardly an optimal solution, but it worked. Encoder problems happened more and more frequently as the days went by so this procedure had to be done a lot of times. The encoder issues will be described later in this chapter.

With two perfectly tuned and operational vehicles it was time for test driving them on the Rotterdam track. Most of the previous DNV GL Fuel Fighter teams never had the system ready in time for making test runs. Having the opportunity to make practice runs is very important. Not only for testing the system, but for letting the drivers gain experience with driving the vehicle on the track. An experienced driver knows how to operate the system properly and also knows when to accelerate and for how long. Using the small, but existing, variations in altitude on the track the driver could roll without using the motor for long periods of time.

By paying attention to the joulemeters it was discovered that the standby power consumption of the system was high. About 15W. By communicating with competitors it was discovered that many of them had a system standby power consumption at about 2W. This issue had to be dealt with in order to achieve good results in the competition. Especially for the prototype vehicle were 15W is a substantial amount of the average power used for an attempt in that class. The best prototype vehicle the year before had an average power consumption of about 25W.

It was decided after the first day of testing that the driver must be able to turn off the electric propulsion system while rolling in order to reduce the standby losses. This was done by allowing the driver to choose between two modes while driving: Manual or automatic acceleration. When in manual the driver could accelerate and decelerate freely. When in automatic and pushing the joystick down the electric propulsion system, figure 9.1.1, was shut down by disconnecting the propulsion battery and when pushing up the battery was reconnected, the system started up again and 1000pu torque reference was applied. See [49] for more information on the driver interface system.

For the urban concept vehicle system another switch which disconnected the FPGA power supply, at the same time as the battery was disconnected, had to be implemented. This had to be done because the spinning motor/wheel would induce a voltage and provide power to the FPGA without this switch. This was not a problem in the prototype vehicle system as the wheel was spinning freely even though the motor was standing still because of the gear solution mentioned in part 9.1 and 3.4.1.2. There was some concern that the prototype vehicle motor would not start at some point as it always started from standstill without the index pulse triggered. Luckily this never occurred. Probably because the motor, regardless of the initial direction of the rotation, always would start with no load, as long as the wheel was spinning.

A problem that occurred when shutting down the propulsion related system was that the driver lost the speed reading provided by it. This was solved by letting the GPS, which was now working properly, provide the speed of the vehicle while the electric propulsion system was shut down.

Figure 9.3.3: First test run with the prototype vehicle

After implementing the electric propulsion system shut down feature at the end of the first on track testing day it was time to test it at the second day. The prototype vehicle electric propulsion system continued to work as reliably as it always had. The problems that occurred was due to the driver not understanding the new driver interface system, along with some other issues like heat and the driver interface screen falling down. These problems was solved by letting the drivers learn the new system, adding another fan and applying a better fixing for the driver interface screen. The urban concept vehicle, on the other hand, had some issues related to the electric propulsion system. When shutting the system off then on again it would sometimes just stop working. The reason why is uncertain as it suddenly worked properly again when taken inside. It was decided to not use the shutdown function on the first urban concept class competition attempt as it did not work properly yet. This was not a huge problem as the standby power consumption is a much smaller part of the total loss for the urban concept than the prototype class as the vehicles has to stop then accelerate again for each lap in this class as mentioned in part 2.2.1.

A great safety advantage introduced by the SINTEF FPGA motordrive was the max speed limiter which was mentioned in list 5.5.1. Many teams did not have this motor controller feature and some of them even rolled over and crashed while making a turn because of it.

The solar issue mentioned in part 8.11 had to be fixed before the official competition attempts started. For the urban concept vehicle this was fixed just by tuning the MPPTs properly for a lower voltage output. For the prototype vehicle solar system it was more complicated, as each row in the solar cell system had one cell too much. The MPPTs could not be tuned low enough to achieve lower than 60V because of this design flaw. It was solved by using the third (spare) FPGA power supply circuit, part 5.3, to reduce the voltage output from one of the two MPPTs in the solar system to 15V. By then connecting the two MPPT outputs in series the needed 49V solar power output was achieved after proper MPPT tuning.

9.4 SEM 2014 attempts and results

The prototype vehicle had gained so much attention that it was chosen, along with 9 other teams, to be in the SEM 2014 opening ceremony. This also allowed the vehicle to be the first prototype vehicle out on the track for its first official competition attempt. Unfortunately the vehicle had some front brake issues which prevented it from racing. These brake issues were solved in a bike shop early the next day, in time for the next prototype class runs.

Figure 9.4.1: SEM 2014 opening ceremony PHOTO: SHELL

Because of the prototype vehicle break issues the urban concept vehicle was actually the first of the two to get a valid attempt. The vehicle was operated safely by the driver at manual mode all the way through which led to a temporary 2nd place when finished. The official end results are presented in list 9.4.1, appendix G and online [9]. Another team had a better result later that day which pushed the urban vehicle result down to a 3rd place. The urban concept vehicle driver reported a weak acceleration after the first attempt which could mean that the system was not perfectly tuned. It was not far up to the 2nd place (198.7 km/kWh versus their 202.7 km/kWh result) so the team was confident that the 2nd place would be taken back on one of the next attempts. For that a better tuned system and driving strategy was needed. Mechanical breaks was used sometimes instead of regenerative breaking because the speed was too high when coming close to the urban concept stop line.

Figure 9.4.2: Urban concept vehicle during the 1st valid attempt PHOTO: SHELL

Later that day it was time to try to take back the 2nd place in the urban concept class. A couple of hours, while the prototype vehicle was racing, had been spent just prior to the attempt just on tuning the system perfectly. As the attempt started the driver reported a much better acceleration and everything was going towards a much better result. Unfortunately the door lock suddenly malfunctioned and the door slammed open (the door hinges are on the opposite side to that of a regular vehicle door). As the driver had no chance to shut the door in time it was spotted by the track officers and the vehicle was escorted out of the track.

After the door incident attempt the reliability of the electric propulsion system in the urban vehicle started to rapidly decline during testing. There seemed to be something very wrong with the encoder system. The stator position offset parameter had to be changed frequently. As time was of the essence at this point the urban vehicle was rushed back to the track as soon as the system seemed to be working reliably again. Unfortunately the first attempt that final day ended with an urban vehicle not being able to start rolling at the starting line. The problem still seemed to be related to the encoder system. Only 15 minutes was left to fix the problem before the last run. In this time both the S1 encoder and the encoder cable was replaced with spare parts and the system was tuned one last time. At the last attempt the vehicle actually managed to start rolling, but after completing almost one lap the message 03 was displayed on the driver interface screen and the vehicle stopped. Message 03 meant that the encoder cable and the encoder was separated and also meant the end of SEM 2014 for the urban concept vehicle. In the rush of fixing the problem in 15 minutes the tape holding the cable and the encoder together was unfortunately forgotten. The driver also reported a very weak acceleration this time so the result would most likely not increase even if a valid attempt had been achieved. The end result for the urban concept vehicle was a 3rd place which the team was very happy with despite the possible improvement potential.

After fixing the breaks the first attempt with the prototype vehicle was also a valid one. It lead to a 6th place at the time which jumped down to a 13th place later. This was not a very good attempt. The system was operated in automatic mode, but the driver reported that the electric propulsion system frequently did not provide torque and that the message 75 kept being displayed while this happened. Message 75 is a fault message indicating that there was something wrong with the blocking connection X6 of the inverter, see list 4.4.1, which blocks inverter circuit operation while the battery is disconnected. This was most likely caused by a loose wire in the relay system connected to X6. At the end of the day the X6 relay system was replaced by a jumper between pin 1 and 2 hoping that this would solve the problem. There was some risk doing this as the inverter could be damaged by a large voltage pulse this way. This was an acceptable risk as inverter circuit board number three was available and operational.

Luckily the inverter did not get damaged at any of the attempts performed the next and final day of the competition. At the first attempt the driver reported a fully functioning electrical system, but when the attempt was finished it was discovered that the solar cells had far from provided enough power to cover the 20% of the propulsion losses. See part 2.2.1. This happened because the MPPTs was tuned early that day and the sun angle had changed a lot while in queue and during the race. Despite of this the result still increased from 512.4 km/kWh to 516.5 km/kWh.

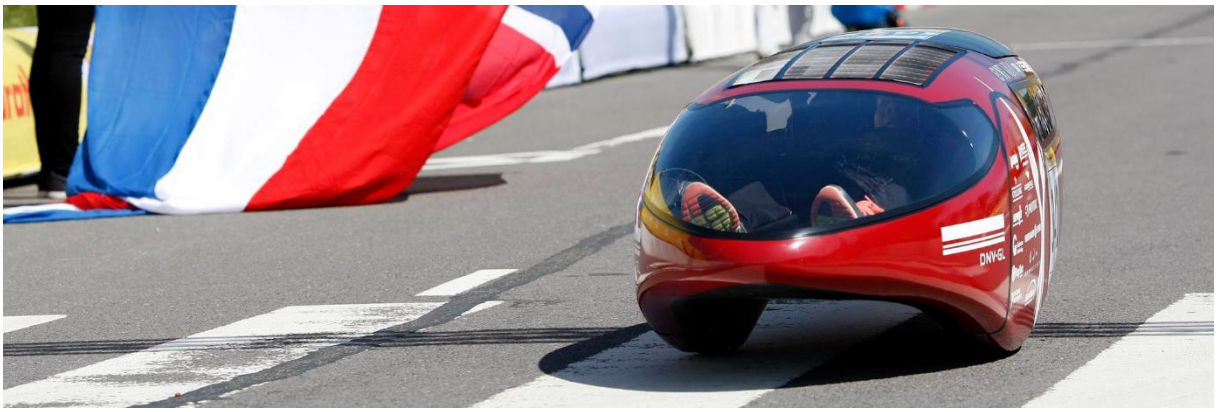

Figure 9.4.3: Prototype vehicle driving during SEM 2014 opening ceremony PHOTO: SHELL

There was still enough time for one more prototype class attempt after the second one. This time the MPPTs was tuned right before entering the start registration tent and it was later in the day so that the sun intensity did not change as much. Also during this attempt the prototype vehicle system was functioning perfectly and the driver finished the 10 laps only seconds before the 39 minutes limit. The result was a stunning 612.8 km/kWh which resulted in a 7th place. The team was extremely happy with the result. List 9.4.1 is a summation of the final SEM 2014 results for both vehicles with a comment for each attempt:

Final Results SEM 15.-18. May 2014 in Rotterdam			
Prototype class: 7th place		**UrbanConcept class: 3rd place**	
Result	*Comment*	*Result*	*Comment*
not valid	Front brake malfunction.	198.7 km/kWh	Tuning and driving issue.
512.4 km/kWh	Message 75 issue.	not valid	Door malfunction.
516.5 km/kWh	Solar power issue.	not valid	Encoder issue.
612.8 km/kWh	Perfect run.	not valid	Message 03 issue.

List 9.4.1: Final SEM 2014 results and comments

9.5 SEM 2014 final results discussion

List 9.4.1 shows the final results in the competition. The DNV GL Fuel Fighter 2014 team results will now be discussed for both cars.

The prototype class 7th place and the urban concept class 3rd place are not really that far apart, as there were more competitors in the prototype class. There were 28 competitors which managed to get at least one valid competition attempt in the prototype class. In the urban concept class this number was 15. Keep in mind that there were more competitors in the different classes than these numbers imply, as many of them did not manage to get a valid competition attempt.

Some issues occurred when the racing started for the prototype vehicle, but after these minor issues were solved it had a perfect run. Except for the message 75, loose wire, issue the electric propulsion system in the prototype vehicle was very reliable the whole competition period.

The urban concept electric propulsion system required a lot more attention though. All of the main issues that occurred were related to the encoder part of the system. What part of the encoder system that was faulty is still unclear, but it is most likely one out of three possible issues that have been mentioned frequently in this thesis:

1. The stator slip issue, described in part 3.3.1.1 and 8.10.2, should be investigated further. When this problem occurred during testing the behaviour of the motor controller system was very similar to what happened during the competition.
2. Another issue that could have triggered the same motor controller behaviour, would be an encoder index channel malfunction. The S1 encoder, part 6.2.2, had been through a lot of rough treatment at this point. If the S1 rotor had been bent by the friction force while sliding on the vertical fork, the disc inside the encoder module could also be misaligned with the encoder.
3. It should also be noted that the less reliable test rig encoder adapter, figure 6.4.1, was used in this vehicle. The problem could have been caused by a loose wire in this adapter.

List 9.5.1: Possible issues that could have led to the urban concept vehicle encoder problems during the competition

As the motor and the encoder system are the only parts of the total electric propulsion system that are different between the two cars, it seems reasonable to assume that the motor controller parts, inverter and FPGA, were functioning perfectly.

By analysing the data from the competition results it is easy to see that a rather efficient electric propulsion system has been made for both vehicles. The prototype vehicle would be able to drive 612.18 km on one kWh unit (assuming that the vehicle would have to stop once

every 16.117 km and that solar power could only provide 20% of propulsion consumption). The gasoline gallon equivalent (GGE) base is 33.41 kWh/US Gal. [57]

$$612.8\frac{km}{kWh} * 33.41\frac{kWh}{US\ Gal} * 0.264172\frac{US\ Gal}{l} = 5\ 408.6\frac{km}{l} \quad (9.5.1)$$

Equation 9.5.1 shows that prototype vehicle would be able to drive 5408.6 km on one gasoline litre equivalent unit. For comparison: Driving from Oslo to Baghdad is a travel length of 5315 km [58].

In order to analyse the urban concept vehicle result it may be compared with the urban concept result achieved during SEM 2013. The final urban concept vehicle result was 198.7 km/kWh. In 2013, with almost the same vehicle, mechanically speaking, the result was 201.9 km/kWh [12]. Just by comparing the numbers it may seem that the vehicle did better in 2013, but the solar power does also have to be taken into account. The solar panels on the urban concept vehicle are very large and expensive. Probably the solar panel system in the competition which contributed with the highest amount of power, both in 2013 and 2014. The difference between 2013 and 2014 was the new rule that the solar panels may only contribute with an amount of power which covers 20% of the total propulsion consumption. See part 2.2.1. Thus in order to compare the results the contribution from solar panels has to be subtracted from the results. The solar panels managed to cover more than the 20% limit of the propulsion system consumption in 2014. In 2013 the solar panels contributed with 124677 joules [12] during the valid urban concept competition attempt.

2014 urban concept class result without solar power contribution:

$$\frac{16.117\ km}{198.7\frac{km}{kWh}} = 0.08111222949\ kWh \quad (9.5.2)$$

$$0.08111222949\ kWh * (1 + 0.2) = 0.09733467539\ kWh \quad (9.5.3)$$

$$\frac{16.117\ km}{0.09733467539\ kWh} = 165.58\frac{km}{kWh} \quad (9.5.4)$$

2013 urban concept class result without solar power contribution:

$$\frac{16.117\ km}{201.9\frac{km}{kWh}} + 124677\ J * \frac{1}{3600000}\frac{kWh}{J} = 0.0798266\ kWh + 0.0346325\ kWh \quad (9.5.5)$$
$$= 0.1144591469\ kWh$$

$$\frac{16.117\ km}{0.1144591469\ kWh} = 140.81\frac{km}{kWh} \quad (9.5.6)$$

By removing the solar power contribution from the urban concept vehicle result for both years, the 2014 result is actually the best one (165.58 km/kWh versus 140.81 km/kWh). This was judged to be very impressing considering that a brand new purpose-built motor controller and a probably less efficient axial flux motor was used.

The results achieved by the DNV GL Fuel Fighter 2014 team is definitely something to be proud of. Most of the competitors that had better results had been in the competition for several years already, with the same vehicle and the same team. Some of them were not even pure student teams. Some teams seemed to consist of professors who made most of the mechanical and electrical system, including some teenagers who did less technical tasks.

Previous DNV GL Fuel Fighter teams only had one vehicle to worry about for the competition. This year a new vehicle was built from scratch, while doing enough work with the old vehicle to get that through technical inspection as well. Technical inspection was even passed quickly enough to test drive both vehicles properly on the track with driver before the actual competition started. More experienced drivers was clearly an advantage during SEM 2014. Carrying out valid attempts, with good results, for both vehicles was an even greater achievement.

Chapter 10: Conclusions and further work

10.1: Conclusions

The main task of this thesis has been to assist the DNV GL Fuel Fighter team in the planning, design and building process of the electric drivetrains for the urban concept and the prototype vehicle. This task was successfully accomplished with the work and results presented in this thesis.

The electric propulsion system became of main interest, as other team members would be able to take care of the other parts of the electric drivetrain. It was decided to divide the electric propulsion system into four main sub systems: The electric motor, inverter, controller and encoder. Conclusions for each of these parts will be presented in the next sections.

Two electric motors was available for the prototype vehicle: The EC 60 flat motor and the AXI motor. Both were of the type PMSM. As the EC 60 flat motor had low power rating, a simulation model was developed early in order to find out if it could withstand the loads. The simulation test concluded that the EC 60 flat motor would not be strong enough for the purpose of accelerating the vehicle. The simulation test was confirmed by a motor malfunction when the EC 60 flat motor was used on the motor test rig. The AXI motor was not discovered before the above alarming simulation results were produced. This motor was functioning really well, but the cogging was an issue as it introduced vibrations and a high required starting torque. Rolling capability of the prototype vehicle was reduced when the AXI motor was connected to the back wheel. A special gear was implemented in order to counter this effect. The efficiency of the AXI motor is not especially good.

Two electric motors was available for the urban concept vehicle as well. One axial flux motor made in 2011 and another one made in 2013. Tests done by previous DNV GL Fuel Fighter teams concluded that the 2013 axial flux motor was much more efficient than the 2011 axial flux motor, 97% versus 90% efficiency during optimal operation, but the 2013 axial flux motor broke already at the start of the 2014 semester. It was decided that the 2011 axial flux motor would have to be used for SEM 2014, as the 2013 axial flux motor could not be fixed in time. An efficiency test was performed on the 2011 axial flux motor in order to find out which operating condition which would give the best efficiency. The conclusion made from this test was that the motor operated most efficient at speeds over 29 km/h. It was also concluded from this test that the efficiency of the motor was not as dependent of the torque provided as the rotation speed of the motor. The tests also indicated that a switching frequency of around 20 kHz should be used, but that tests with the final inverter circuit should be performed. This was unfortunately not done, due to an encoder fault during the last frequency test. The 2011 axial flux motor worked really well, but there seemed to be one issue. The stator seemed to slip inside the motor on several occasions, causing the tuned stator position offset parameter of the controller to become wrong.

A new requirement for SEM 2014 was that the motor controller had to be purpose-built for the competition. The motor controller solution became identical for both vehicles, except for a few software parameters. An inverter circuit board in combination with the SINTEF FPGA including an FPGA power supply circuit was used. A brand new inverter circuit board was produced for the competition. The motor controller solution worked perfectly as soon as three faults were fixed: The voltage measurement and the status indication feature of the inverter circuit board, and the menusystem_enable function of the FPGA. The motor controller solution easily passed through technical inspection as a purpose-built motor controller, but it was discovered that it had a relatively high standby power consumption. The FPGA power supply became warm fast, which makes it possible to conclude that this part was not efficient enough. Using a different FPGA, or a circuit serving the same purpose, can potentially also reduce the standby loss. It was decided to work around this problem by turning the electric propulsion part of the system off while rolling. This strategy worked well in the end for the prototype vehicle, but not for the urban concept vehicle. The reason is still unknown, but the problem was most likely related to the encoder system and not the motor controller.

During initial encoder testing the index channel signal did not get registered by the FPGA logic for the encoders delivered by US Digital. The problem proved to be a weakness in the FPGA encoder logic, which was avoided by inverting the A and B channel signal. In the end it was decided to go for the S1 encoder module for both vehicles as the EM1 with DISC-2 solution did not work properly. The DISC-2 component was quickly damaged and it was very hard to align the two parts together properly. The prototype vehicle encoder system solution worked flawlessly, except for some weight and heat issues with the first encoder mount design, which was quickly fixed in the last design. The urban concept vehicle encoder solution did not work that well. Problems related to the urban concept vehicle encoder system eventually prevented the vehicle from being able to finish the last two competition attempts. There are three possible issues which could be the cause of the urban concept vehicle encoder problems. The first possibility was the stator slip issue, as described above. The second possible issue was that the S1 encoder module could be defect due to friction forces between it and the vertical fork. The third and last possible issue was the encoder adapter used in the urban concept vehicle, which was not optimal. This was designed for the test bench and not the vehicle, so vibrations was not taken into account.

The final competition results was very good for both cars. A 3rd place for the urban concept vehicle with the result 198.7 km/kWh and a 7th place for the prototype vehicle with the result 612.8 km/kWh. The urban concept vehicle result this year was actually better than the result with the same vehicle in 2013, with solar energy taken out of the equation: 165.58 km/kWh versus 140.81 km/kWh. This was judged to be very impressing, considering that the difference between 2014 and 2013 was a brand new purpose-built motor controller, an encoder system which was not perfectly tuned and a probably less efficient axial flux motor.

10.2: Further work

List 10.2.1 contains possible improvements for the electric propulsion system, for each vehicle, in preparation for SEM 2015. The motor controller is basically identical for both vehicles and is therefore not divided for each vehicle. The list does also provide some improvement suggestions for the simulation model.

	UrbanConcept vehicle:	**Prototype vehicle:**
Electric motor:	Fix the 2013 axial flux motor and compare the efficiency with the 2011 axial flux motor, when operated in the final electric propulsion system.	Replace the AXI motor with a similar motor, only with reduced cogging and increased efficiency. A Maxon motor with higher power rating, about 300W, should give good results. Consider changing the gear configuration with something similar to a bike gear, which is what the winning team in the prototype class used in 2014.
Encoder:	Investigate the stator slip issue with the 2011 axial flux motor. Replace the encoder cable adapter with the compact type. Find a better encoder solution. A new mechanical solution for the motor with an encoder solution implemented in the design should be considered.	The encoder solution used for the prototype vehicle was working very well. There is no need to make changes to this part, unless it starts creating problems.
	Motor controller:	
Inverter:	Replace the MOSFETs on inverter circuit board number 3 with MOSFET type number 1 in list 4.3.2.2.2. This way every inverter circuit board has a different MOSFET type. By operating each inverter circuit board equally for an equal period of time the efficiency may be compared by e.g. measuring the heat sink temperature. The MOSFET type which leads to the lowest temperature at the end of the test, has the highest efficiency for that operating condition. Some work also needs to be done on tuning the gate driver circuit: Gate resistor values must be tuned to the actual power transistor type in order to obtain proper switching speed. [37] The inverter circuit board may also be redesigned. A lot of secure operation features may be sacrificed in order to improve efficiency. If the new design fails, one can always go back to using the safe inverter boards produced in thesis work.	

Controller:	The full system frequency test, which failed in this thesis, must be performed for both vehicles in order to find the optimal switching frequency of the system. Other solutions which can perform the same task as the SINTEF FPGA should be considered, in order to find a solution with a lower stand by power consumption. If a FPGA is still being used, then the FPGA power supply circuit components should be replaced with other DC/DC converters with higher efficiency. A motordrive controller algorithm which switches over to encoderless vector control during encoder faults would be preferable for the competition next year. Encoderless control is less efficient, but it is better than having an encoder fault, which leads to a system malfunction.
Simulation model:	
The simulation model may also be improved in several ways for further analysis. The decoupling terms may be implemented as well as the current sum and centre regulators. These possible controller features was described in part 5.1, 5.2.2 and 7.5.	

List 10.2.1: Recommended further work

Bibliography

[1] DNV GL Fuel Fighter; team 2014, “Master Report DNVGLFF2014,” NTNU, Trondheim, 2014.

[2] MathWorks Nordic, “MATLAB - The Language of Technical Computing,” MathWorks, [Online]. Available: http://www.mathworks.se/products/matlab/. [Accessed 10 2 2014].

[3] MathWorks Nordic, “Simulink - Simulation and Model-Based Design,” MathWorks, [Online]. Available: http://www.mathworks.se/products/simulink/. [Accessed 10 2 2014].

[4] MathWorks Nordic, “Electrical Power Systems Simulation - SimPowerSystems,” Mathworks, [Online]. Available: http://www.mathworks.se/products/simpower/. [Accessed 10 2 2014].

[5] National Instruments, “NI LabVIEW - Improving the Productivity of Engineers and Scientists,” National Instruments, [Online]. Available: http://sine.ni.com/np/app/main/p/docid/nav-104/lang/no/. [Accessed 10 2 2014].

[6] ZUKEN, “CADSTAR – Desktop PCB design for the expert | Zuken,” [Online]. Available: http://www.zuken.com/en/products/pcb-design/cadstar. [Accessed 9 June 2014].

[7] DNV GL Fuel Fighter, “DNV GL Fuel Fighter, The NTNU Eco-marathon cars,” [Online]. Available: http://www.ecomarathon.no/. [Accessed 25 May 2014].

[8] Shell Eco-Marathon, “Shell Eco-Marathon Official Rules 2014,” Shell Eco-Marathon, [Online]. Available: http://s01.static-shell.com/content/dam/shell-new/local/corporate/ecomarathon/downloads/pdf/sem-global-official-rules-chapter-1-2014.pdf. [Accessed 28 02 2014].

[9] SHELL, “Shell Eco-marathon - Shell Global,” [Online]. Available: http://www.shell.com/global/environment-society/ecomarathon.html. [Accessed 25 May 2014].

[10] SmartMotor, “SmartMotor,” [Online]. Available: http://www.smartmotor.no/. [Accessed 2014 May 26].

[11] SINTEF Energi, “SINTEF Energi AS - SINTEF,” [Online]. Available: http://www.sintef.no/SINTEF-Energi-AS/. [Accessed 28 May 2014].

[12] DNV GL Fuel Fighter; team 2013, “Master Report DNVFF2013,” NTNU, Trondheim, 2013.

[13] SHELL, “Results - Shell Global,” [Online]. Available: http://www.shell.com/global/environment-society/ecomarathon/events/europe/results.html. [Accessed 25 May 2014].

[14] E. H. Mo, “Permanent Magnet Synchronous Machines - development of models suitable for power system dynamic analysis,” NTNU, Trondheim, 2013.

[15] S. J. Chapman, Electric Machinery Fundamentals, Fifth Edition, New York, USA: The McGraw-Hill Companies, 2012.

[16] Jan Machowski, Janusz W. Bialek & James R. Bumby, Power System Dynamics Stability and Control, Second Edition, West Sussex, United Kingdom: John Wiley & Sons Ltd, 2008.

[17] R. K. Nilssen, Electromagnetics in Power Engineering, Compendium, Trondheim, Norway: NTNU, 2012.

[18] D. D. Hanselman, Brushless Permanent Magnet Motor Design, Second Edition, Ohio, USA: Magna Physics Publishing, 2006.

[19] IEEE Power Engineering Society, IEEE Guide for Synchronous Generator Modelling Practices and Applications in Power System Stability Analyses, New York, USA: The Institute of Electrical and Electronics Engineers, Inc., 2003.

[20] C.-M. Ong, Dynamic Simulation of Electric Machinery Using Matlab/Simulink, West Lafayette, India: Prentice Hall PTR, 1998.

[21] The MathWorks Inc., “SimPowerSystems, R2013b, PMSM block documentation, Second Generation,” MathWorks, 1994-2013.

[22] J. O. Buøy, “Development of high efficiency Axial Flux Motor for Shell Eco-Marathon,” NTNU, Trondheim, 2013.

[23] DNV GL Fuel Fighter; team 2010, “Master Report DNVFF2010,” NTNU, Trondheim, 2010.

[24] DNV GL Fuel Fighter; team 2011, “Master Report DNVFF2011,” NTNU, Trondheim, 2011.

[25] L. Nasrin, “Improved Version of Energy Efficient Motor for Shell Eco Marathon,” NTNU,

Trondheim, 2011.

[26] maxon motor, “Maxon EC 60 flat motor datasheet,” [Online]. Available: http://www.aviton.spb.ru/files/doc/pdf/maxon/ec_60_flat_en.pdf. [Accessed 9 June 2014].

[27] Maxon Motor, “DC motors and drive systems by maxon motor,” [Online]. Available: http://www.maxonmotor.com/maxon/view/content/index. [Accessed 27 May 2014].

[28] B. O. Wiik, “Elektrisk Fremdriftsystem for Shell Eco-Marathon PureChoice Kjøretøy,” NTNU, Trondheim, 2008.

[29] Ned Mohan, Tore M. Undeland & William P. Robbins, Power Electronics, Third Edition, Minneapolis/Trondheim: John Wiley & Sons, inc., 2003.

[30] Intertaional Rectifier, “International Rectifier - The Power Management Leader,” [Online]. Available: http://www.irf.com/. [Accessed 28 May 2014].

[31] International Rectifier, “Datasheet IR2101,” [Online]. Available: http://www.irf.com/product-info/datasheets/data/ir2101.pdf. [Accessed 10 June 2014].

[32] International Rectifier, “Datasheet IRS2336D,” [Online]. Available: http://www.irf.com/product-info/datasheets/data/irs2336.pdf. [Accessed 10 June 2014].

[33] International Rectifier, “Datasheet IRS26310DJPbF,” [Online]. Available: http://www.irf.com/product-info/datasheets/data/irs26310djpbf.pdf. [Accessed 10 June 2014].

[34] International Rectifier, [Online]. Available: http://www.irf.com/product-info/datasheets/data/iram136-3023b.pdf. [Accessed 10 June 2014].

[35] International Rectifier, [Online]. Available: http://www.irf.com/technical-info/refdesigns/irmdkg6-400w.pdf. [Accessed 10 June 2014].

[36] Avago Technologies, “Datasheet ACPL-333J,” [Online]. Available: http://www.avagotech.com/docs/AV02-1087EN. [Accessed 10 June 2014].

[37] K. Ljøkelsøy, “Inverter board V1_0 Documentation,” SINTEF, Trondheim, 2014.

[38] Noca, “Noca: Industrialisering og produksjon av elektronikk,” [Online]. Available: http://www.noca.no/. [Accessed 28 May 2014].

[39] Farnell, “B59901D90A40 - EPCOS - THERMISTOR, PTC | Farnell element14 Norge,” [Online]. Available: http://no.farnell.com/epcos/b59901d90a40/thermistor-ptc/dp/218832?CMP=GRHB-OCTOPART-1000341. [Accessed 10 June 2014].

[40] Farnell, “FDP032N08 - FAIRCHILD SEMICONDUCTOR - MOSFET, N CH, 75V, 120A, TO-220 | Farnell element14 Norge,” [Online]. Available: http://no.farnell.com/fairchild-semiconductor/fdp032n08/mosfet-n-ch-75v-120a-to-220/dp/2083328. [Accessed 10 June 2014].

[41] Farnell, “IRFB3077PBF - INTERNATIONAL RECTIFIER - MOSFET, N, 75V, TO-220 | Farnell element14 Norge,” [Online]. Available: http://no.farnell.com/international-rectifier/irfb3077pbf/mosfet-n-75v-to-220/dp/1298539. [Accessed 10 June 2014].

[42] Farnell, “STP75NF75 - STMICROELECTRONICS - MOSFET, N, TO-220 | Farnell element14 Norge,” [Online]. Available: http://no.farnell.com/stmicroelectronics/stp75nf75/mosfet-n-to-220/dp/1468003. [Accessed 10 June 2014].

[43] Midcom Trondheim as, “Midcom as: Home,” [Online]. Available: http://www.midcom.no/. [Accessed 28 May 2014].

[44] Elprint Norge AS, “Elprint Norge | Høykvalitets mønsterkort for det skandinaviske og det Nord-Europeiske marked,” [Online]. Available: http://www.elprint.no/. [Accessed 9 June 2014].

[45] Würth Elektronik CBT group, “WEdirekt – online shop powered by Würth Elektronik | PCBs and Stencils directly from Europe’s electronics specialist,” [Online]. Available: http://www.wedirekt.de/. [Accessed 9 June 2014].

[46] N. Mohan, Advanced Electric Drives, Twin Cities, Minnesota: MNPERE, 2011.

[47] National Instruments, “OEM OPERATING INSTRUCTIONS AND SPECIFICATIONS NI sbRIO-9605/9606 and NI sbRIO-9623/9626/9633/9636,” [Online]. Available: http://www.ni.com/pdf/manuals/373378c.pdf. [Accessed 9 June 2014].

[48] National Instruments, “National Instruments Norge,” [Online]. Available: http://norway.ni.com/. [Accessed 30 May 2014].

[49] H. Trømborg, “Control system for the DNV GL Fuel Fighter Prototype and the DNV GL Fuel Fighter UrbanConcept,” NTNU, Trondheim, 2014.

[50] K. Ljøkelsøy, “Control system for a three-phase grid connected converter. 3 december 2013 version. Description.,” SINTEF Energi AS, Trondheim, 2013.

[51] TRACO ELECTRONIC AG, “tracopower.com: Home,” [Online]. Available: http://www.tracopower.com/. [Accessed 31 May 2014].

[52] TRACO ELECTRONIC AG, “Datasheet THL 20WI Series, 20 Watt,” [Online]. Available: http://www.tracopower.com/fileadmin/medien/dokumente/pdf/datasheets/thl20wi.pdf. [Accessed May 31 2014].

[53] HEIDENHAIN, “Rotary Encoders catalogs,” 2005. [Online]. Available: http://www.atechauthority.com/pdf/Rotary_Prod.pdf#page=. [Accessed 1 June 2014].

[54] A Tech Authority, “HEIDENHAIN ROD 420,” [Online]. Available: http://www.atechauthority.com/products.asp?id=173. [Accessed 1 June 2014].

[55] US Digital, “US Digital,” [Online]. Available: http://usdigital.com/. [Accessed 1 June 2014].

[56] Gylling Teknikk, “A123 systems lithium-ion,” Gylling Teknikk, [Online]. Available: http://www.gylling.no/produkter/batterier/a123-batterier.shtml?meny=0;divmeny=0. [Accessed 23 4 2014].

[57] Wikimedia Foundation, Inc., “Gasoline gallon equivalent - Wikipedia, the free encyclopedia,” [Online]. Available: http://en.wikipedia.org/wiki/Gasoline_gallon_equivalent. [Accessed 10 June 2014].

[58] Google, “Google Maps,” [Online]. Available: http://www.google.com/maps/. [Accessed 10 June 2014].

Appendices

Appendix A.1: Simulink full system simulation results: Speed PI saturation limit = 20.

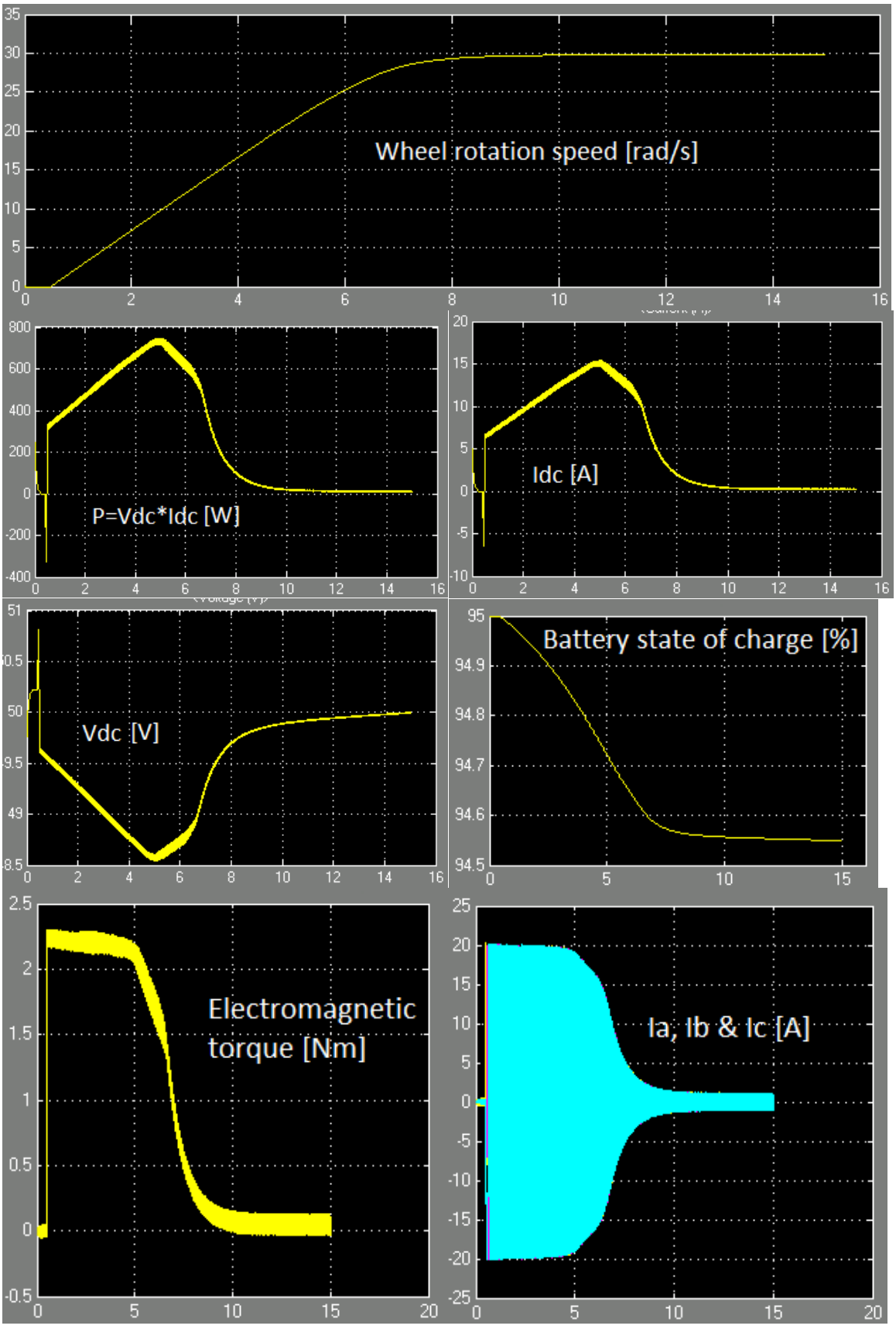

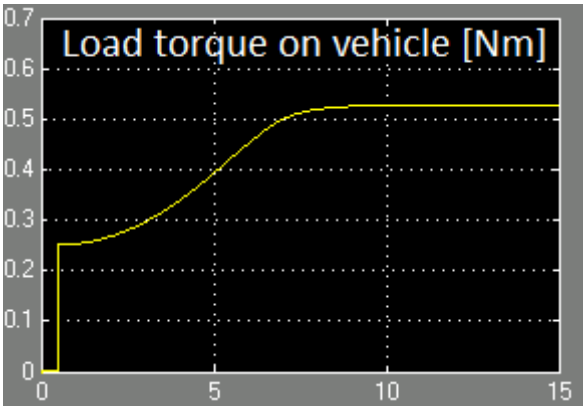
Load torque on vehicle [Nm]
0.7
0.6
0.5
0.4
0.3
0.2
0.1
0
0
5
10
15

Appendix A.2: Simulink full system simulation results: Speed PI saturation limit = 15.

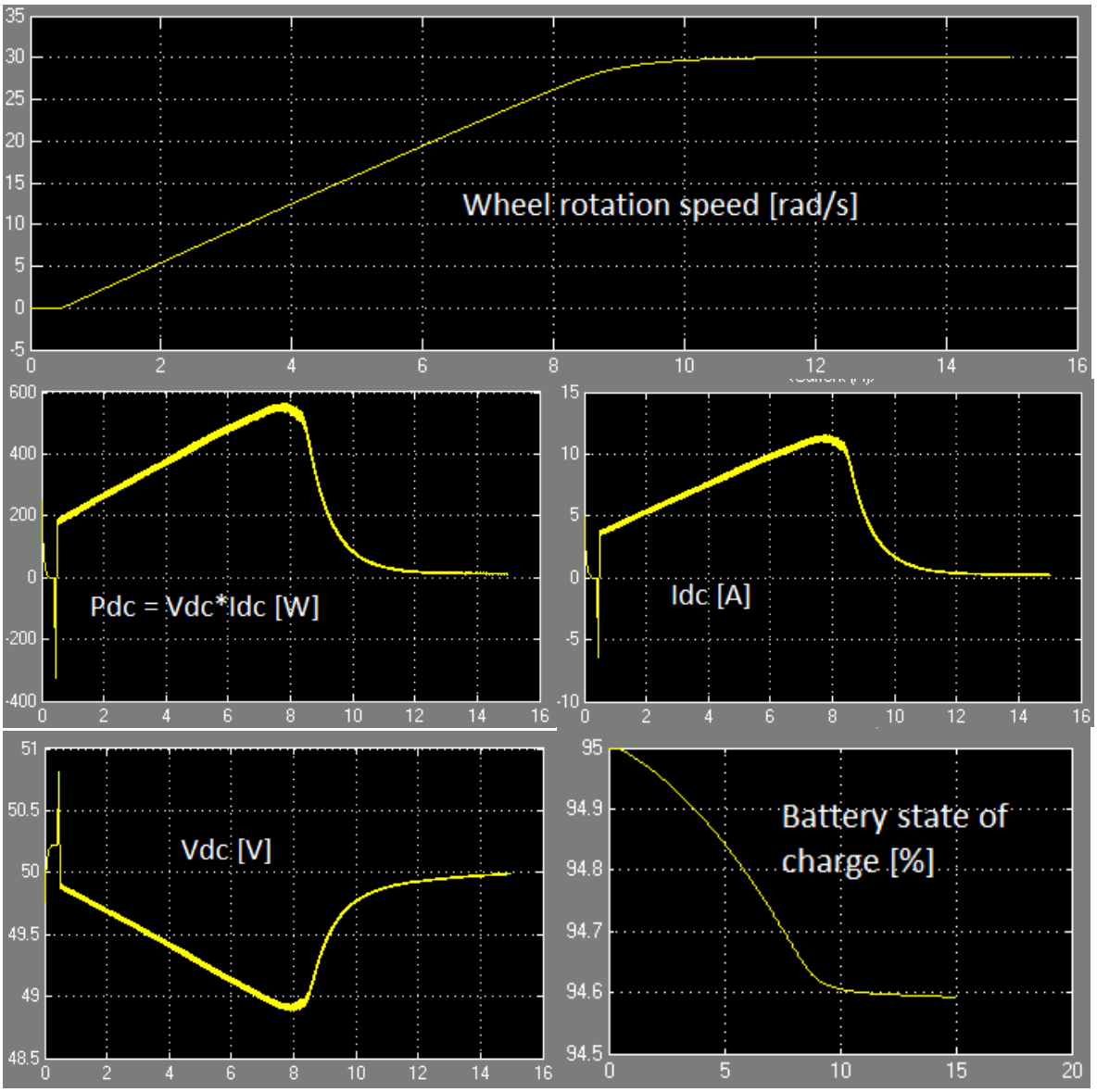

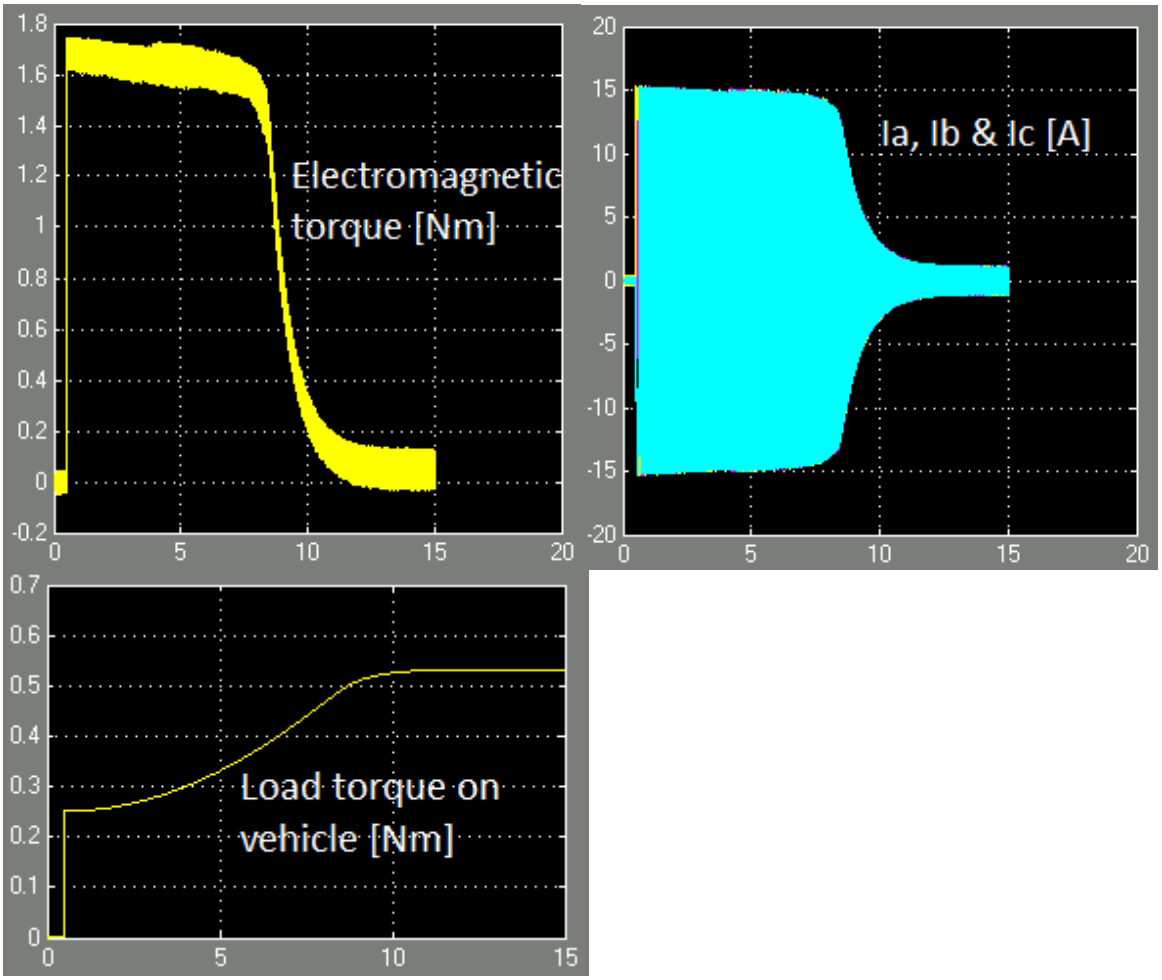
Electromagnetic torque [Nm]
Ia, Ib & Ic [A]
Load torque on vehicle [Nm]

Appendix A.3: Simulink full system simulation results: Speed PI saturation limit = 10.

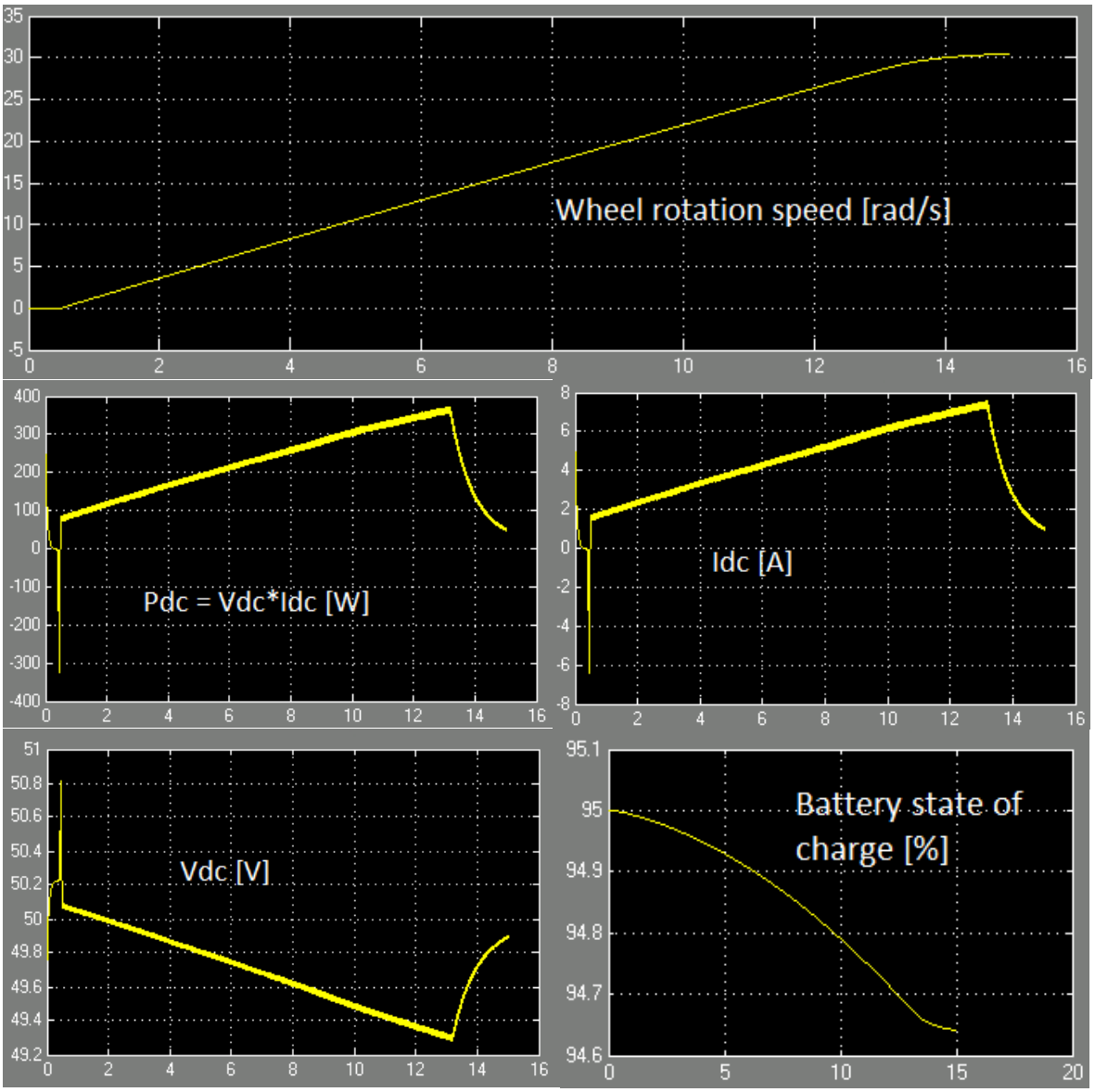

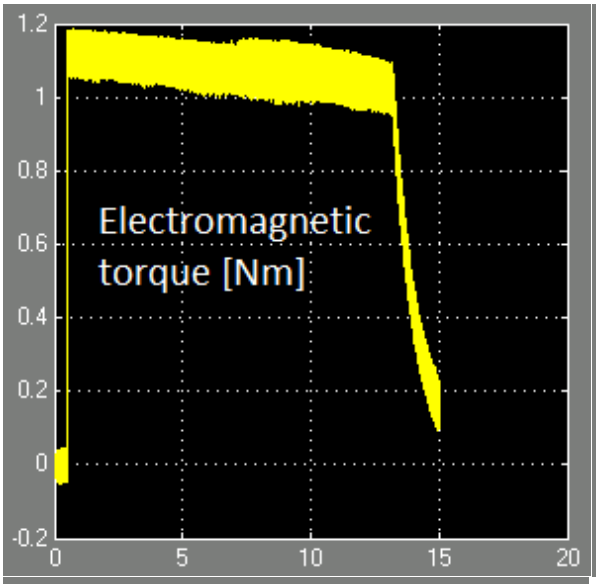
Electromagnetic
torque [Nm]

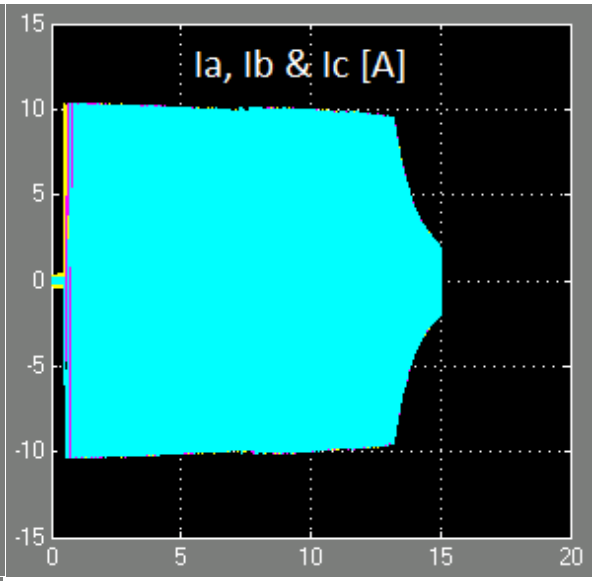
Ia, Ib & Ic [A]

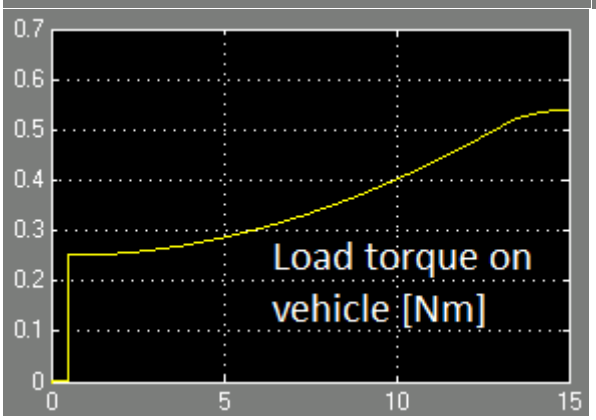
Load torque on
vehicle [Nm]

Appendix A.4: Simulink full system simulation results: Speed PI saturation limit = 5.

Note: Simulation time length changed from 15 to 30 seconds.

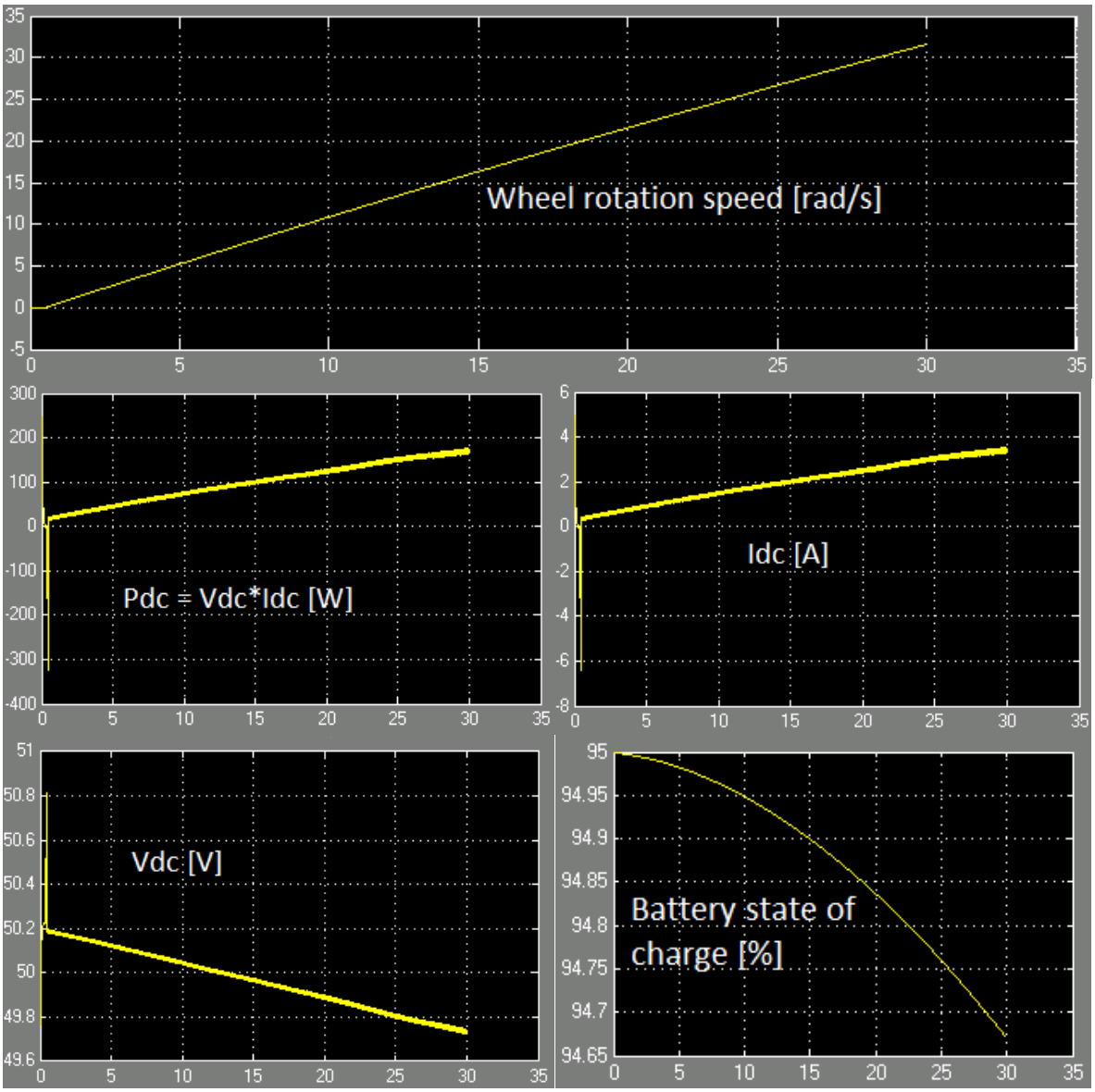

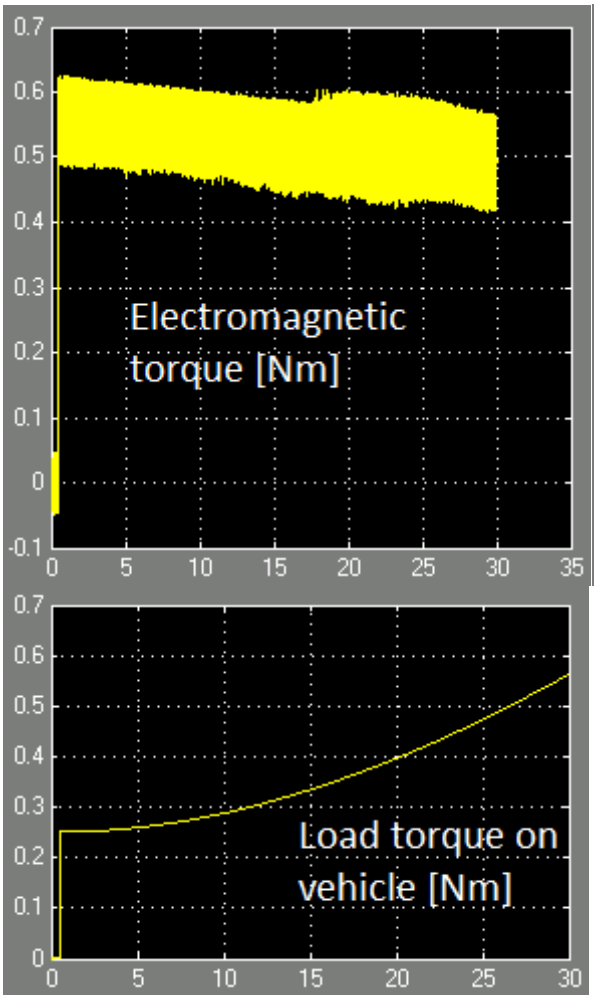
Electromagnetic
torque [Nm]
Load torque on
vehicle [Nm]

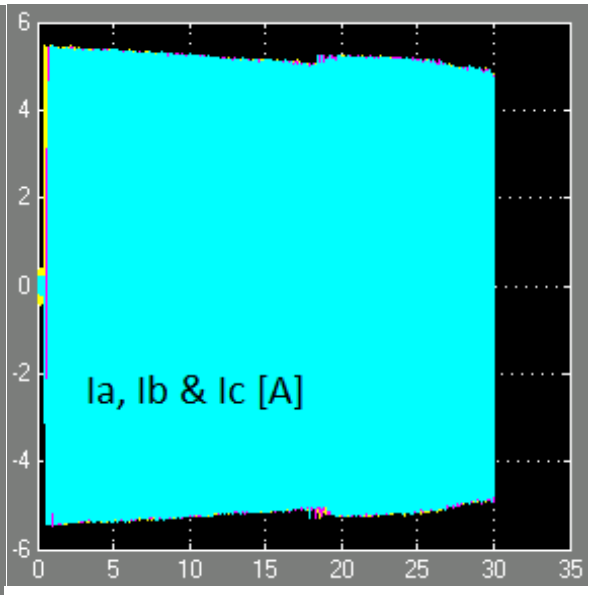
Ia, Ib & Ic [A]

Appendix A.5: Early simulation comparison between the simple and the complex inverter model.

Note: Parameterization does not perfectly match the final model parameterization. An ideal voltage source was used instead of the battery model for the complex model simulation presented here.

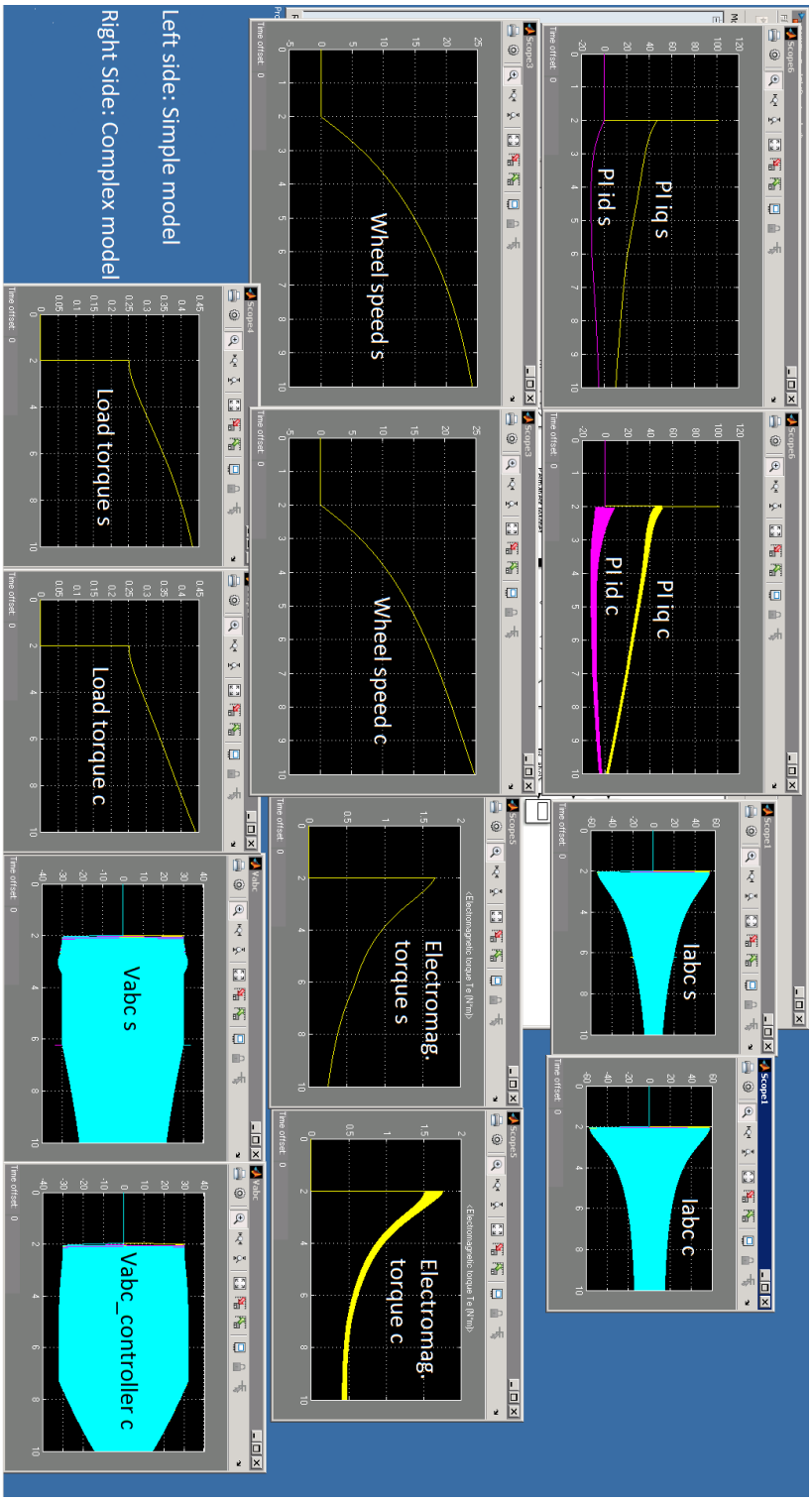

Appendix B.1: Efficiency tests on the 2011 axial flux motor

Equation used for the efficiency calculation:

Efficency = Pout/Pin

= (T [Nm] w [rad/s])/(Vdc*Idc) = (T [Nm] *0,104719755* w[rpm])/(Vdc*Idc)

B.1.1: Main efficiency test

Lab test 27-31.03.2014

Motor:	2011 Urban	
Inverter:	3kW IGBT	B03-0191
Contoller:	Sintef FPGA	
Switching freq.:	15000	
DC source:	40V/10A	B02-0365
Switched to variac for more power		

Measured: Vdc + Idc:

Speed [rpm]	20		40		60		80	
Torque [Nm]	A	V	A	V	A	V	A	V
0,5	0,12	32,17	0,16	32,12	0,22	32,09	0,26	32,1
1	0,22	38,56	0,29	32,05	0,40	32	0,38	37,4
1,5	0,33	38,49	0,39	38,44	0,47	37,79	0,7	31,9
2	0,43	38,35	0,52	38,37	0,63	38,34	0,88	31,8
2,5	0,55	38,38	0,67	38,30	0,77	38,28	0,93	38,2
3	0,67	38,38	0,84	38,23	0,97	38,2	1,155	38,1
3,5	0,80	38,25	0,98	38,16	1,19	38,1	1,39	38
4	0,93	38,18	1,18	38,09	1,38	38,03	1,59	38
4,5	1,10	38,11	1,35	38,03	1,55	37,97	1,9	37,8
5	1,30	37,98	1,50	37,98	1,80	37,9	2,1	37,8

100		120		140		160		180		200	
A	V	A	V	A	V	A	V	A	V	A	V
0,25	37,8	0,32	37,	0,36		0,40	37,8	0,46		0,54	
5	3	2	8	3	37,8	5	5	9	37,7	4	37,71
	31,9		31,		31,8		31,8				
0,54	1	0,66	7	0,71	8	0,86	1	0,92	31,8	0,95	31,81
	31,8		37,	0,84	37,5	0,99	37,5		37,4	1,17	
0,81	4	0,77	6	8	8	4	8	1,09	8	5	37,37

		1,03	37,	1,15	37,4	1,33	37,4		31,5		
1,12	31,7	5	5	5	8	3	4	1,7	8	1,9	31,54
	38,1		37,		37,3		37,3		37,2		
1,1	6	1,24	4	1,46	4	1,62	3	1,78	4	1,99	37,16
1,38	38,0		31,				31,4		37,1		
5	6	1,9	5	2,09	31,5	2,4	1	2,18	2	2,38	37,01
	37,9		37,	2,01	37,8		36,0		31,0		
1,62	6	1,9	8	5	8	2,3	5	3,17	5	2,8	36,87
1,88	37,8		37,		37,7		31,2		36,8		
5	7	2,15	8	2,37	2	3,16	6	2,92	9	3,8	31,09
	37,7		37,		37,5		37,4				
2,1	8	2,43	6	2,72	6	2,95	8	4,1	30,9	4,42	30,9
2,47			37,		37,4		37,3		37,1		36,99
5	37,6	2,7	5	3,06	6	3,39	1	3,72	6	4,05	5

220		240		260		280		300		320	
A	V	A	V	A	V	A	V	A	V	A	V
0,585	37,66	0,63	37,71	0,68	37,7	0,78	31,89	0,72	38,27	0,751	38,27
1,17	31,73	1,05	37,53	1,14	37,54	1,42	31,71	1,166	38,14	1,22	38,09
1,295	37,37	1,49	37,42	1,53	37,4	1,72	34,68	1,665	37,97	1,722	37,9
2,05	31,48	1,94	37,26	2,05	37,24	2,167	34,52	2,16	37,86	2,295	37,78
2,12	37,14	2,45	37,1	2,5	37,12	2,72	34,37	2,64	37,71	2,38	46
2,94	31,24	3,1	36,89	3,18	37	3,26	34,2	3,135	37,55	2,825	45,26
3,45	31,1	3,27	36,96	3,8	36,75	3,55	36,84	3,7	37,36	3,4	44,2
3,5	36,7	4,3	30,87	4,3	36,6	4,13	36,62	4,3	37,15	3,93	43,46
4,58	30,81	4,13	36,69	5,2	36,4	5,05	36,4	4,49	41,02	4,78	40,55
4,34	36,36	4,56	36,61	5,7	36,26	5,73	36,17	4,989	40,17	5,185	41,56

Efficiency calculation:

Speed [km/h]	1,959	3,919	5,878	7,837	9,7968	11,76	13,7155	15,7
Speed [rpm]	20	40	60	80	100	120	140	160
Torque [Nm]								
0,5	0,27	0,41	0,44	0,50	0,54	0,52	0,53	0,55
1	0,25	0,45	0,49	0,59	0,61	0,60	0,65	0,61
1,5	0,25	0,42	0,53	0,56	0,61	0,65	0,69	0,67
2	0,25	0,42	0,52	0,60	0,59	0,65	0,68	0,67
2,5	0,25	0,41	0,53	0,59	0,62	0,68	0,67	0,69
3	0,24	0,39	0,51	0,57	0,60	0,63	0,67	0,67
3,5	0,24	0,39	0,49	0,55	0,60	0,61	0,67	0,71
4	0,24	0,37	0,48	0,55	0,59	0,62	0,66	0,68
4,5	0,22	0,37	0,48	0,53	0,59	0,62	0,65	0,68
5	0,21	0,37	0,46	0,53	0,56	0,62	0,64	0,66

17,63	19,59	21,55	23,5	25,47	27,43	29,39	31,35
180	200	220	240	260	280	300	320
0,53	0,51	0,52	0,53	0,53	0,59	0,68	0,58
0,64	0,69	0,62	0,64	0,64	0,65	0,85	0,72
0,69	0,72	0,71	0,68	0,71	0,74	0,82	0,77
0,70	0,70	0,71	0,70	0,71	0,78	0,84	0,77
0,71	0,71	0,73	0,69	0,73	0,78	0,87	0,77
0,70	0,71	0,75	0,66	0,69	0,79	0,88	0,79
0,67	0,71	0,75	0,73	0,68	0,78	0,81	0,78
0,70	0,71	0,72	0,76	0,69	0,78	0,80	0,78
0,67	0,69	0,73	0,75	0,65	0,72	0,86	0,78
0,68	0,70	0,73	0,75	0,66	0,71	0,87	0,78

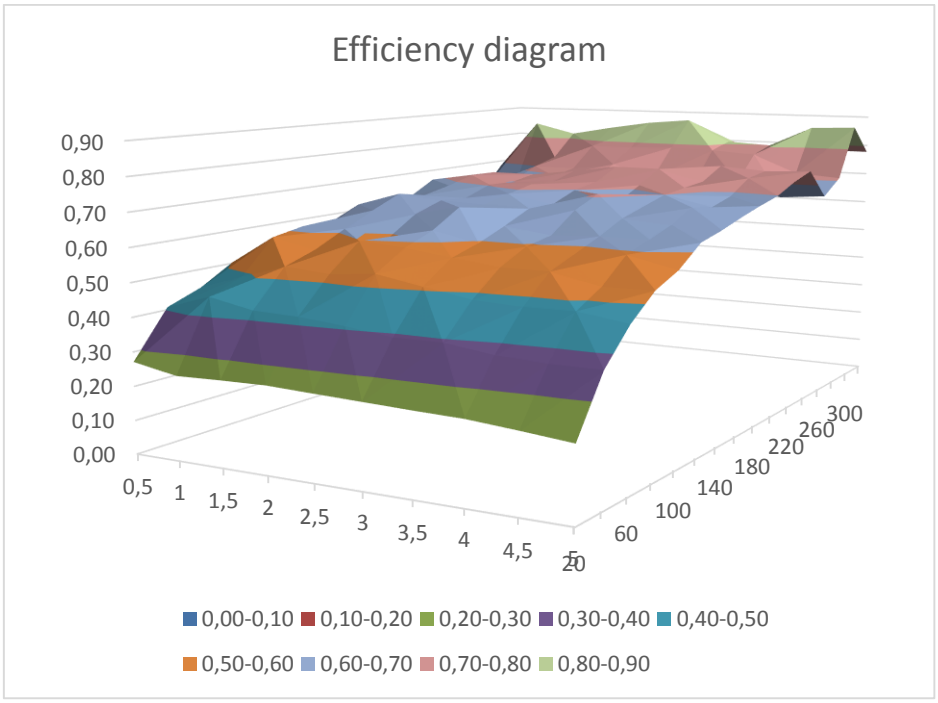
Efficiency diagram
0,90
0,80
0,70
0,60
0,50
0,40
0,30
0,20
0,10
0,00
0,5
1
1,5
2
2,5
3
3,5
4
4,5
5
20
60
100
140
180
220
260
300
0,00-0,10
0,10-0,20
0,20-0,30
0,30-0,40
0,40-0,50
0,50-0,60
0,60-0,70
0,70-0,80
0,80-0,90

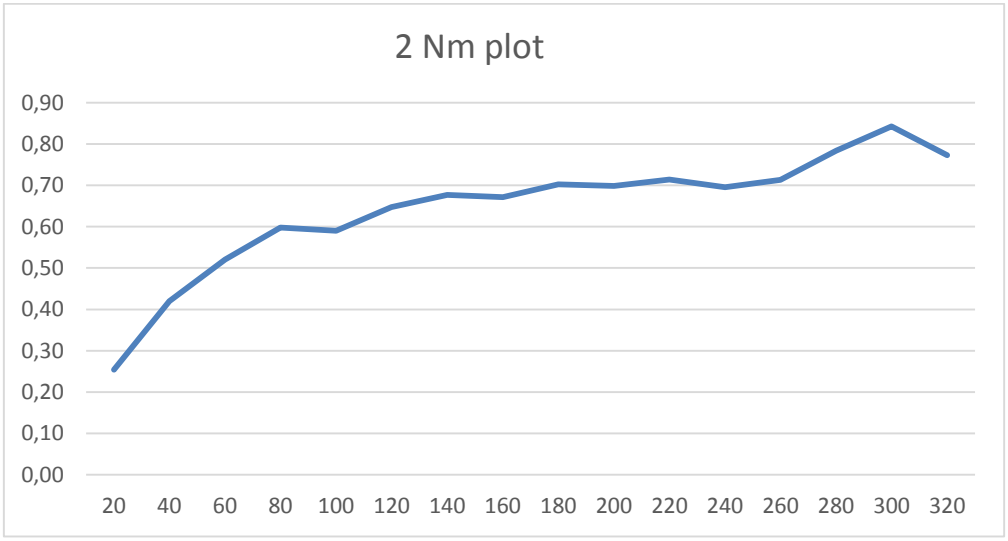
2 Nm plot
0,90
0,80
0,70
0,60
0,50
0,40
0,30
0,20
0,10
0,00
20
40
60
80
100
120
140
160
180
200
220
240
260
280
300
320

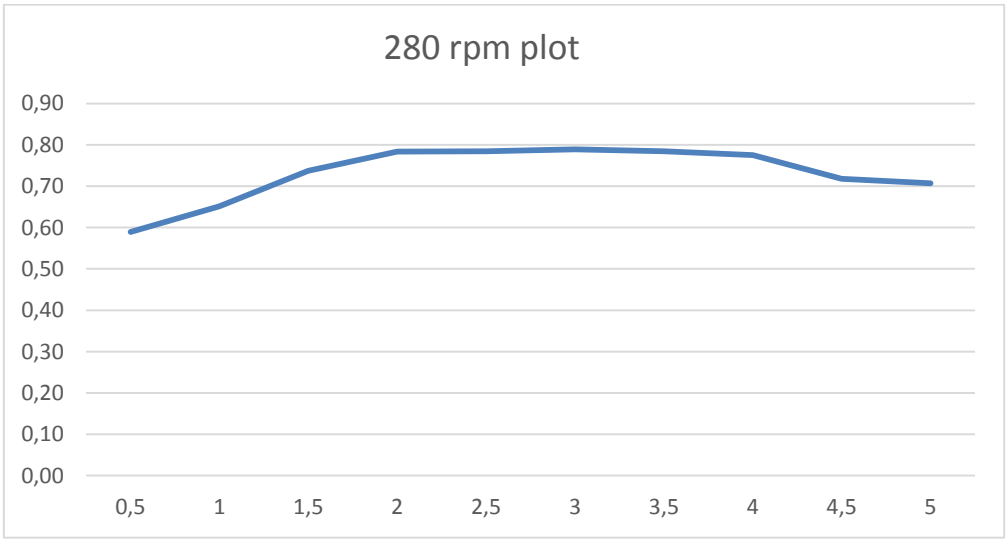
280 rpm plot
0,90
0,80
0,70
0,60
0,50
0,40
0,30
0,20
0,10
0,00
0,5
1
1,5
2
2,5
3
3,5
4
4,5
5

B.1.2: Increased voltage test

Lab test
06.04.2014

Motor:	2011 Urban	
Inverter	3kW IGBT: B03-0191	
Controller:	Sintef FPGA	
DC source:	Variac and rectifier: B01-0426 & B02-0562	
Switching freq.:	15000	Hz

Measured:
Vdc + Idc:

Speed [rpm]		40		80		120		160	
Torque [Nm]		A	V	A	V	A	V	A	V
	0,5	0,12	56,40	0,18	56	0,25	55,42	0,33	57,1
	1	0,24	55,60	0,283	55,34	0,42	54,39	0,55	56
	1,5	0,32	55,00	0,425	54,53	0,58	53,6	0,75	55,2
	2	0,40	54,95	0,59	53,83	0,77	52,75	0,96	54,6
	2,5	0,53	54,30	0,73	53,03	0,97	52	1,15	54
	3	0,64	53,80	0,9	52,3	1,165	51,48	1,43	53,3
	3,5	0,78	53,30	1,07	51,9	1,415	50,8	1,7	52
	4	0,94	52,70	1,25	51,23	1,6	50,4	1,97	51,8
	4,5	1,05	52,26	1,46	51,02	1,9	49,76	2,23	50,9
	5	1,19	51,83	1,61	50,56	2,12	49,1	2,54	50,5

200		240		280		320	
A	V	A	V	A	V	A	V
0,385	57	0,47	56,5	0,53	56,75	0,575	56,4
0,675	51,16	0,74	55,4	0,86	55,3	0,9	55,13
0,897	55,08	1,04	54,2	1,195	54,16	1,3	54,2
1,218	49,47	1,34	53,3	1,55	53,2	1,765	52,75
1,37	53,7	1,69	52,6	1,94	52,1	2,16	51,7
1,83	48	1,99	51,8	2,27	51,4	2,52	51
2,05	52,13	2,37	51,3	2,7	50,4	3,1	49,75
2,38	50,5	2,7	50,5	3,18	49,6	3,6	48,97
2,65	50,25	3,16	49,8	3,59	48,8	4,07	48,2
3,1	49	3,55	48,9	3,99	48,38	4,6	47,43

Efficiency calculation:

Speed [km/h]		3,919	7,837	11,76	15,67	19,594	23,51	27,4	31,3
Speed [rpm]		40	80	120	160	200	240	280	320
Torque [Nm]									
	0,5	0,31	0,42	0,45	0,45	0,48	0,47	0,49	0,52
	1	0,32	0,53	0,55	0,54	0,61	0,61	0,62	0,68
	1,5	0,36	0,54	0,61	0,61	0,64	0,67	0,68	0,71
	2	0,38	0,53	0,62	0,64	0,70	0,70	0,71	0,72
	2,5	0,36	0,54	0,62	0,68	0,71	0,71	0,73	0,75
	3	0,36	0,53	0,63	0,66	0,72	0,73	0,75	0,78
	3,5	0,35	0,53	0,61	0,66	0,69	0,72	0,75	0,76
	4	0,34	0,52	0,62	0,66	0,70	0,74	0,74	0,76
	4,5	0,35	0,51	0,60	0,66	0,71	0,72	0,75	0,77
	5	0,34	0,51	0,60	0,65	0,69	0,72	0,76	0,77

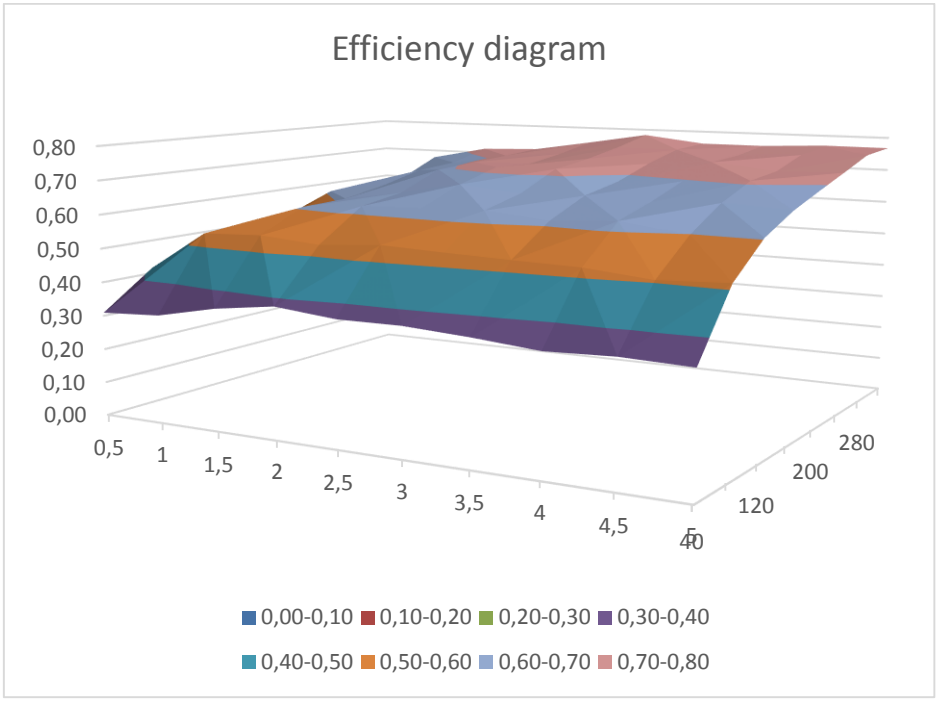

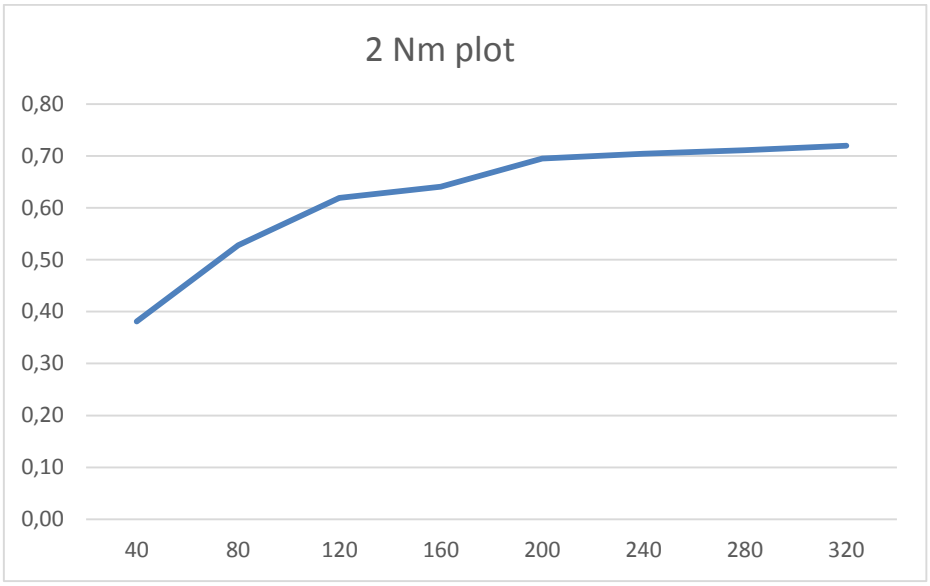
2 Nm plot
0,80
0,70
0,60
0,50
0,40
0,30
0,20
0,10
0,00
40
80
120
160
200
240
280
320

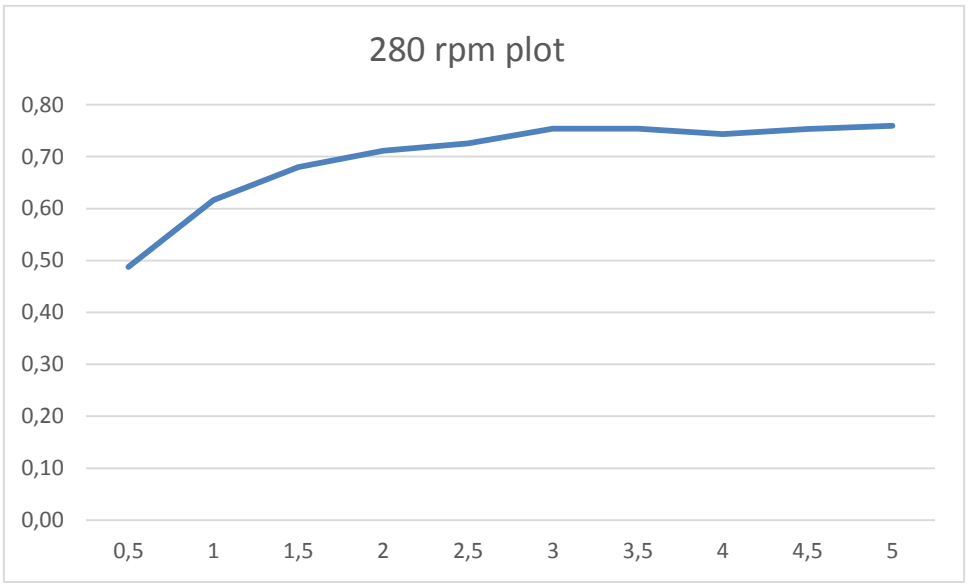
280 rpm plot
0,80
0,70
0,60
0,50
0,40
0,30
0,20
0,10
0,00
0,5
1
1,5
2
2,5
3
3,5
4
4,5
5

B.1.3: Reduced switching frequency test

Lab test 06.04.2014

Motor:	2011 Urban	
Inverter:	3kW IGBT B03-0191	
Controller:	Sintef FPGA	
DC source:	Variac & rectifier: B01-0426 & B02-0562	
Switching freq.:	4000	Hz

Measurements: Vdc + Idc

Speed [rpm]	40		80		120		160	
Torque [Nm]	A	V	A	V	A	V	A	V
0,5	0,21	43,68	0,3	43,2	0,384	43,06	0,44	42,7
1	0,30	43,20	0,45	42,6	0,58	42,29	0,73	41,6
1,5	0,40	42,68	0,62	41,88	0,82	41,3	1,03	40,5
2	0,49	42,49	0,78	41,41	1,05	40,58	1,3	39,8
2,5	0,63	41,93	0,95	40,93	1,28	39,88	1,63	38,9
3	0,81	41,40	1,2	40,15	1,59	39,04	1,95	38,4
3,5	1,03	40,76	1,45	39,43	1,87	38,45	2,39	37,4
4	1,14	40,48	1,68	38,9	2,2	38,1	2,78	36,8
4,5	1,39	39,84	1,95	38,4	2,55	37,5	3,27	36
5	1,55	39,43	2,23	37,9	2,989	36,7	3,6	35,5

200		240		280		320	
A	V	A	V	A	V	A	V
0,57	37,6	0,68	37,2	0,63	45,6	0,67	47,8
0,94	36,37	1,12	36	1	44,58	1,1	46,4
1,25	35,6	1,55	34,7	1,43	43,3	1,5	47,4
1,678	35,28	2	33,7	1,85	42,25	1,989	46,08
2,17	34,33	2,5	33	2,38	41,1	2,37	45,3
2,63	33,56	3,1	31,9	2,9	40,2	2,98	44
3,19	32	3,7	30,9	3,4	39,48	3,57	43
3,79	31	3,69	35,9	3,98	38,58	4,05	42,37
4,3	30,4	4,34	34,9	4,58	37,9	4,69	41,44
5,12	29,3	5	34,1	5,18	37,35	5,5	40,33

Efficiency calculation:

Speed [km/h]	3,919	7,837	11,76	15,67	19,59	23,51	27,4	31,3
Speed [rpm]	40	80	120	160	200	240	280	320
Torque [Nm]								
0,5	0,23	0,32	0,38	0,44	0,49	0,50	0,51	0,52
1	0,33	0,44	0,51	0,55	0,61	0,62	0,66	0,66
1,5	0,37	0,48	0,56	0,60	0,71	0,70	0,71	0,71
2	0,40	0,52	0,59	0,65	0,71	0,75	0,75	0,73
2,5	0,39	0,54	0,62	0,66	0,70	0,76	0,75	0,78
3	0,37	0,52	0,61	0,67	0,71	0,76	0,75	0,77
3,5	0,35	0,51	0,61	0,66	0,72	0,77	0,76	0,76
4	0,36	0,51	0,60	0,66	0,71	0,76	0,76	0,78
4,5	0,34	0,50	0,59	0,64	0,72	0,75	0,76	0,78
5	0,34	0,50	0,57	0,65	0,70	0,74	0,76	0,76

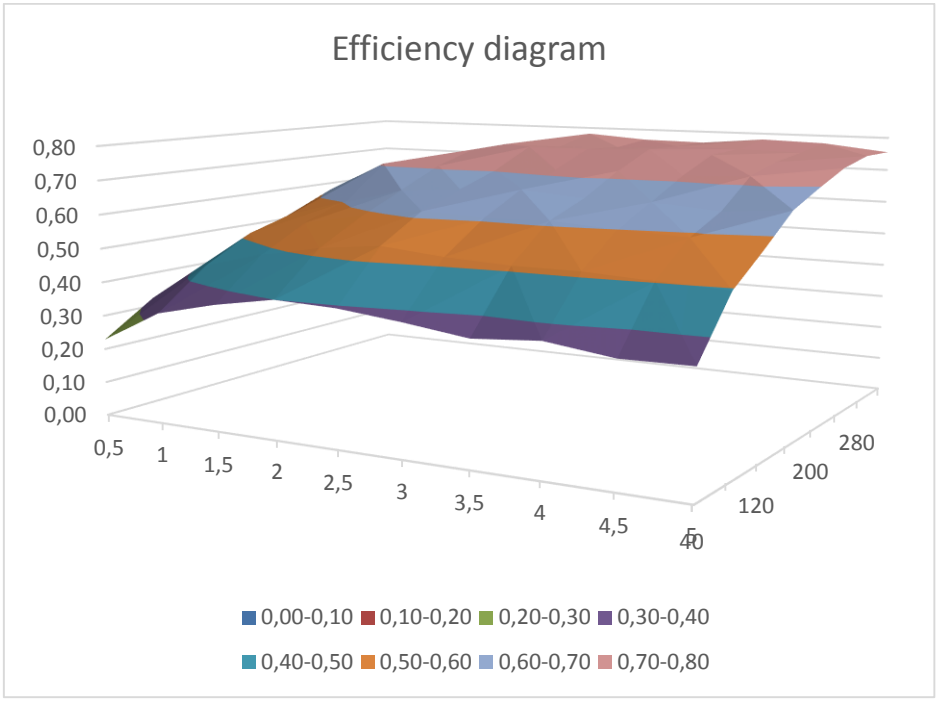

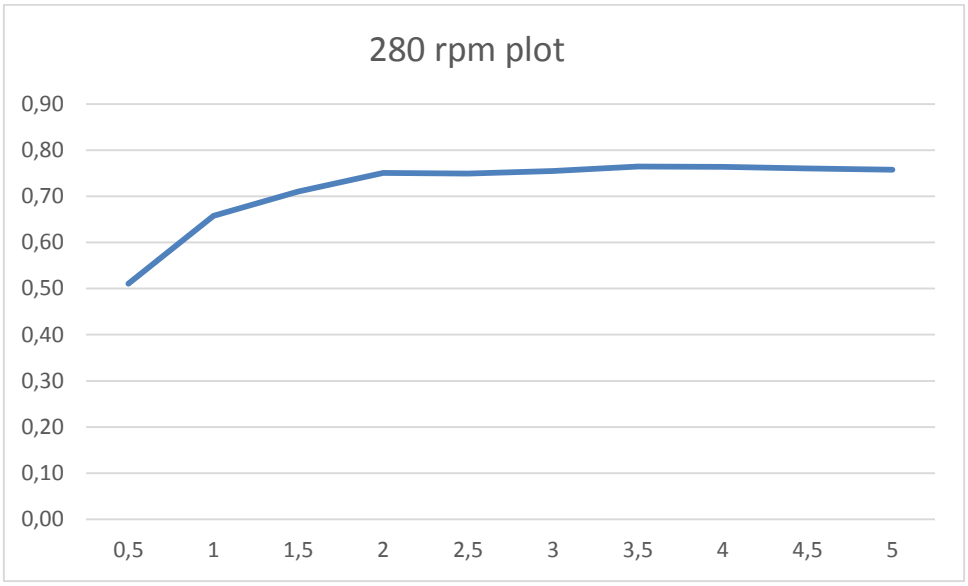
280 rpm plot
0,90
0,80
0,70
0,60
0,50
0,40
0,30
0,20
0,10
0,00
0,5
1
1,5
2
2,5
3
3,5
4
4,5
5

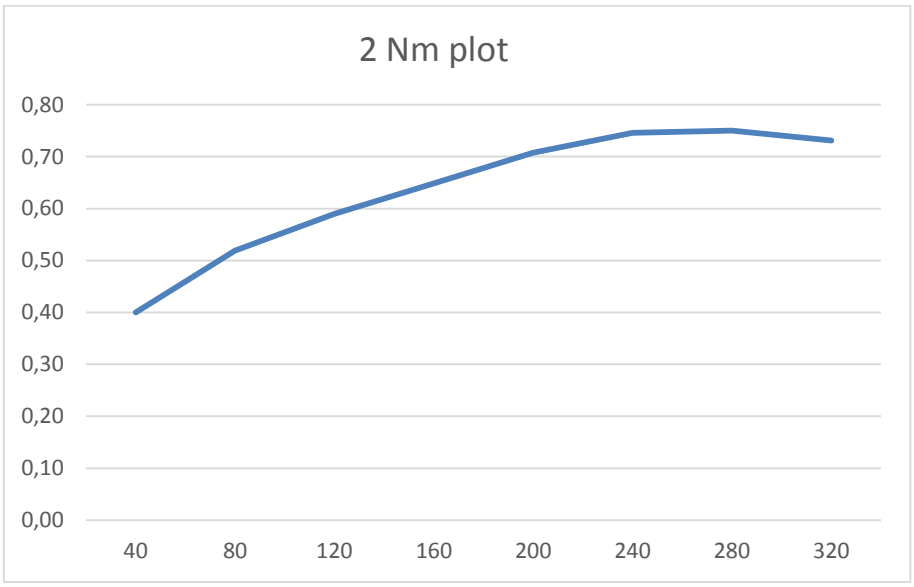
2 Nm plot
0,80
0,70
0,60
0,50
0,40
0,30
0,20
0,10
0,00
40
80
120
160
200
240
280
320

B.1.4: 1-25 kHz efficiency test

Lab test 06.04.2014

Motor:	2011 Urban 3kW IGBT	
Inverter:	B03-0191	
Controller:	Sintef FPGA	
Variac & rectifier:		
DC source:	B01-0426 & B02-0562	
Torque:	3,5	Nm
Speed:	19,59	km/h
Speed:	200	rpm

Measurements:	Vdc + Idc		Efficiency calculation:	
Switch. freq. [Hz]	A	V	Hz	%
1000	2,50	42,10	1000	69,65
2500	2,46	42,47	2500	70,16
5000	2,46	42,42	5000	70,36
7500	2,43	42,60	7500	70,81
10000	2,38	42,74	10000	72,06
12500	2,39	42,70	12500	71,83
15000	2,39	42,71	15000	71,84
17500	2,38	42,74	17500	72,22
20000	2,39	42,67	20000	71,88
22500	2,38	42,66	22500	72,26
25000	2,37	42,93	25000	72,14

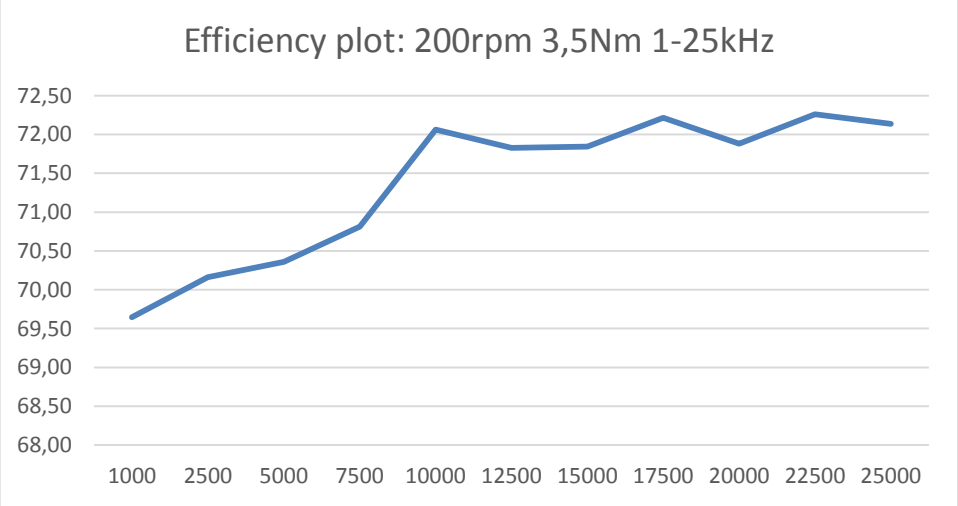

Appendix B.2: AXI motor 1-25 kHz efficiency test (FAILED)

Lab. test 07.05.2014

Motor:	AXI	
Inverter:	Inverterboard with STB75NF75 MOSFET	
Controller:	FPGA Virtex 5 sintef motor controller 40V/10A: B02-0365	
DC source:		
Torque:	0,8	Nm
Speed:	11,76	km/h
Speed:	1200	rpm

Measurements: Vdc + Idc

Switchfreq. [Hz]	A	V
1000	3,42	39,83
2500	3,43	39,82
5000	3,44	39,82
7500	3,41	39,82
10000	3,49	39,81
12500	3,58	39,80
15000	3,63	39,81
17500	3,65	39,79
20000	3,67	39,76
22500		
25000	3,65	39,77

Efficiency calculation:

Hz	%
1000	73,76
2500	73,67
5000	73,50
7500	74,14
10000	72,46
12500	70,56
15000	69,62
17500	69,22
20000	68,89
22500	#####
25000	69,26

Comment: Position measurement slowly changed while the measurements were made.

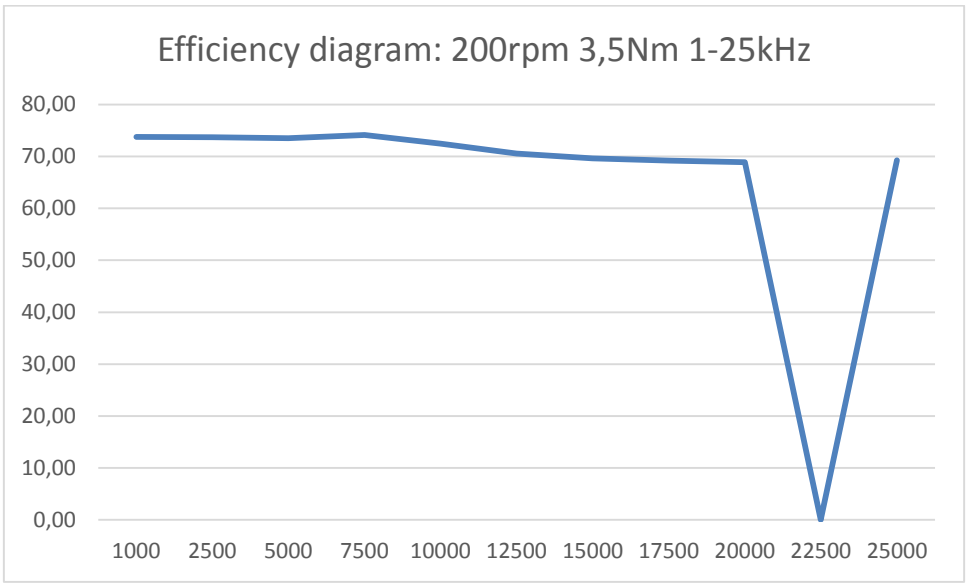

Appendix C: Active DSP motordrive setup

Contact Kjell Ljøkelsøy, at SINTEF Energi [11], in order to receive the files needed. First off open the project: Ctrl+O and select “Motorstyring_prosj.xml”. Now a few more steps has to be done before the FPGA can be connected. First add a module at Setup>Add Module and select “PPC_DLL.dll”. See figure C1.

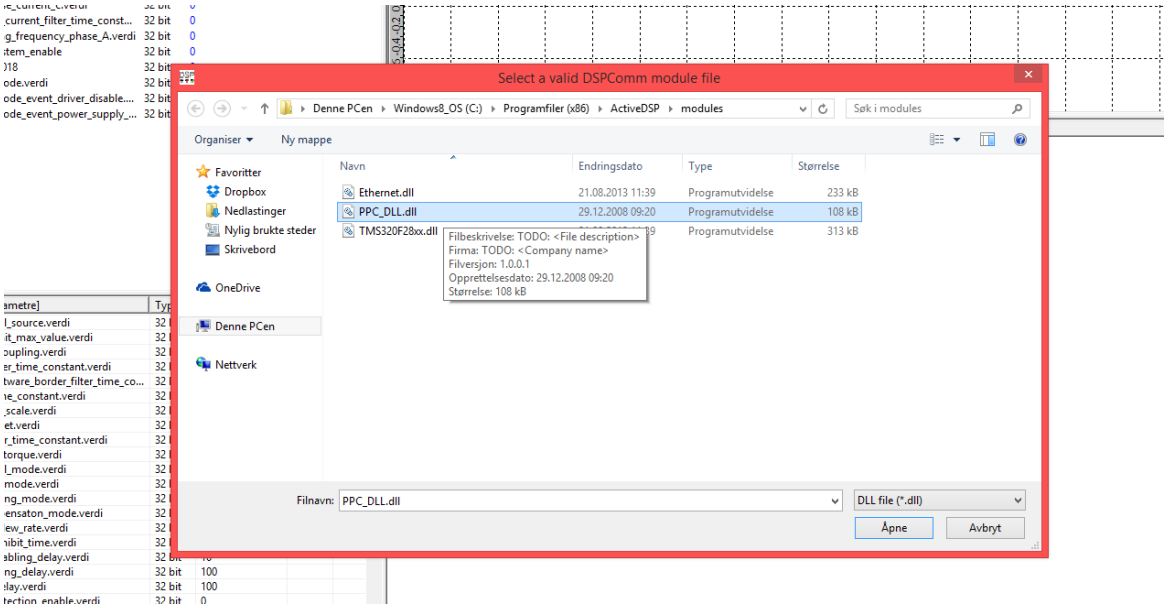

Figure C1: ActiveDSP, add module: PPC_DLL.dll

Next select the default processor. This can be accessed at Setup>Select processor. Now select the processor “PowerPC 405 Dwarf” as in figure C2.

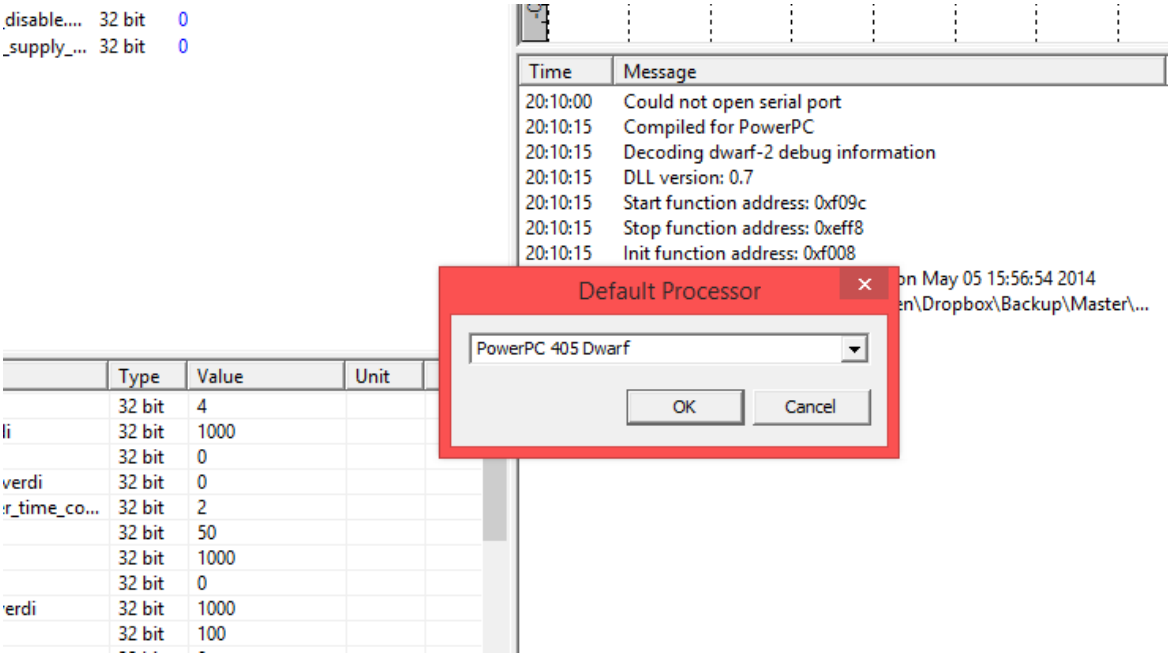

Figure C2: ActiveDSP, select processor: PowerPC 405 Dwarf

Now connect the computer to the FPGA serial port. When this is done go to;

Setup>Communication>Serial, and select the appropriate serial port (note that it is not necessarily COM1) and set the baud rate to 115200 as in figure C3:

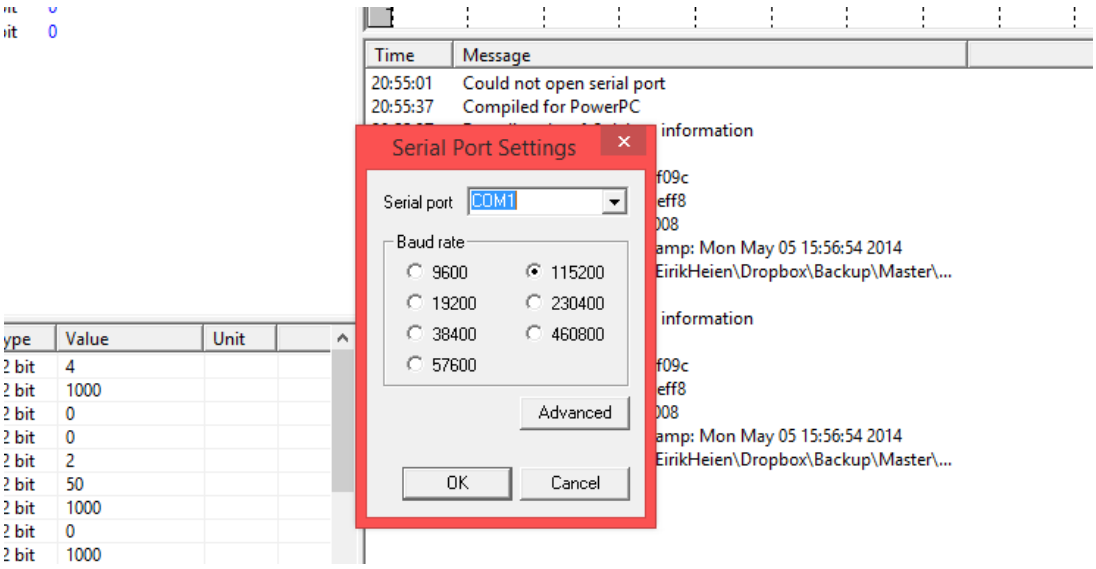

Figure C3: ActiveDSP: select serial port and baud rate

Finally make go to Setup>Run as... and make sure that “Standalone” is selected. See figure C4:

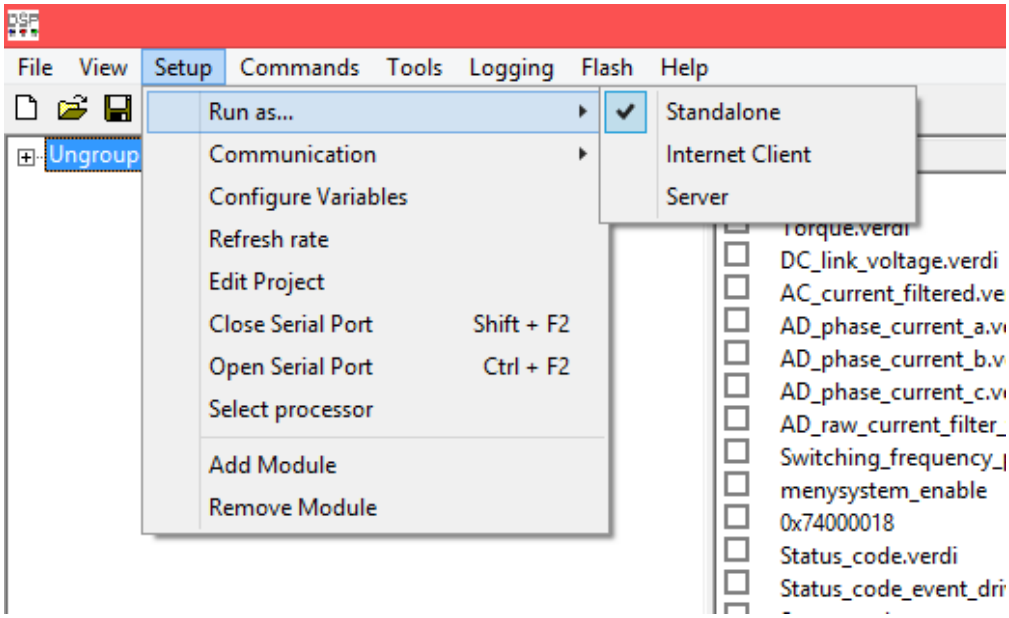

Figure C4: ActiveDSP: run as standalone

Check if the FPGA answers. Click F2 (Commands>Ping). If no reply appears in the message window then try to close and reopen the serial port: Shift+F2 (Setup>Close serial port) then Ctrl+F2 (Setup>Open serial port) and try F2 (Commands>Ping) again.

Appendix D.1: Urban motor drive controller settings

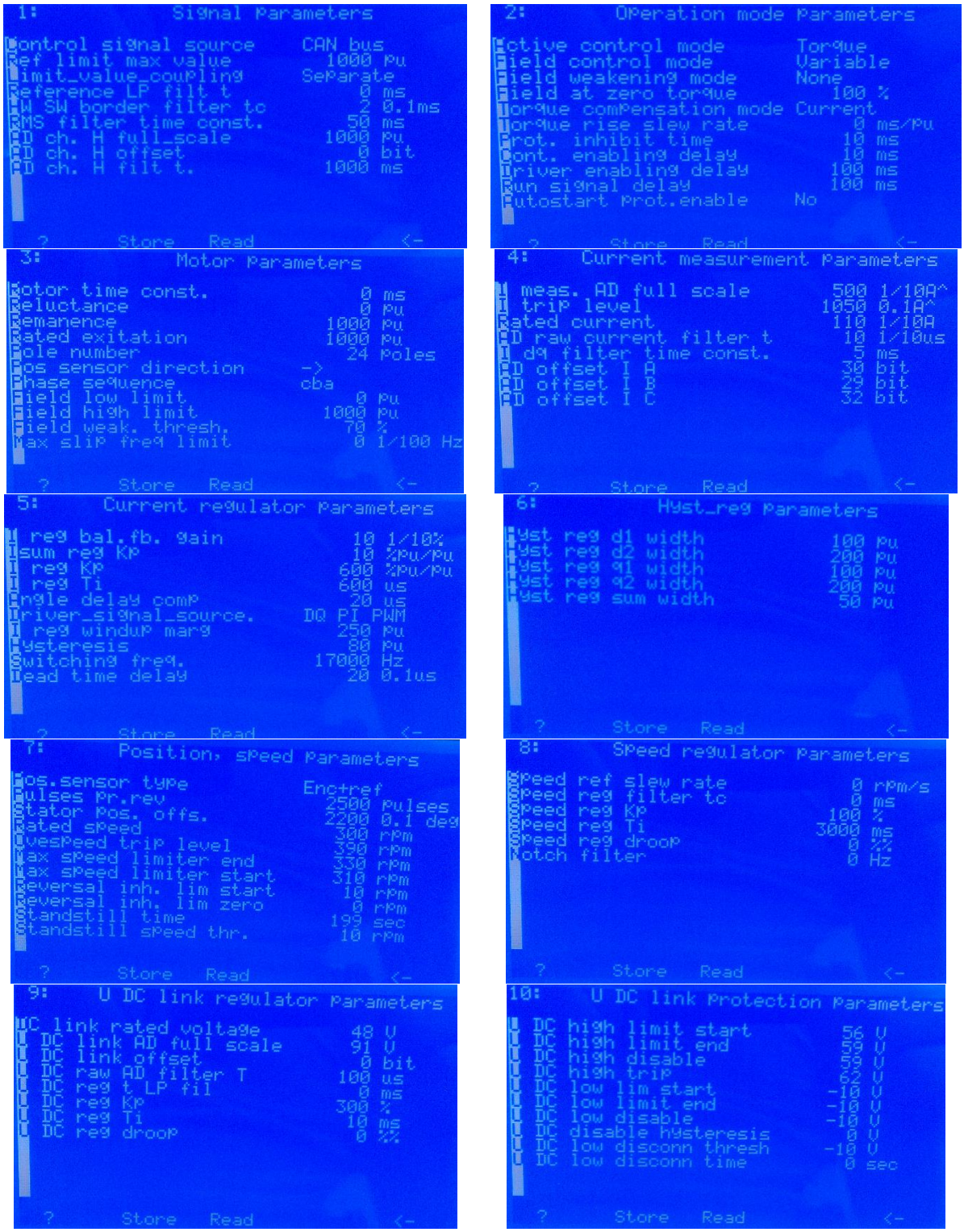

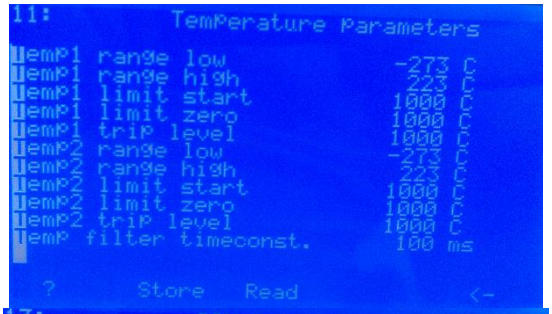
11: Temperature parameters
Temp1 range low -273 C
Temp1 range high 223 C
Temp1 limit start 1000 C
Temp1 limit zero 1000 C
Temp1 trip level 1000 C
Temp2 range low -273 C
Temp2 range high 223 C
Temp2 limit start 1000 C
Temp2 limit zero 1000 C
Temp2 trip level 1000 C
Temp filter timeconst. 100 ms
? Store Read <-

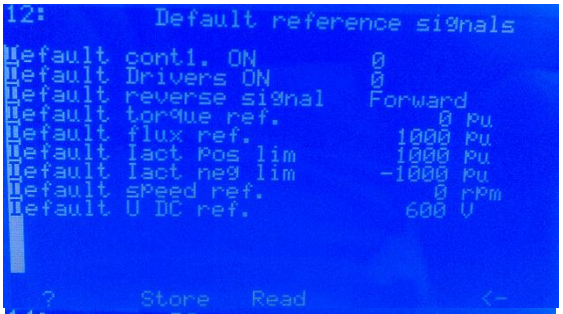
12: Default reference signals
Default cont1. ON 0
Default Drivers ON 0
Default reverse signal Forward
Default torque ref. 0 Pu
Default flux ref. 1000 Pu
Default Iact Pos lim 1000 Pu
Default Iact neg lim -1000 Pu
Default speed ref. 0 rPm
Default U DC ref. 600 V
? Store Read <-

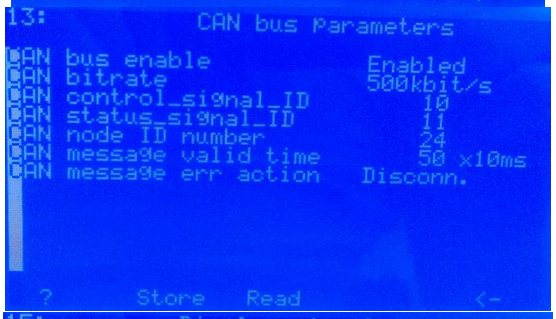
13: CAN bus Parameters
CAN bus enable Enabled
CAN bitrate 500kbit/s
CAN control_signal_ID 10
CAN status_signal_ID 11
CAN node ID number 24
CAN message valid time 50 x10ms
CAN message err action Disconn.
? Store Read <-

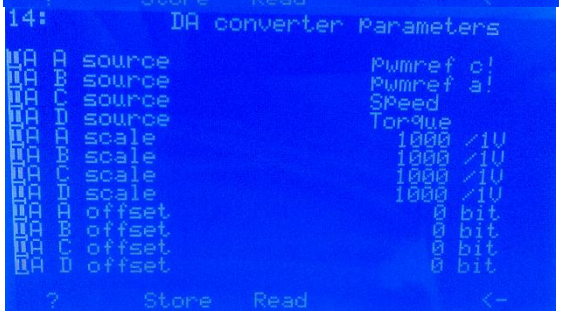
14: DA converter Parameters
DA A source Pwmref c!
DA B source Pwmref a!
DA C source Speed
DA D source Torque
DA A scale 1000 /1V
DA B scale 1000 /1V
DA C scale 1000 /1V
DA D scale 1000 /1V
DA A offset 0 bit
DA B offset 0 bit
DA C offset 0 bit
DA D offset 0 bit
? Store Read <-

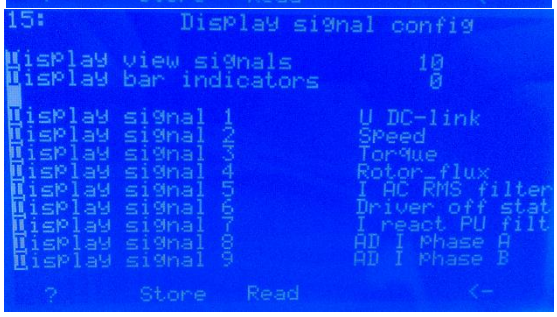
15: Display signal config
Display view signals 10
Display bar indicators 0
Display signal 1 U DC-link
Display signal 2 Speed
Display signal 3 Torque
Display signal 4 Rotor_flux
Display signal 5 I AC RMS filter
Display signal 6 Driver off stat
Display signal 7 I react PU filt
Display signal 8 AD I Phase A
Display signal 9 AD I Phase B
? Store Read <-

Appendix D.2: Prototype motor drive controller settings

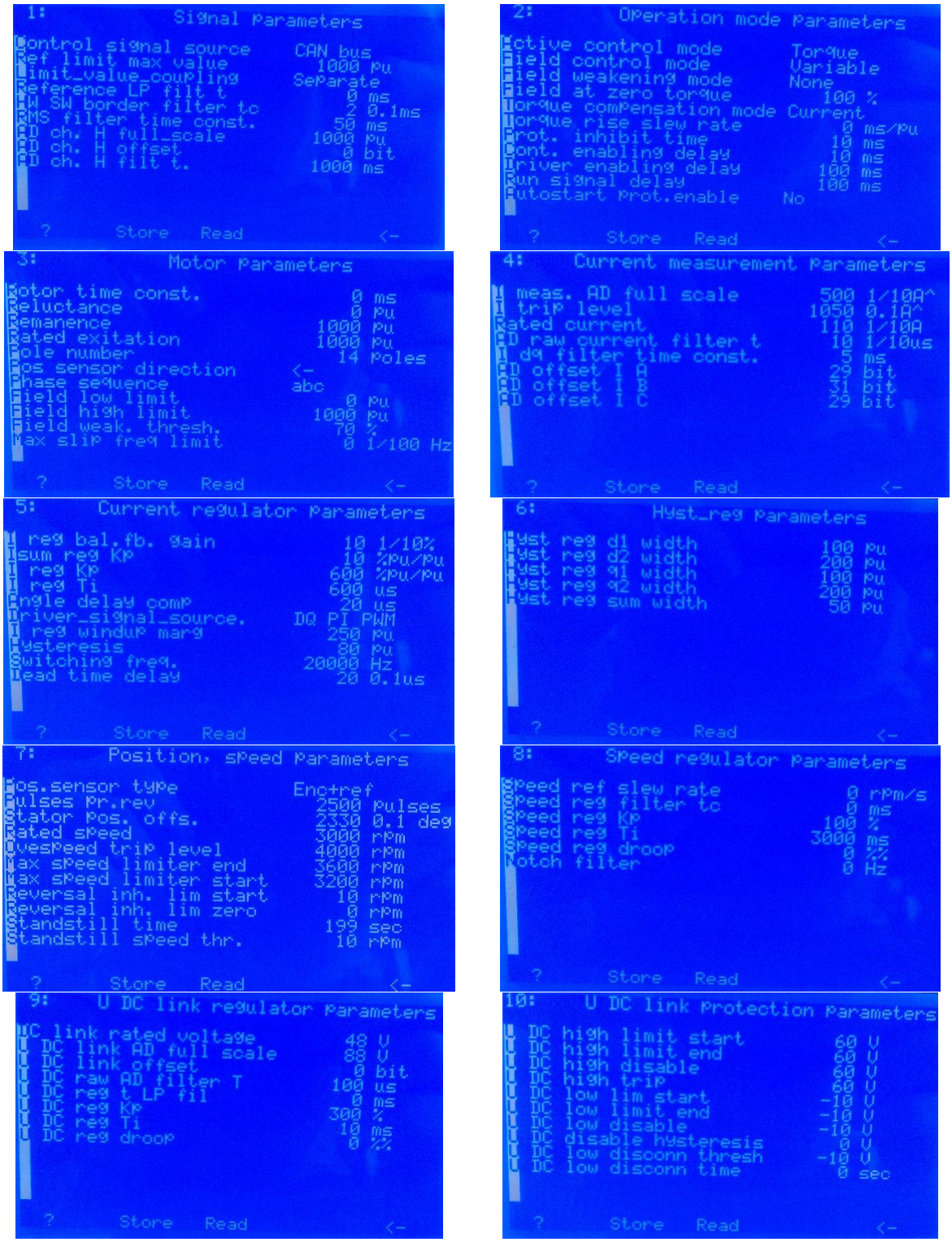

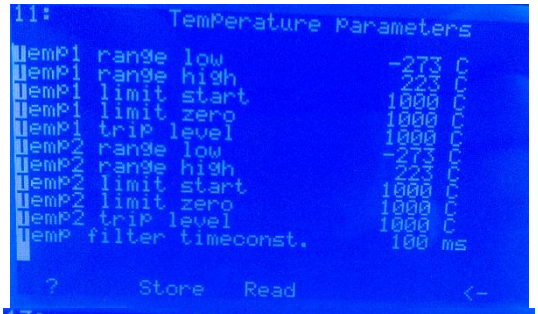
11: Temperature parameters
Temp1 range low -273 C
Temp1 range high 223 C
Temp1 limit start 1000 C
Temp1 limit zero 1000 C
Temp1 trip level 1000 C
Temp2 range low -273 C
Temp2 range high 223 C
Temp2 limit start 1000 C
Temp2 limit zero 1000 C
Temp2 trip level 1000 C
Temp filter timeconst. 100 ms
? Store Read <-

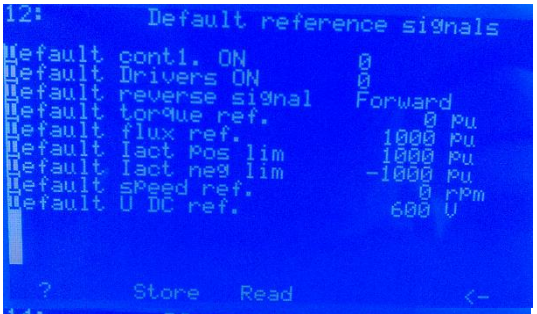
12: Default reference signals
Default cont1. ON 0
Default Drivers ON 0
Default reverse signal Forward
Default torque ref. 0 pu
Default flux ref. 1000 pu
Default Iact Pos lim 1000 pu
Default Iact neg lim -1000 pu
Default speed ref. 0 rpm
Default U DC ref. 600 V
? Store Read <-

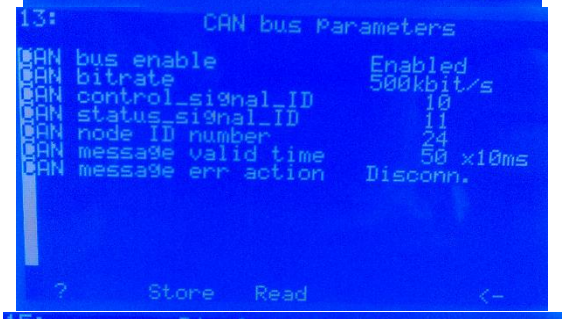
13: CAN bus Parameters
CAN bus enable Enabled
CAN bitrate 500kbit/s
CAN control_signal_ID 10
CAN status_signal_ID 11
CAN node ID number 24
CAN message valid time 50 x10ms
CAN message err action Disconn.
? Store Read <-

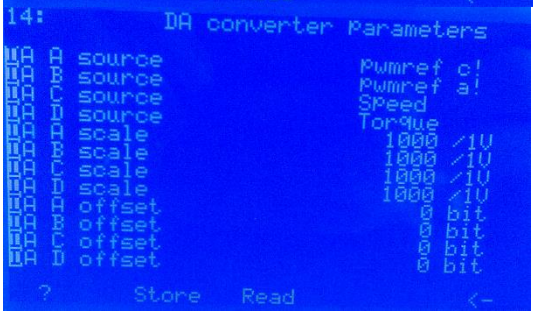
14: DA converter Parameters
DA A source PWMref c!
DA B source PWMref a!
DA C source Speed
DA D source Torque
DA A scale 1000 /1V
DA B scale 1000 /1V
DA C scale 1000 /1V
DA D scale 1000 /1V
DA A offset 0 bit
DA B offset 0 bit
DA C offset 0 bit
DA D offset 0 bit
? Store Read <-

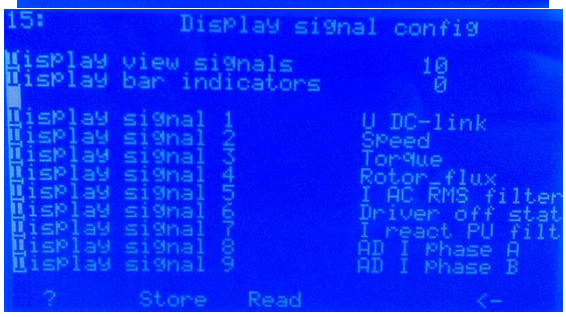
15: Display signal config
Display view signals 10
Display bar indicators 0
Display signal 1 U DC-link
Display signal 2 Speed
Display signal 3 Torque
Display signal 4 Rotor_flux
Display signal 5 I AC RMS filter
Display signal 6 Driver off stat
Display signal 7 I react PU filt
Display signal 8 AD I Phase A
Display signal 9 AD I Phase B
? Store Read <-

Appendix E: Inverter circuit board order process excel sheet

The excel sheet starts on the next page in order to provide a large image. This excel sheet is also available on the DNV GL Fuel Fighter team 2014 server.

2								Quantity
3	**Type #**	**Description**	**Status**	**Noca #**	**Noca description**	**Product #**	**Comment**	**1 CB**
4	0805/100K	1/8W 0805	In stock	27089121	Motstand 100K 1% 0.125W 0805 100ppm.			2
5	0805/100NF	Keramisk kondensator X7R 50V 0805	In stock	20039024	Kond. KER-X7R 100nF 50V 5% 0805			43
6	0805/100OHM	1/8W 0805	In stock	27089049	Motstand 100R 1% 0.125W 0805 100ppm.			3
7	0805/100PF	Keramisk kondensator NP0 50V 0805	In stock	20029081	KONDENSATOR KER-NP0 100pF 50V 5% 0805 PH			9
8	0805/10K	1/8W 0805	In stock	27089097	Motstand 10K 1% 0.125W 0805 100ppm			20
9	0805/10NF	Keramisk kondensator X7R 50V 0805	In stock	20039015	Kondensator KER-X7R 10nF 50V 5% 0805			3
10	0805/120OHM	1/8W 0805	In stock	27089051	Motstand 120R 1% 0.125W 0805 100ppm.			12
11	0805/12K	1/8W 0805	In stock	27089099	MOTSTAND 12K 1% 0.125W 0805 100PPM			1
12	0805/15K	1/8W 0805	In stock	27089101	Motstand 15K 1% 0.125W 0805 100ppm.			6
13	0805/1K	1/8W 0805	In stock	27089073	Motstand 1K0 1% 0.125W 0805 100PPM			9
14	0805/1NF	Keramisk kondensator NP0 50V 0805	In stock	20029019	Kondensator KER-C0G 1nF 50V 5% 0805			17
15	0805/2.2K	1/8W 0805	In stock	27089081	Motstand 2K2 1% 0.125W 0805 100ppm.			16
16	0805/200K	1/8W 0805	In stock	27089128	MOTSTAND 200K 1% 0.125W 0805 100PPM			3
17	0805/220K	1/8W 0805	In stock	27089129	Motstand 220K 1% 0.125W 0805 100ppm.			1
18	0805/22K	1/8W 0805	In stock	27089105	Motstand 22K 1% 0.125W 0805 100ppm.			1
19	0805/22NF	Keramisk kondensator X7R 50V 0805	In stock	20039068	Kond. KER-X7R 22nF 50V 10% 0805 *Mur			1
20	0805/4.7K	1/8W 0805	In stock	27089089	Motstand 4K7 1% 0.125W 0805 100ppm			1
21	0805/47K	1/8W 0805	In stock	27089113	Motstand 47K 1% 0.125W 0805 100ppm			12
22	0805/47PF	Keramisk kondensator NP0 50V 0805	In stock	20029087	KONDENSATOR KER-NP0 47pF 50V 5% 0805 PH			7
23	100UF/50V/FK	Elektrolyt EEEFK1H101GP 350 mA 0.34 Ohm (100kHz) 1	In stock	20019098	Kond. OFM-Lytt LoESR 100µF 50V 105° *FK			2
24	1206/100OHM	1/4W 1206	In stock	27129049	Motstand 100R 1% 0.25W 1206 100ppm			19
25	1206/10K	1/4W 1206	In stock	27129097	Motstand 10K 1% 0.25W 1206 100ppm			5
26	1206/1OHM	1/4W 1206	In stock	27129001	MOTSTAND 1R0 1% 0.25W 1206 500PPM			6
27	1206/1uF/50V	Keramisk kondensator X7R 50V 1206	In stock	20039251	Kond. KER-X7R 1µF 50V 10% 1206			5
28	1206/2.2K	1/4W 1206	In stock	27129081	Motstand 2K2 1% 0.25W 1206 100ppm			3
29	1206/20OHM	1/4W 1206	In stock	27129032	MOTSTAND 20R 1% 0.25W 1206 100PPM			12
30	1206/220OHM	1/4W 1206	In stock	27129057	Motstand 220R 1% 0.25W 1206 100ppm.			6
31	1206/22K	1/4W 1206	In stock	27129105	Motstand 22K 1% 0.25W 1206 100ppm.			5
32	1206/2K	1/4W 1206	In stock	27129080	MOTSTAND 2K0 1% 0.25W 1206 100PPM			1
33	1206/LED GRØNN	Grønn lysdiode SO 1206	In stock	13013135	LED KPTD-3216MGC Grønn 1206 Klar *Kingbr			1

34	1206/LED GUL	Gul lysdiode SO 1206	Ordered 24/3			466-4018P, LED KPTD-3216SYC	RS comp	http://no.rs-online.com/web/	1
35	1206/LED RØD	Rød lysdiode SO 1206	In stock	13013137		LED KPTD-3216URCK Rød 1206 Klar *Kingbr			1
36	2.2UF/450V/CKG57	TDK CKG57NX7T2W225M500JH Stacked Ceramic capaci	Ordered 17/3			221-0746	2210746	TDK - CKG57NX7T2W225M500JI	9
37	22UF/25V/CKG57	TDK CKG57KX7R1E226M335JH Ceramic capacitor X7R 2	Ordered 18/3			1826354	1826354	KEMET - C2220C226M5R2CT500	12
38	4043	CMOS Quad RS latch tristate SO 16	Ordered 24/3			355-8827	RS comp	http://no.rs-online.com/web/	2
39	4049	CMOS Hex inverter SO 16	Ordered 17/3			146-8727	1468727	ON SEMICONDUCTOR - MC140	2
40	4071	CMOS Quad 2 input OR SO 14	Ordered 24/3			662-6857	RS comp	http://no.rs-online.com/web/	3
41	4093	CMOS Quad 2 schmitt trigger input NAND SO 14	In stock	15049011		IC 4093B Quad 2-Input NAND-Gate SO14	1201296	NXP - HEF4093BT - IC, NAND, Q	1
42	4532	CMOS 8 input priority encoder SO 16	Ordered 17/3			966-5226	9665226	ON SEMICONDUCTOR - MC145	2
43	4584	CMOS Hex schmitt trigger inverter SO 14	In stock	15049038		IC 40106B Hex Schmitt-Trigger(INV) SO14			1
44	78L05	5V 100 mA Serieregulator SO8	Ordered 17/3			966-6265	9666265	ON SEMICONDUCTOR - MC78L0	2
45	820uF/63V/FR	Elektrolyt EEUFR1J821 3A 24mOhm(100kHz) 105C Pana	Ordered 12/3			969-2576	9692576	PANASONIC - EEUFC1J102 - CA	6
46	ACPL-333J	Optocoupler gatedriver 2.5A with fault detection. Avago SO	Ordered 17/3			170-7748	1707748	AVAGO TECHNOLOGIES - ACPL-	6
47	ACPL-C790	Optocoupler insulation amplifier. Avago Stretch SO8	Ordered 17/3			185-4250	1854250	AVAGO TECHNOLOGIES - ACPL-	1
48	BZX84-C3V3	Zenerdiode. 3.3V 0.25W Vishay SOT23	In stock	10039000		ZENERDIODE BZX84C3V3 0.3W 5% SOT23			6
49	BZX84-C9V1	Zenerdiode 9.1V 0.25W Vishay SOT23	In stock	10039009		ZENERDIODE BZX84C9V1 0.3W 5% SOT23 Z8 PH			6
50	BZX84-C5V1	Zenerdiode 5.1V 0.25W Vishay SOT23	In stock	10039003		Zenerdiode BZX84C5V1 0.3W 5% SOT23 *Z2 NXP			1
51	DUBOX1x2/ STRAI	FCI/Berg Dubox 76384-302 1x2P. Stående	Servicelab			in bag marked with "Servicelab" and "Testpins++"	ELFA	https://www.elfaelektronikk.n	1
52	DUBOX1x3/ STRAI	FCI/Berg Dubox 76384-303 1x3P. Stående	Servicelab			in bag marked with "Servicelab" and "Testpins++"	ELFA	https://www.elfaelektronikk.n	2
53	DUBOX1x4/ STRAI	FCI/Berg Dubox 76384-304 1x4P. Stående	Servicelab			in bag marked with "Servicelab" and "Testpins++"	ELFA	https://www.elfaelektronikk.n	4
54	ES1D	Diode 200V 1A Ultrahurtig trr 25ns. Vishay SMA/DO214AC	In stock	10019016		Diode ES1DL 200V 1A Avalanche SOD123F			6
55	FLATKABEL16MS	Flatkabelkontakt 16P. Med vegger. Uten utkastere/låsing. St	Servicelab			43-653-95	ELFA	https://www.elfaelektronikk.n	1
56	FZT651	NPN transistor 60V 3A 2W hfe Zetex/Diodes inc SO223	Ordered 17/3			9525009	9525009	DIODES INC. - FZT651 - TRANSIS	1
57	FZT751	PNP transistor 60V 3A 2W hfe Zetex/Diodes inc SO223	Ordered 24/3			274-936	RS comp	http://no.rs-online.com/web/	1
58	IPP100N08S2-07	MOS N-kanal transistor. 75V 6.8 mOhm 100A Infineon T	Ordered 12/3			DO NOT MOUNT!		Subject to adaptation. Will be	6
59	1206/0Ohm	1/4W 1206	In stock	27129000		Motstand 0R0 5% 0.25W 1206 200ppm			2
60	LEM LAH 25-NP	8/12/25 A Current sensor 25 mA out. +-15V LEM	Ordered 12&17/3			214-6849	2146849	LEM - LAH 25-NP - CURRENT TR	3
61	LM2903M	2x komparator LM393 ekv. -40 - 85C Texas Instruments.	In stock	17029035		IC LM2903M Dual Comparator SO8			1
62	MBR0540	Schottkydiode 40V. 0.5A ON Semiconductor SOD123	In stock	10029024		Schottkydiode MBR0540T1G 40V 0.5A SOD123			7
63	MKDS 5/2-7,62	Screw terminal 4 mm2. 7.62 mm pin spacing. Phoenix Cont	Servicelab			48-449-81	ELFA	https://www.elfaelektronikk.n	1
64	MKDS 5/3-7,62	Screw terminal 4 mm2. 7.62 mm pin spacing. Phoenix Cont	Servicelab			48-449-99	ELFA	https://www.elfaelektronikk.n	1
65	MSTBVA2.5/2-G-5.	Phoenix Combicon MSTBVA 2.5/2-G-5.08 Hann 2 pol. St	In stock	56059298		REKKEKLEMME MSTBVA 2,5/2-G-5.08AU Basis			1

66	US1M	Diode fast 1000V 1A	Ordered 17/3		185-8603	1858603	DIODES INC. - US1M-13-F - DIO	6
67	OPA140AID	Operational amplifier 10 MHz 4.5-36V Texas instru	Ordered 17/3		185-5117	1855117	TEXAS INSTRUMENTS - OPA140	1
68	PTC/B59901 D90 A	PTC-Motstand 90C. 1 kOhm 30V Epcos Festeøre.	Ordered 12/3		DO NOT MOUNT! 218832	218832	EPCOS - B59901D90A40 - THERM	1
69	R24P15S/P/R6.4	DC/DC-converter 24 VDC in. 15 VDC 1 W reinforced insul	Ordered 13/3 3PCB		666-4045, TMV 2415S	RS comp	http://no.rs-online.com/web/	6
70	SFH610A-4X006	Optokobler VDE0884 Viorm 890V. CTR: 160-320%. Visha	Ordered 17/3		225-1536	2251536	VISHAY - VO610A-4X017T - OPT	1
71	STRAP	2 pin header	Servicelab		in bag marked with "Servicelab" and "Testpins++"			2
72	TEST	Testpin. 1 pin header	Servicelab		in bag marked with "Servicelab" and "Testpins++"			16
73	THM 10-4815WI	DC/DC-converter 18-75 VDC in. 24V DC 10 W. Traco. DIL	Ordered 12/3		69-547-10, TEN 6-4815WIN	ELFA	https://www.elfaelektronikk.r	1
74	TLV3202AID	2x Rail to Rail 40-ns Push-Pull Output Comparators Texas	Ordered 18/3		595-TLV3202AID	595-TLV32	Mouser electronics	3
75	TMR 1-2411	DC/DC-converter 18-36 VDC in. 5 V DC 1 W. Traco. SIP6	Ordered 17/3		781-3213, TMR 1-2411	7813213	RS Components	1
76	TPS3707-50D	Voltage supervisor. 4.55V and Vadj. Texas Instruments. SO	Ordered 17/3		232-3740	2323740	TEXAS INSTRUMENTS - TPS3707	1

Fix 5/7 2014:

R143, R148: 150k.

R149: 3k.

R136,137,138,141,145: 200k

Appendix F: E-mail regarding purpose-built motor controller requirement

Gmail by Google

Eirik Mo <eirikheienmo@gmail.com>

TR: Purpose-built motor controller question

Shell-Eco.Marathon@shell.com <Shell-Eco.Marathon@shell.com> Mon, Apr 14, 2014 at 12:29 PM
To: eirikheienmo@gmail.com

Dear Erik,

I apologize for the delay in answering your question.

Your hardware design meets the requirement as purpose built, your team should be able to describe the FPGA software function and operation.

Kind regards,

Sarah

De : Eirik Mo [mailto:eirikheienmo@gmail.com]
Envoyé : 13 March 2014 13:28
À : Marathon, Shell-Eco S SPSHELL-EA/ES
Objet : Purpose-built motor controller question

Hi.

This is the part of the rules I'm referring to:

"The motor controller MUST be purpose-built for the Shell Eco-marathon. Modifications to purchased motor controllers are not acceptable. Motor controllers built from sub-components such as single-board computers, power stages, etc. are encouraged. If a unit is developed incorporating the motor controller into one or more single printed circuit boards (PCB) the text "SEM" needs to be included in the mask of the PCB etching." - Shell Eco Marathon Official rules 2014

I have attached an image that illustrates the way I'm designing the motor control for DNV GL Fuel Fighter. The inverter PCB is in production now and will have the letters SEM printed on it. The inverter is controlled by 6 pulses given to each inverter mosfet. We use will a FPGA card to produce these pulses from 4 measurements + torque reference given by a CAN bus. The software on the FPGA card is made by our sponsor SINTEF energi for general inverter PWM control purposes.

My question is: Is our motor controller solution classified as a purpose-built motor contoller? I think so because the motor control system is unique for the competition. The inverter, in particular, is made just for the competition.

Regards

Eirik Heien Mo

Power Electronics

DNV GL Fuel Fighter

NTNU, Trondheim, Norway

Appendix G.1: Official Shell Eco-Marathon results list for UrbanConcept class [9]

If the results are hard to read please see the online version.

Shell Eco-marathon

Shell Eco-marathon Europe 2014

Final results : UrbanConcept Battery Electric

21/05/2014

Rank	Team n°	Team name	Country	Organization	Institution type	Competition category	Energy type	Best attempt (km/kWh)	Attempt 1 (km/kWh)	Attempt 2 (km/kWh)	Attempt 3 (km/kWh)	Attempt 4 (km/kWh)	Attempt 5 (km/kWh)
1	701	Electricar Solution	France	Lycee Des Metiers De L Energie Arles	School	Urban concept	Battery Electric	312.1	299.7	305	281.8	312.1	
2	702	Team proTRon	Germany	Hochschule Trier	University	Urban concept	Battery Electric	219	202.7	209.6	218.8	219	
3	703	DNV GL Fuel Fighter 2	Norway	Norwegian University Of Science And Technology	University	Urban concept	Battery Electric	198.7	198.7				
4	707	SZEnergy Team	Hungary	Szechenyi Istvan University	University	Urban concept	Battery Electric	190.7	173	173.9	180.4	190.7	
5	705	ElBa	Sweden	Kth Royal Institute Of Technology	University	Urban concept	Battery Electric	181.5			181.5	164.4	
6	724	Team EVA	Netherlands	Hogeschool Van Amsterdam	University	Urban concept	Battery Electric	177.9	168.1	173.6	142.1	166.1	177.9
7	717	Evi Neuruppin	Germany	Evangelische Schule Neuruppin	School	Urban concept	Battery Electric	166.1	166.1	163.7	161.8	153.1	
8	708	Sakarya University Advanced Technologies A	Turkey	Sakarya Universitesi	University	Urban concept	Battery Electric	145	131.7	130.7	145		
9	734	YUEMT	Turkey	Yeditepe University	University	Urban concept	Battery Electric	119	107.1		116.7	119	
10	709	NIEPCE	France	Lycee Nicephore Niepce	School	Urban concept	Battery Electric	111.3	111.3	110.8			
11	729	Os Alcaides	Portugal	Agrupamento De Escolas Alcaides De Faria Barcelos	School	Urban concept	Battery Electric	108	100.5	108			
12	727	Smart Power Urban	Poland	Silesian University Of Technology	University	Urban concept	Battery Electric	59.7		59.7	49.9	57.5	
13	714	ENSIL Team	France	ENSI Limoges	University	Urban concept	Battery Electric	48.4		48.4			
14	715	IUT Alençon	France	IUT Alençon	University	Urban concept	Battery Electric	44.7		44.7			
15	736	Angel's angels	Bulgaria	Technical University Varna	University	Urban concept	Battery Electric	34.8		34.8			

Appendix G.2: Official Shell Eco-Marathon results list for Prototype class [9]

If the results are hard to read please see the online version.

Shell Eco-marathon Europe 2014
Final results : Prototype Battery Electric

21/05/2014

Rank	Team n°	Team name	Country	Organization	Institution type	Competition category	Energy type	Best attempt (km/kWh)	Attempt 1 (km/kWh)	Attempt 2 (km/kWh)	Attempt 3 (km/kWh)	Attempt 4 (km/kWh)	Attempt 5 (km/kWh)
1	304	TERA TU Graz	Austria	T.U. Graz	University	Prototype	Battery Electric	1091.6	836		1081.4	1091.6	
2	301	PASQUET ECO MOTION SCS	France	Lycee Louis Pasquet	School	Prototype	Battery Electric	894.5	746.2		894.5	815.8	825.8
3	327	Lausitz Dynamics	Germany	BTU Cottbus- Senftenberg (Campus Senftenberg)	University	Prototype	Battery Electric	839.5	691.2	732.2		839.5	
4	328	Ruppin Jet	Germany	Oberstufenzentrum Ostprignitz Ruppin	School	Prototype	Battery Electric	830	575	830			
5	305	Team AU	Denmark	Aarhus Universitet	University	Prototype	Battery Electric	814.6		711.1	814.6		
6	303	IDEA CEU Team	Spain	Universidad Ceu Cardenal Herrera	University	Prototype	Battery Electric	794.5	769.1	794.5	749.6	793.8	
7	342	DNV GL Fuel Fighter	Norway	Norwegian University Of Science And Technology	University	Prototype	Battery Electric	612.8	512.4	516.5	612.8		
8	309	Team Zero C	Italy	Itis Leonardo Da Vinci	School	Prototype	Battery Electric	604.6	400.6	386.1	386	604.6	
9	329	Schluckspecht	Germany	University Of Applied Sciences Offenburg	University	Prototype	Battery Electric	589.9	502	589.9	551.3		
10	306	Eco Motion Team by ESSTIN	France	ESSTIN De Nancy	University	Prototype	Battery Electric	533.6		479.4	533.6		
11	331	Poseidon	Greece	Technological Educational Institute Piraeus	University	Prototype	Battery Electric	527.9	527.9		236.4		
12	344	Smart Power	Poland	Silesian University Of Technology	University	Prototype	Battery Electric	487.3	365.4	481.3	487.3		
13	326	PSTVA	France	PST Université Paris Ouest	University	Prototype	Battery Electric	480.3	459.9	480.3	464	471	
14	346	Solar-GT	Spain	C.I.P.F.P. Benicarló	School	Prototype	Battery Electric	454.9		449.5	454.9		
15	324	Vector Ecoteam	France	MINES ParisTech et Lycees Louis Armand	University	Prototype	Battery Electric	439.5	370.4	426.2	438.7	439.5	
16	332	Kandó Electric	Hungary	Kalman Kando Secondary Technical And Vocational School	School	Prototype	Battery Electric	433.3		373.5		433.3	
17	302	TUfast Eco Team	Germany	Technische Universitaet Muenchen	University	Prototype	Battery Electric	418.9			418.9		
18	330	Prometheus	Greece	National Technical University Of Athens	University	Prototype	Battery Electric	368.5		368.5			
19	347	ECO-DIMONI	Spain	I.E.S Cotes Baixes	School	Prototype	Battery Electric	300.2	300.2				
20	314	Thomas More Eco Drive Team	Belgium	Thomas More De Nayer	School	Prototype	Battery Electric	250.8	171.6	250.8	232.1		
21	350	UCAM RACING TEAM	Spain	Universidad Catolica San Antonio	University	Prototype	Battery Electric	234.8	210.6	234.8			
22	358	Pteron	United Kingdom	A.J. Woods Education And Training Hub	School	Prototype	Battery Electric	234.3		225.2	195	234.3	
23	316	Avtomobilist	Bulgaria	University of Ruse	University	Prototype	Battery Electric	168.3	140.7	149.7	163.9	168.3	
24	357	AE2 PROJECT TEAM	Turkey	Yildiz Technical University	University	Prototype	Battery Electric	161.8	153.2	161.8		156.9	
25	325	VINCI ECO'DRIVE	France	Pôle Universitaire Léonard de Vinci	University	Prototype	Battery Electric	142.6		142.6		117.2	
26	340	De Leekbumers	Netherlands	The Lindenborg	School	Prototype	Battery Electric	117.1		117.1	111.7		
27	315	blue-ev	Bulgaria	N.Vaptsarov	School	Prototype	Battery Electric	92.7		92.7			
28	343	WAT ECO TEAM	Poland	Military University of Technology Warsaw	University	Prototype	Battery Electric	80.6	71.9	80.6			